THESIS

DIAGENESIS AND GEOCHEMISTRY OF THE LOWER PERMIAN INGLESIDE FORMATION, OWL CANYON AREA, LARIMER COUNTY, COLORADO

Submitted by

Ahmad Issa

Department of Geosciences

In partial fulfillment of the requirements
For the Degree of Master of Science
Colorado State University
Fort Collins, Colorado
Summer 2018

Master's Committee:

Advisor: Sally Sutton

John Ridley
Susan De Long

ABSTRACT

DIAGENESIS AND GEOCHEMISTRY OF THE LOWER PERMIAN INGLESIDE FORMATION, OWL CANYON AREA, LARIMER COUNTY, COLORADO

The purpose of this study is to determine the diagenetic history and timing of hydrocarbon migration in the Lower Permian Ingleside Formation as revealed in the Ingleside roadcut at Owl Canyon area, Colorado. The studied exposure is divided into fourteen beds composed of quartz arenite sandstone, limestone, dolomite, or siltstone. Observations from outcrop and thin sections, including calcite veins, carbonate-hosted vugs, and carbonate cement, suggest carbonate mobility throughout the outcrop. Stylolites parallel to bedding may have formed by pressure solution related to compaction, and pressure solution of carbonates is one possible source of carbonate that could have precipitated in veins or as cement. The formation was affected by other diagenetic processes, in addition to compaction and carbonate cementation, including feldspar dissolution and alteration and several stages of cementation. Cements include hematite, calcite, dolomite, kaolinite, and quartz overgrowth cement. Hematite cement was determined to have precipitated very early. Poikilotopic carbonate cement was precipitated very early, but after the precipitation of the hematite cement. Blocky calcite and blocky dolomite cements, the most common cements within the formation, were precipitated after the hematite and poikilotopic cements. Kaolinite cement was probably precipitated in association with feldspar dissolution and alteration, or occurred with feldspar dissolution during modern weathering. Hydrocarbon migration probably occurred before the precipitation of the blocky carbonate cement. The relationship between S and MgO in some sandstone samples may indicate that Mg and S have been added by diagenetic fluids. Also, K_2O correlates with Al_2O_3 probably because both elements are mainly in the same phases, clay minerals, micas, K-feldspar, or glauconite. This study of the Ingleside outcrop provides some information about the diagenesis, possible timing of possible hydrocarbon migration through the Ingleside Formation, and geochemical and mineralogical composition of the exposure, which was used to interpret the diagenetic history throughout the outcrop. Therefore, this study adds to understanding of hydrocarbon migration and the hydrocarbon pathways in this part of the Denver Basin.

ACKNOWLEDGMENTS

First and foremost, I want to express my deepest gratitude to my advisor Prof. Sally Sutton for the continuous support of my master's study and related research, and for her patience, motivation, and immense knowledge. The door to Prof. Sally office was always open whenever I ran into a trouble spot or had a question about my research or writing. She is also more than an advisor as she provided me numerous support and guidance outside research. Besides my advisor, I would like to thank the rest of my thesis committee: Prof. John Ridley and Prof. Susan De Long for their insightful comments and encouragement. Thanks go to the Libyan ministry of higher education and scientific research, and Omar Al-Mukhtar University for their scholarship and funding my master's study. Finally, I want to thank my family and friends for their unconditional support and being with me at every difficult moment.

TABLE OF CONTENTS

LIST OF TABLES

LIST OF FIGURES

CHAPTER 1
INTRODUCTION

Diagenesis can be defined as all events that cause alterations in sediments or sedimentary rocks after deposition (Berner, 1980). Evaluating diagenetic processes and their effects on reservoir quality is a valuable exploration tool for the petroleum industry. The Ingleside Formation has been studied by many in the past to describe the sedimentology and stratigraphy of the formation. Less work, however, has been done on the diagenesis, timing of hydrocarbon migration, or the geochemistry of the Ingleside Formation. The main purpose of this study of one exposure of the Ingleside Formation is to investigate the diagenetic processes that affected the formation. An important aim of understanding diagenesis is to determine the timing of diagenetic events and of hydrocarbon migration. This is especially important for the petroleum industry because diagenesis can impact porosity and permeability, as well as hydrocarbon migration pathways, hence having implications for hydrocarbon exploration and reservoir quality. Porosity is important for reservoir quality because hydrocarbons are stored in the porosity. Adequate permeability is also important because it allows hydrocarbons to move through the pore spaces and may permit production of hydrocarbons from the reservoir. Therefore, hydrocarbons are more likely to migrate through rocks that have high porosity and permeability. Further, diagenetic processes can impact the porosity distribution and then control the hydrocarbon pathways in sandstone reservoirs (Worden and Burley, 2003). Oil companies use some methods that require injection of chemical materials that increase a reservoir’s permeability in order to increase the production. This requires determining the mineralogy and chemical reactions that occur naturally in sandstone reservoirs (Pittman and King, 1986). In addition, it is essential to understand hydrocarbon migration to predict the hydrocarbon migration direction and the presence of hydrocarbon traps (Bjørlykke, 2010). Diagenetic events can impact the porosity and permeability. This is important because porosity and permeability may increase or decline because of different types of diagenetic events. Therefore, this will impact the hydrocarbon production, emplacement and trapping. Studying the diagenetic processes and their timing can help with understanding of burial history. Oil companies use this information in basin modelling and to determine the timing of petroleum generation, migration and accumulation (Worden and Burley, 2003).

Understanding the timing of hydrocarbon migration can help to predict where the oil moves and accumulates. Oil companies study hydrocarbon migration to determine where the migration and accumulation of hydrocarbon occurred. Further, investigating the critical moment (hydrocarbon generation, migration and accumulation) is important in characterizing the petroleum system and basin modelling (Al-Hajeri et al. 2009). Therefore, oil companies are interested in the relative timing of various diagenetic events and of hydrocarbon migration.

1.1 Objectives

The goals of this study are to use outcrop characterization, thin section petrography, and whole rock geochemistry to characterize the diagenetic history of this Ingleside exposure and to place the timing of hydrocarbon migration within that diagenetic history.

1.2 Previous Work

1.2.1 Ingleside Formation

The Lower Permian Ingleside Formation exposed along the Front Range in northern Colorado (Fig. 1.1) was deposited to the east of the Ancestral Rocky Mountains and crops out today on the western edge in the Denver-Julesburg Basin. Butters (1913) named the Ingleside Formation because of its exposure at the Ingleside Quarry, near the study area at Owl Canyon.

Generally, the Ingleside Formation is composed of quartz sandstone that was deposited mainly in a nearshore marine setting as offshore bars (Maughan and Ahlbrandt, 1978), with interbedded marine limestone. Davis (1947) studied the sedimentary environment of the Ingleside Formation in North Central Colorado. He suggested that the limestone beds in the upper part of the Ingleside Formation formed during low amplitude sea level fluctuations. He hypothesized that a semi-arid environment is documented by some features, including gypsum, torrential cross-bedding, interstratification with the semi-arid Fountain Formation arkose, and the preservation of readily weathered heavy minerals. He also inferred the age of the Ingleside Formation to be Pennsylvanian based on lithological evidence, and that the Casper Formation in southeastern Wyoming, the upper Hartville Formation in eastern Wyoming, and Tensleep sandstone in northern Wyoming are the regional equivalents of the Ingleside Formation. Hoyt and Chronic (1961) used the existence of a fossil fusulinid found in the Ingleside Formation at Owl Canyon to determine the age of the formation. They defined the fusulinid as *Triticites ventricosus* and defined the Ingleside Formation to be Wolfcampian in age (Hoyt and Chronic, 1961; Hoyt, 1962).

Maughan and Wilson (1963) observed that at the Colorado-Wyoming border the maximum thickness of the Ingleside Formation is approximately 79.3 m. In the study area at Owl Canyon the outcrop thickness is about 42.2 m, therefore, approximately the lower 53% of the Ingleside is exposed in the study area, if the thickness matches that at the border. They proposed that the formation was deposited in a marine setting, beaches, and dunes marginal to the sea, whereas on its southern edge the formation was deposited in fluvial and marginal marine settings. They also suggested that in the eastern part of the Laramie Range the Ingleside

Formation is correlated with the upper portion of the Casper Formation, and in the Lyons area with the uppermost portion of the Fountain Formation.

Steidtmann (1974) interpreted the depositional environment of the cross-stratification in the Casper Formation in Laramie Basin, Wyoming. He concluded that sandstone of the Casper Formation is eolian in origin, based on ripples, truncated ripples, and lag deposits. The Permian formations in the Bellvue-Livermore area, including the Ingleside Formation, were studied in detail by Berman (1978). He interpreted the depositional mechanism of the Ingleside sandstone in this area to be mainly eolian.

Fredrickson (1978) studied the depositional environments and the petrography of the Ingleside outcrops in the Owl Canyon area and described them in detail. She concluded that the Ingleside Formation has a gradational contact with the Fountain Formation at Owl Canyon. She suggested that sedimentary structures and textures in Ingleside sandstones indicate marine nearshore settings, and the deposition was in beach, backbeach, foreshore shoreface, and coastal dune zones, whereas limestone was deposited mainly in shallow water. Sipe (1984) described the depositional environment and the prominent bedding planes of the Ingleside Formation around Livermore, Colorado. He concluded that the Ingleside sandstones were deposited in dune, coastal marine, and ephemeral stream settings, whereas the marine limestones were deposited in shallow water, nearshore zones, and bounded bays, and the non-marine limestone lenses were deposited in lakes. He suggested that the late Paleozoic glaciations were possibly responsible for the cyclic sea level changes that controlled Ingleside deposition. The sea level fluctuations were also responsible for the deflation and erosion, which formed the bounding surfaces in the Ingleside Formation.

Napp (1985) described the sedimentology and the stratigraphy of the Fountain and Ingleside Formations across a wide area in the northwest part of the Denver Basin, and described the contact between the Ingleside Formation and the Fountain Formation as a conformable contact. He also noted a transition from an alluvial depositional environment to wave-dominated fan deltas and a carbonate shelf environment. Schatz (1986) described the depositional environments of the Fountain-Ingleside sequence from south of Lyons to Loveland, Colorado. He concluded that the Ingleside Formation was deposited in a coastal dune field, interfingers with the upper Fountain formation, and transitions from braided fluvial deposits to coastal dune deposits. He suggested that sea level fluctuations were probably responsible for the local carbonate beds in the formations or they may have been formed from small fresh water ponds. Also, dunes, interdunes, ponds, and channel deposits were observed in the Ingleside Formation. The variety of the primary sedimentary structures within the Ingleside allows assessment of the paleoenvironment (Crick, 1987). Crick (1987) presented a detailed sedimentological study of the Ingleside Formation in an area along the western side of Horsetooth Reservoir, Larimer County, Colorado, to determine the environments of deposition. He concluded that the Ingleside in that area consists mainly of sandstone, with interbedded siltstone and mudstone. A marine transgression onto the Fountain fan deltas formed a disconformable contact with the lower Fountain Formation. He divided the Ingleside Formation into twelve distinctive lithofacies based on data obtained from seventeen measured sections. He also interpreted the depositional sequences in the lower portion of the formation as mainly transgressive, and in the middle and upper portions of the Ingleside as progradational or regressive.

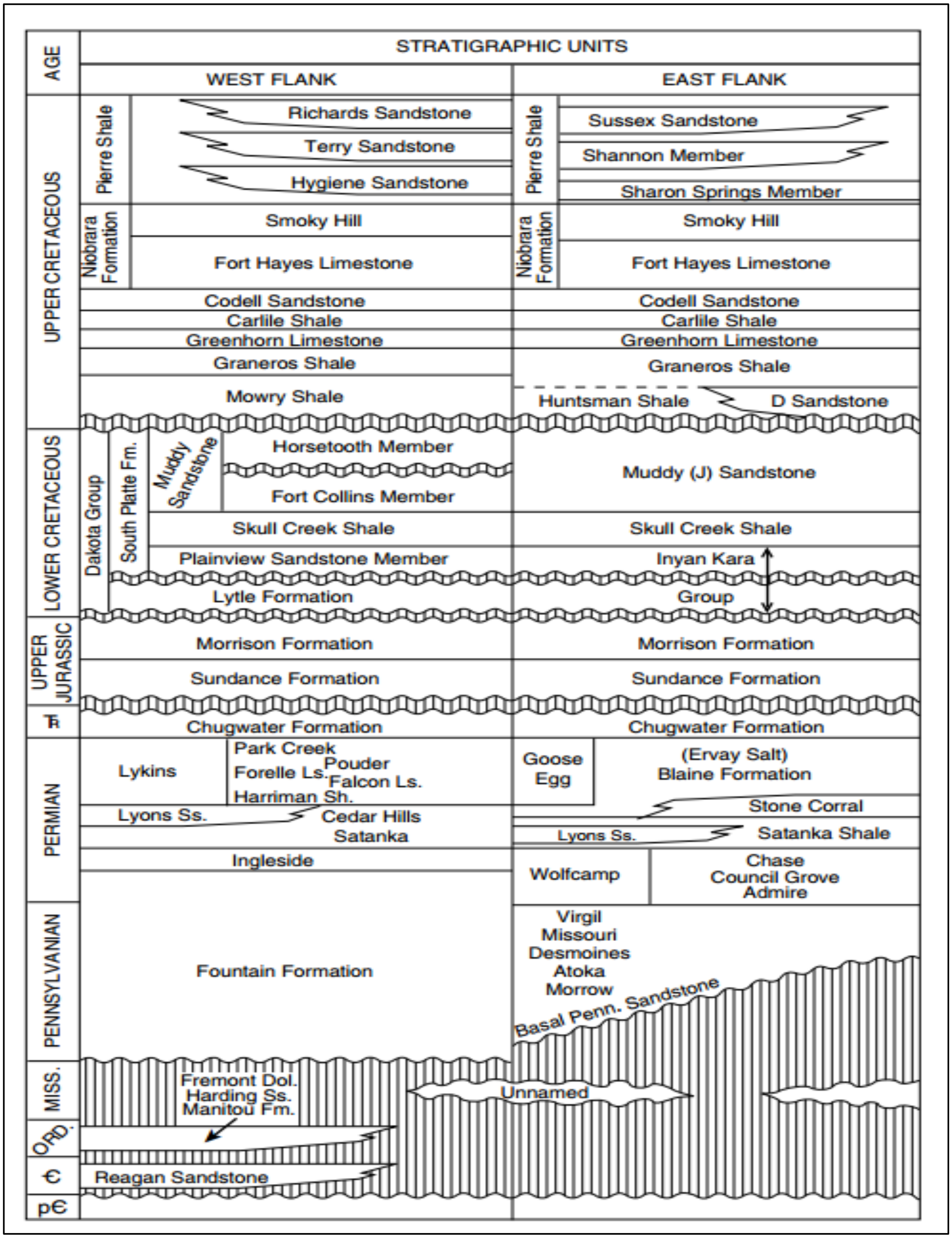

Figure 1-1. The stratigraphic columns of the west and east flanks of the Denver-Julesburg Basin, including the Lower Permian Ingleside Formation (Higley and Cox, 2007).

Maughan and Wilson (1963) described the Ingleside sandstone at Owl Canyon as light brown, moderate reddish-orange, and orange-pink in color, whereas the carbonate rocks, which are approximately 28% of the formation, are yellowish-grey, light-grey, and grayish-pink. They reported that the Ingleside sandstone grains are very fine to fine, and vary from sub-angular to rounded. Fredrickson (1978) observed that the Ingleside sandstone includes quartz, feldspar, rock fragments, carbonate grains, micas, clay minerals, and heavy minerals. Quartz is the predominant mineral and ranges from 74% to 91% in sandstone samples and generally increases up-section. Mainly the quartz grains are monocrystalline with minor polycrystalline grains. Some quartz grains host inclusions of heavy minerals and bubble trains. She reported that the feldspar abundance declines in the upper part of the formation. Feldspar includes K-feldspar which is the common type, and ranges between 6% and 18% with plagioclase ranging between 0% and 5%. Quartzite, igneous rock fragments, and carbonate rock fragments are present in the Ingleside Formation, with quartzite fragments most abundant. Carbonate grains are composed of skeletal fragments, peloids, and minor oolites. The samples contain minor amounts of biotite and muscovite. Clay minerals are present and include illite, smectite, and kaolinite. Illite and smectite are more common than kaolinite. Only one sample contains a small amount of mixed layer smectite-illite. The samples include a minor quantity of heavy minerals. She described the Ingleside sandstone texture as ranging from sub-mature to mature and moderately to moderately-well sorted, with fine to very fine grains showing roundness ranging from sub-angular to sub-rounded. All sandstone samples are classified as subarkose.

Fredrickson (1978) also observed that cements in the sandstone are calcite, dolomite, hematite, and quartz overgrowths. Carbonate cement is the most common and ranges from 4.9% to 28.8%. Calcite cement is the main carbonate and dolomite cement is present in only one sample. She hypothesized that calcite cement probably precipitated early, which saved grains from compaction and prevented feldspar alteration. Hematite is present in small amounts as detrital grains, rim cement, and in pore spaces. Quartz overgrowth cement occurs on quartz grains as euhedral faces. She also described that the main diagenetic processes that affected sandstone are carbonate cementation and replacement of detrital grains (feldspar). Grains were not affected by major compaction. Stylolites occurred in limestone beds as a result of pressure solution and may have been the source for calcium carbonate. Stylolites occurred parallel to bedding and formed by compaction. Sipe (1984) described the Ingleside sandstone as mainly subarkose, ranging from fine to very coarse sand and poorly to well sorted.

Several observations in previous studies of the Ingleside and Casper Formations are particularly relevant to consideration of the hydrocarbon reservoir properties of these units. Prucha et al. (1965) described low angle reverse faulting and conjugate shear fractures within the Ingleside Formation in the Horsetooth Reservoir area, Larimer County, Colorado. Kelly (1984) described the petroleum geology of the Upper Casper Formation in the Northern Laramie Basin. She concluded that the depositional system of the Upper Casper Formation is characterized by two subenviroments, dunes and interdune. The dune sediments are well-sorted and contain low carbonate cement, therefore they may have excellent reservoir quality. The interdune sediments contain lenses of poorly-sorted, well-cemented sandstone, and lenses of very low permeability nonmarine siltstone and limestone. This study of the Caspar Formation suggests that the oil distribution in the formation may partly depend on the depositional environment. Oil may migrate to dune sandstones because they have high porosity and permeability, whereas the interdune sandstones may prevent oil migration because they have low porosity and permeability. This is represented in outcrop where the dune sandstone commonly contains oil stains, whereas the interdune sandstone does not have any oil residue.

1.2.2 Regional Setting and Petroleum Geology

The Denver Basin, also known as the Denver-Julesburg Basin, is located in eastern Colorado, southeast Wyoming, western Kansas and southwest Nebraska. The study area at Owl Canyon lies on the western edge of the Denver Basin (Fig. 1.2). The asymmetrical foreland Denver Basin covers approximately 180,000 km^2 and has an oval shape trending north-south. The western edge of the basin is steeply dipping, whereas the eastern edge is moderately dipping. Beneath the sedimentary rocks filling the Denver Basin are 1.6 billion year-old Precambrian rocks, approximately 4000 m deep along the basin axis. The basin was formed by the Laramide orogeny, beginning 67.5 million years ago. This tectonic activity folded the basin's rocks, created the existing structures, and formed the Rocky Mountains in the west (Higley and Cox, 2007).

According to the Colorado Oil and Gas Conservation Commission (COGCC) the accumulative oil production in Larimer county from conventional and unconventional reservoirs in 2017 was 676,281 BBL (barrel), and Gas Production was 2,472,681 MCF (million cubic feet). The oil production from all counties in Colorado in 2017 was 130,061,254 BBL and gas production was 1,679,130,968 MCF. The Wattenberg Oil Field is one of the most important oil fields north of Denver, Colorado. Oil, gas, and condensate in the Wattenberg Field are produced from Cretaceous intervals which are the J Sandstone, D Sandstone, Codell, Dakota- Lakota, Greenhorn, Niobrara, Larimer-Rocky Ridge, (Parkman), Hygiene (Shannon), and Terry (Sussex). Recently, horizontal drilling has focused on the Niobrara and Codell formations in the Wattenberg Field. The reserves in the Niobrara Formation in the Wattenberg region are between

3-4 billion barrels (Sonnenberg, 2015). The oil production from the Wattenberg Field in 2017 was 593,138 BBL and gas production was 2,347,856 MCF (COGCC).

The Wellington Oil Field in Larimer County, Colorado is the nearest petroleum production to the Ingleside Formation in the Owl Canyon area (Fig. 1.2). The Wellington Oil Field is approximately 8.2 mi to the east of the study area. The oil production from the Wellington Oil Field in 2017 was 15,506 BBL and gas production was 2,321 MCF (COGCC). The producing formations in the Wellington Oil Field are the Muddy J, J Sand, and the upper Jurassic Entrada Formation.

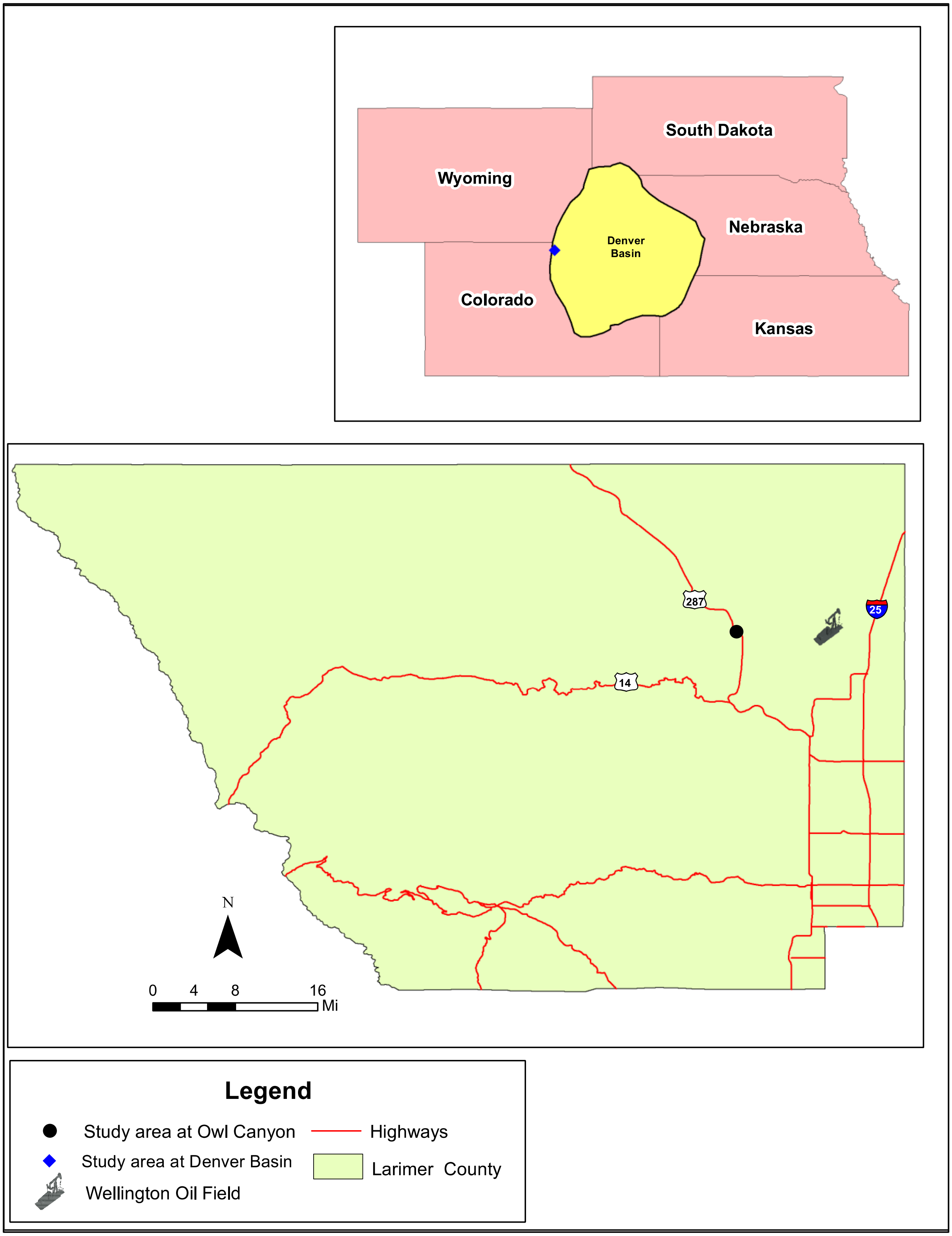

Figure 1-2. The Location of the study area in the Denver Basin (modified from http://ibis-live1.nrel.colostate.edu).

There are no petroleum occurrences described in literature in the Ingleside Formation, but there are occurrences described in the overlying Lyons Formation. The Permian Lyons Formation is the stratigraphically deepest formation in the Denver Basin that produces oil. Higley and Cox (2007) stated that petroleum generation in the hydrocarbon source rocks for the Lyons Formation probably occurred in early, middle or late Tertiary age. The hydrocarbon source rocks for the Lyons Formation are not well defined. However, it is possible that the black shale of Middle Pennsylvanian age in northern and eastern portions of the Denver Basin are the hydrocarbon source rocks for the Lyons Formation (Clayton, 1989, 1999). Hydrocarbon traps in the area of the Lyons Formation were probably created in Late Paleozoic or during Laramide orogeny time, and the generation, migration and accumulation of hydrocarbon occurred after this time. The Lower Permian Ingleside Formation probably experienced geologic events similar to those in the Permian Lyons Formation.

Lee and Bethke (1994) described the thermal maturity of the Pennsylvanian hydrocarbon source rocks adjacent to the Permian Lyons Formation. They calculated the TTI (Time temperature index), and used heat flow of 1.2, 1.5, 1.8 HFU (Heat flow unit). According to the calculation, oil generation occurred when the source rocks reach TTI values between 15 and 165, and vitrinite reflectance values between 0.65 and 1.3 %. Also, when the TTI is above160 the oil starts to crack to form natural gas. Further, the strata of the Denver Basin were not buried enough to generate hydrocarbons until the Cretaceous after the deposition of thick shale strata. They claimed that the oil maturation started in the late Cretaceous or early Tertiary, between 78 and 50 million years ago, and the initial petroleum was generated in the late Cretaceous about 68 million years ago. The migration of the oil from the source rocks to the reservoirs in the basin occurred mainly in the Tertiary (Lee and Bethke, 1994).

1.2.3 Sandstone Diagenesis

Diagenesis includes the processes that affect or alter sediments after deposition, such as compaction, precipitation of cement, grain replacement, and dissolution of cements and grains (Boggs, 2009). Studying these diagenetic processes and their effects is important for the petroleum industry because they can impact the hydrocarbon reservoir quality and properties (Rahman et al., 2011). Cementation and compaction generally increase with depth, causing a decline in the reservoir's porosity with depth. Conversely, excellent hydrocarbon reservoirs can survive high degrees of cementation and compaction if their porosity was enhanced by the destruction of grains and former cements (Taylor et al., 2010). Further, hydrocarbon migration pathways are restricted by the amount of porosity and its distribution in sandstone reservoirs, which can affect hydrocarbon production (Worden and Burley, 2003). Therefore, understanding the relationship between diagenetic processes and the timing of hydrocarbon migration is useful for hydrocarbon exploration and for predicting hydrocarbon accumulation.

Iron oxides minerals, including hematite, can occur in sandstones both as coatings on detrital grains and as cement (Boggs, 2009). Fredrickson (1978) observed hematite cement within the Fountain and Ingleside Formations in the Owl Canyon area, Colorado precipitated as rim cement. She suggested that hematite formed as a result of hornblende alteration in the Fountain Formation and biotite alteration in the Ingleside Formation, and that iron was redistributed by groundwater. Rainoldi et al., (2015) observed that hematite within a Late Cretaceous sandstone in the Neuquén Basin, Argentina occurred mainly as coatings on grains and precipitated between grain boundaries. Hematite there formed as a result of detrital grain alteration releasing Fe as a result of contact with oxidizing fluids in early diagenesis. They suggested that hematite coating the grains was deposited in early diagenesis and that hematite dissolution and whitening of red strata occurred by the movement of reducing fluids associated with hydrocarbons that migrated from deep in the basin through the red strata. They also observed that hematite coatings underlie quartz overgrowths, suggesting that hematite coatings occurred before quartz overgrowth cement.

Worden and Burley (2003) explained that carbonate cement is one of the most abundant cements in sandstone. Carbonate cement can precipitate during both eogenesis (early diagenesis) and mesogenesis (late diagenesis). A source of calcium is required for the precipitation of calcite cement, and a source of both calcium and magnesium is required for the precipitation of dolomite cement. The dissolution of carbonate skeletal framework in sandstone is one source for Ca and Mg. Other sources for Ca and Mg are the smectite-illite transformation and the dissolution of Ca-feldspar. An additional source is the alteration of mafic volcanic rocks by the subsurface water, which can release high volumes of Ca and Mg to form carbonate cement (Boggs, 2009). Stylolites that formed by carbonate dissolution along grain boundaries is another possible source for calcite cement (Land and Dutton, 1978; Bjørlykke, 2010).

Imam and Shaw (1987) suggested that recrystallization of a large amount of skeletal debris formed early poikilotopic cement in sandstone in the Surma Group from the Bengal Basin. They reported that the detrital grains in some samples appear to float with low grain contacts in very early poikilotopic Fe-calcite cement. Walderhaug (1990) stated that poikilotopic calcite cement precipitated prior to the precipitation of quartz overgrowth cement in a Jurassic sandstone from offshore Mid-Norway. He also found that where the pore spaces are filled with poikilotopic cement, it surrounds authigenic kaolinite cement. Islam (2009) studied sandstone diagenesis of the Titas gas field, Bengal Basin. He observed that calcite cement is the most abundant cement in most samples and precipitated as a poikilotopic cement. He stated that in thin sections the poikilotopic cement appeared to form in early diagenesis and block fluid movement by filling the pore spaces. Rahman et al. (2011) interpreted the diagenesis of the Surma Group sandstones in the Bengal Basin. They stated that some of the carbonate cement they observed was poikilotopic, and that the poikilotopic cement precipitated early, reducing both the porosity and permeability. They explained that the poikilotopic cement precipitated between loosely packed grains, filling large pores, or partly replaced grains. They observed that this cement occurred between grains that were not impacted by major compaction and precipitated before quartz cementation.

McBride (1989) reviewed quartz cementation, which he stated is one of the most important and common cements in sandstones. According to McBride, silica cement is controlled by sedimentary basin type and can be prevented by minerals, including clay minerals, coating the sand grains and by hydrocarbon emplacement. Grain composition, fluid composition, flow rate and pathways, and time of residence in the silica mobility zone can restrict the quantity of silica cement in sandstones. He indicated that silica cement is precipitated mainly at burial depths between 1 to 2 km and at a temperature range of 40-90 °C, but could precipitate at burial depths of 4 km or even 6 km. He also noted that quartz cement precipitated at temperatures between 60-100 °C in sandstones in quickly subsiding basins. He suggested that minor silica sources include older units affected by low grade metamorphism and silica from meteoric water. Other silica sources in sandstone include the dissolution and alteration of feldspar grains, quartz grains dissolved by pressure solution, silicate minerals replaced by carbonate, clay mineral transformations, and dissolution of quartz and opal grains.

Bjorlykke and Egeberg (1993) discussed the influence of quartz cementation on sandstone reservoir quality. They proposed that quartz cementation occurs more during deep burial, which is different from some previous studies that suggested quartz cementation probably occurred at shallower depth and at low temperature. They suggested that the sources of silica for quartz cementation at depths between 1.5 and 2.0 km and temperatures of 70-80 °C are opal CT and amorphous silica, whereas in deeper sandstones pressure solution and silicate minerals reactions are the major sources for silica cement. In sandstones from the North Sea Basin, they found from fluid inclusion analysis that most quartz cement formed at temperatures above 90 - 100°C, and probably continued precipitating slowly after petroleum emplacement. The formation of quartz cement in sandstone reservoirs from externally derived silica driven by advective transport requires significant volumes of pore water flow. Hence, moving a large amount of silica by advective transport through the sandstone will cause cementation that will damage the permeability of the sandstone. Finally, they calculated that rising pore water driven by convective heat transfer will more rapidly increase the carbonate removal than the precipitation of quartz cement, and the pore water transported by compaction will more rapidly dissolve carbonate than precipitate quartz cement. Worden and Burley (2003) stated that commonly quartz cementation in sandstone forms at temperature ranging between 80 –100°C. Taylor et al. (2010) suggested that the assumption that hydrocarbon pore fluids prevent quartz cementation which damages the porosity is not proved yet. Rahman et al., (2011) observed that quartz cement in sandstone samples from the Surma Group in the Bengal Basin is more abundant in deeply buried sandstones and is rare in sandstones from shallower depths. They observed quartz cement in sandstone from depths between 2000 and 3400 m, and suggested that pressure solution of quartz grains was the major source of the silica.

Diagenetic changes in feldspar abundance and type have been noted in numerous studies. Land and Dutton (1978) stated that some detrital grains, including feldspar, were partially or completely replaced by calcite. In addition, they noted that some cements precipitated in secondary porosity suggesting that these cements precipitated in a late stage after the dissolution of the feldspar. Also, feldspar destruction occurred as temperature increased with burial depth. Land and Milliken (1981) described the importance of feldspar alteration in sandstone of the Frio Formation, Texas Gulf Coast. They noted that K-feldspar decreased with depth and in deep burial below 4,267 m much K-feldspar was dissolved or albitized. Approximately 15% of the rock volume was impacted by feldspar replacement and dissolution. The albitization of Ca-feldspar and K-feldspar is important and has consequences for other processes, including the formation of silica and carbonate cements, and creating secondary porosity. Milliken et al. (1994) used elemental and isotopic data to interpret elemental mobility in sandstones of the Frio Formation. They observed that some elements were lost or added during the alteration, replacement, and dissolution of feldspar in samples from burial depths between 0.9-4.3 km. The whole rock lost about 2-3 weight percent of K_2O due to K-feldspar dissolution and albitization, although the amount of Na_2O held constant with increased feldspar alteration during burial. Wilkinson et al. (2001) studied K-feldspar destruction in rift and passive margin sandstones from two different rift basins in the North Sea and the passive margin basin of the Gulf Coast. They concluded that arkosic sandstone at a burial depth from about 1.5 to 4.5 km displayed a systematic reduction in K-feldspar abundance, commonly by dissolution which reduced the rock volume by about 15%. Arkosic sandstones turned into quartz arenite sandstones and the secondary porosity increased due to the destruction of K-feldspar with depth. These changes indicate that the dissolution of K-feldspar is an essential process in deep burial. They also suggested that changes in source rock provenance were not responsible for the K-feldspar reduction with depth.

In sandstones, kaolinite cement can fill pore spaces and be formed by feldspar replacement and alteration. Land and Dutton (1978) determined that at burial depths of about 1.4 km kaolinite cement formed as a result of H^+ released from the replacement of detrital feldspar. Imam and Shaw (1987) observed that authigenic kaolinite cement was precipitated in pore spaces and formed by feldspar alteration. They suggested that the generation of kaolinite cement is favored by the presence of acidic pore fluids, with feldspar as the source of Al and Si to form this cement. A possible source for the acidic water to form kaolinite cement is hydrocarbon maturation in adjacent source rocks. Worden and Burley (2003) suggested that the precipitation of kaolinite requires low ionic strength water and low pH that can also be present during weathering. Islam (2009) pointed out that feldspar alteration was responsible for some kaolinite cement. Taylor et al. (2010) suggested that feldspar dissolution causes kaolinite cement precipitated in pore spaces as authigenic cement and it causes little change in the porosity, but it causes major reduction in permeability.

Schmidt and McDonald (1979) discussed the importance of sandstone secondary porosity. Important amounts of hydrocarbon reserves are found in sandstone secondary porosity. They observed that a vast amount of secondary porosity is formed by mineral dissolution, especially dissolution of carbonate minerals. However, the rate of carbonate removal is less than the precipitation of carbonate in sandstone. They suggested that primary hydrocarbon migration probably occurs when secondary porosity is created. The amount of secondary porosity declines with deep burial, but more slowly than primary porosity. Wilkinson et al. (2001) observed that compaction increased with depth, causing a decline in secondary porosity which is in some sandstones less than 10%. Taylor et al. (2010) studied the impact of diagenetic processes on sandstone reservoir quality. They suggested that the dissolution of cement and frame-work grains is responsible for forming minor secondary porosity, approximately less than 2%.

CHAPTER 2
METHODOLOGY

The Owl Canyon Ingleside roadcut was studied and described in detail. The 42.2 m thickness of the Ingleside Formation outcrop was divided into fourteen distinct beds based on variations in lithology and color. The thickness of each bed and the horizontal length of the roadcut were measured with a100-meter tape, whereas strike and dip of beds were measured by using a Brunton compass. Features such as lithology, color, thickness, sedimentary structures, and deformational structures were recorded for each bed. The Munsell color system was used to identify each bed's color. Twenty-nine rock samples were collected from the roadcut to make twenty-nine thin sections, and the stratigraphic position of each thin section is listed in Table 2.1. The samples for the thin sections were collected from the upper part to the lower part of the roadcut, with approximately a five foot stratigraphic increment from one sample to another.

Thin sections were prepared with blue epoxy, to identify porosity, and stained with alizarin red to distinguish calcite from dolomite. Bitumen was identified in thin sections in plane-polarized light. Bitumen is black or dark colored in plane-polarized light (Shi et al., 2017), entirely opaque and amorphous. Bitumen occurs in these samples always as a coating and as a discontinues layer (Ridley, personal communication). The thin sections were described in detail to determine the diagenetic history, mineralogy, porosity, and possible hydrocarbon migration history. The diagenetic events that impacted the Ingleside Formation are cementation, compaction, feldspar dissolution and alteration, and the relative paragenetic sequence is based on the petrographic observations of spatial relationships among the products of these diagenetic processes (Fig 4.1). Fourteen thin sections of the twenty-nine thin sections were selected for point counting. These fourteen thin sections represent sandstones while the other fifteen thin sections are carbonate, so were not included in point counting. The point counting was performed on a mechanical stage moved in a grid pattern across a representative part of the thin section. At least 250 points were recorded to determine the abundance of mineral types, cements, matrix, and porosity in each thin section.

In addition to the samples taken for thin sections, sixteen hand samples were taken from the outcrop for analysis by handheld XRF (X-ray fluorescence). The samples for XRF analysis were taken from all fourteen beds (Table 2.1). One hand sample was collected from each bed, except for three samples collected from bed 3. The hand samples for geochemistry were selected to represent the dominant rock type in each bed. The samples were collected from fresh-appearing rocks, although the rocks were probably somewhat affected by modern weathering. The samples were cut and polished to prepare them for XRF analysis.

The model of the XRF instrument is Delta Premium (DP-6000) manufactured by Olympus IMS. The XRF device can be used to identify most of the major elements (Mg and heavier) and many trace elements (Table 2.2), but not rare earth elements, Na, or elements lighter than Na. Therefore, it gives useful, but incomplete, information about bulk chemical composition. The chosen sample is placed in a housing case designed to contain the sample and after mounting the XRF and closing the lid of the housing case the XRF analyzer emits an x-ray beam that interacts with the sample. A cable connects the XRF with a computer, allowing the user to read and export the data. For this analysis approximately four XRF analyses were recorded from each hand sample to determine the chemical variation and chemical composition throughout the outcrop. The duration of analysis for each spot in the rock lasted for two minutes.

The Delta Premium tool has an advanced accelerating voltage (40kV tube), and large area (SDD) detector (Silicon Drift Detector). The tool has a powerful 4W x-ray tube, with 200 μA current (max). Standards were not used in this analysis. Because of the limitations of the portable instrument and because standards were not used, the data generated by the XRF analysis are not very accurate and should be regarded qualitative and not quantitative. The reason that standards were not used is that appropriate standards were not readily available, and the goal for the geochemistry was qualitative information. The raw data for the XRF analysis for each major element were analyzed and converted to weight percent oxide whereas the trace elements were in percent and required conversion to ppm (parts per million). The values of the limits of detection given in Table 2.2 were obtained under optimal conditions by the manufacturer for a particular type of sample and likely are lower than the actual detection limits applicable to the present study. To partially evaluate the analyses generated, the sum of the major element oxides, combined with CO_2 calculated by assigning all CaO and MgO to carbonate minerals (Table 4.1), was calculated for each analysis. This assessment was done to evaluate the accuracy of the data by examining whether the totals for the analyses were reasonable. Data for evaluating the additional weight of H_2O and Na_2O in the samples was not available.

Table 2.1. The stratigraphic position of all rock samples for thin sections (29 samples) and geochemistry (16 samples). The samples are listed from the top (bed 14) to the bottom (bed 1) of the exposure. The stratigraphic position is defined as height above the base of the formation.

Thin Section No	Bed No	Geochemistry Sample No	Bed No	Approximate Stratigraphic Position for Geochemistry Samples (m)
ING-1	Bed-14	GS-14	Bed-14	40.4
ING-2				
ING-5	Bed-13	GS-13	Bed-13	37.7
ING-6				
ING-7	Bed-12	GS-12	Bed-12	35.8
ING-8				
ING-9	Bed-11	GS-11	Bed-11	34.1
ING-10				
ING-11	Bed-10	GS-10	Bed-10	30.1
ING-12				
ING-14				
ING-15	Bed-9	GS-9	Bed-9	25.9
ING-16				
ING-17				
ING-18	Bed-7	GS-8	Bed-8	24.4
ING-19		GS-7	Bed-7	22.5
ING-20				
ING-21	Bed-6	GS-6	Bed-6	20.4
ING-22				
ING-23	Bed-5	GS-5	Bed-5	19.3
ING-24	Bed-4	GS-4	Bed-4	16.6
ING-25				
ING-26				
ING-28	Bed-3	GS-3C	Bed-3	14.4
		GS-3B		12.3
ING-30		GS-3A		10.3
ING-32	Bed-2	GS-2	Bed-2	4.1
ING-33				
ING-34	Bed-1	GS-1	Bed-1	1
ING-35				

Table 2.2. Lower limits of detection (LODs) in ppm published by the manufacturer for XRF Delta Premium (DP-6000) using a rhodium x-ray tube (Rh). www.olympus-ims.com.

Elements	Limits of Detection
Mg	10000
Al	1400
Si	800
P	120
S	150
Cl	-
K	50
Ca	35
Ti	10
V	10
Cr	9
Mn	7
Fe	20
Ni	10
Cu	6
Zn	3
W	10
Hg	5
Au	4
As	3
Se	2
Pb	4
Rb	2
U	6
Sr	2
Y	2
Zr	2
Nb	1
Th	6
Mo	2
Ag	12
Cd	9
Sn	14
Sb	13
Ba	-
La	-
Ce	-
Pr	-
Nd	-

CHAPTER 3
RESULTS

3.1 Roadcut Description

The Ingleside Formation is well-exposed in a roadcut along U.S. Highway 287 just south of Owl Canyon in northern Colorado, approximately 17.4 miles north of the city of Fort Collins, Colorado (Fig. 3.1). The roadcut has exposures on both sides of the road; the northeast side was sampled for this study and is described here. In the exposure studied (Fig. 3.2), the lower 53% of the Ingleside Formation can be divided into fourteen beds (Fig. 3.3), based on variations in composition, color, and texture from the base to the top of the outcrop. These beds are well exposed, and composed variously of sandstone, limestone, dolomite, and siltstone. For purposes of this study, the beds are numbered from 1 to 14, listed from the bottom to the top of the exposed Ingleside.

The horizontal length of the exposure is around 220 m, whereas the stratigraphic thickness of all fourteen beds is approximately 42.2 m. The strike and the dip of the outcrop are approximately 115°N/25°E. The Ingleside Formation sandstone is pink, red or orange whereas the limestone is light grey, the dolomite is white or pink, and the siltstone is red. Some deformational structures and sedimentary structures were recognized in the outcrop including fractures, joints, stylolites, bedding, crossbedding, veins, sand lenses, and vugs.

Figure 3-1. Index map showing the location of the Ingleside roadcut exposure at Owl Canyon, Larimer County, Colorado. The red rectangle within the photo insert defines the study area.

Figure 3-2. The Ingleside outcrop at Owl Canyon, Larimer County, Colorado.

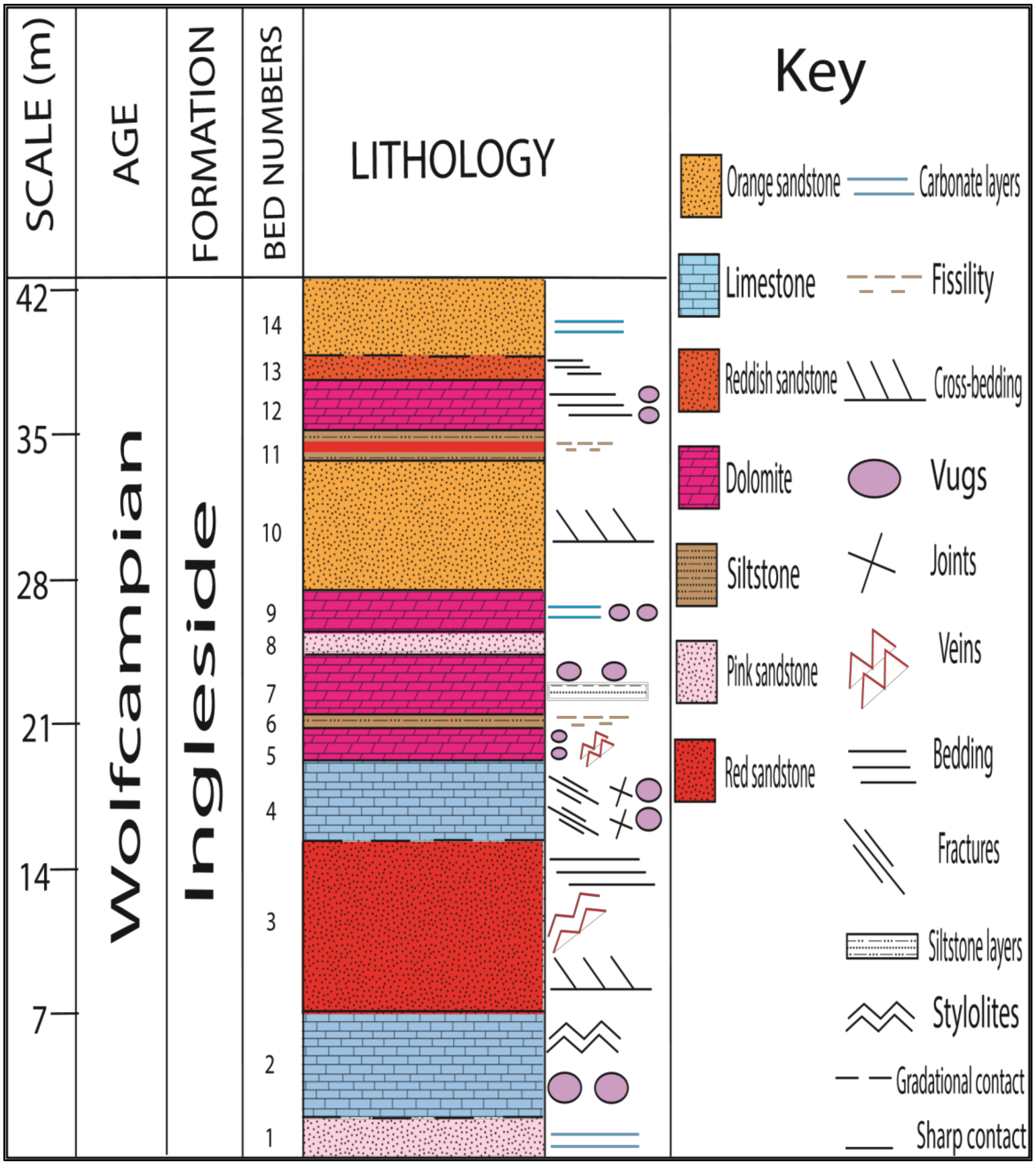

Figure 3-3. Measured stratigraphic column of the Ingleside roadcut, Hwy. 287, Owl Canyon area, Larimer County, Colorado.

3.2 Bed Descriptions

Bed 1:

This is the stratigraphically lowest bed exposed in the roadcut (Fig. 3.4). It consists of massive sandstone, and the exposed thickness is approximately 2 m. The bed's colors are 5YR

8/3 and 2.5YR 5/4 in the Munsell color system. The bed contains a thinly bedded dolomite lens, approximately 0.90 m thick, that does not extend laterally through the bed and is 5YR 8/2 in the Munsell color system.

Figure 3-4. Bed 1 is a banded (yellow arrows) massive sandstone. 32.3 cm hammer for scale.

The sandstone bed contains some light grey bands parallel to bedding, carbonate clasts that range from 0.5 cm to 4.5 cm, and joints and fractures. At the top the bed also shows evidence of possible bioturbation, perhaps a root cast or a large burrow (Fig. 3.5). No other sedimentary structures were observed in this bed. The contact of this bed with the overlying limestone (bed 2) is gradational which is represented by progressively increasing in calcite content.

Figure 3-5. A structure in bed 1, possibly a root cast or large burrow. 14.6 cm pencil for scale.

Bed 2:

Bed 2 consists of massive limestone (Fig. 3.6). The bed's color is 5YR 6/1 in the Munsell color system. The bed contains some crystalline calcite in sparse vugs which, range in size from approximately 1 cm to 3.5 cm in diameter. (A vug is a cavity in a rock lined with minerals that may have formed when water flowing through the rock is saturated with respect to particular minerals). The bed contains some joints, fractures, stylolites, and sand lenses. The stylolite surfaces are approximately parallel to bedding (Fig. 3.7). No other structures were observed. The contact of this bed with overlying bed 3 is sharp. The upper surface of bed 2 is uneven and is probably an erosional surface; there is variation in thickness of the bed from approximately 3.2 m to 4.2 m.

Figure 3-6. Bed 2 consists of thick and massive grey limestone. Note the fractures extending through the bed. 14.7 cm pen used for scale.

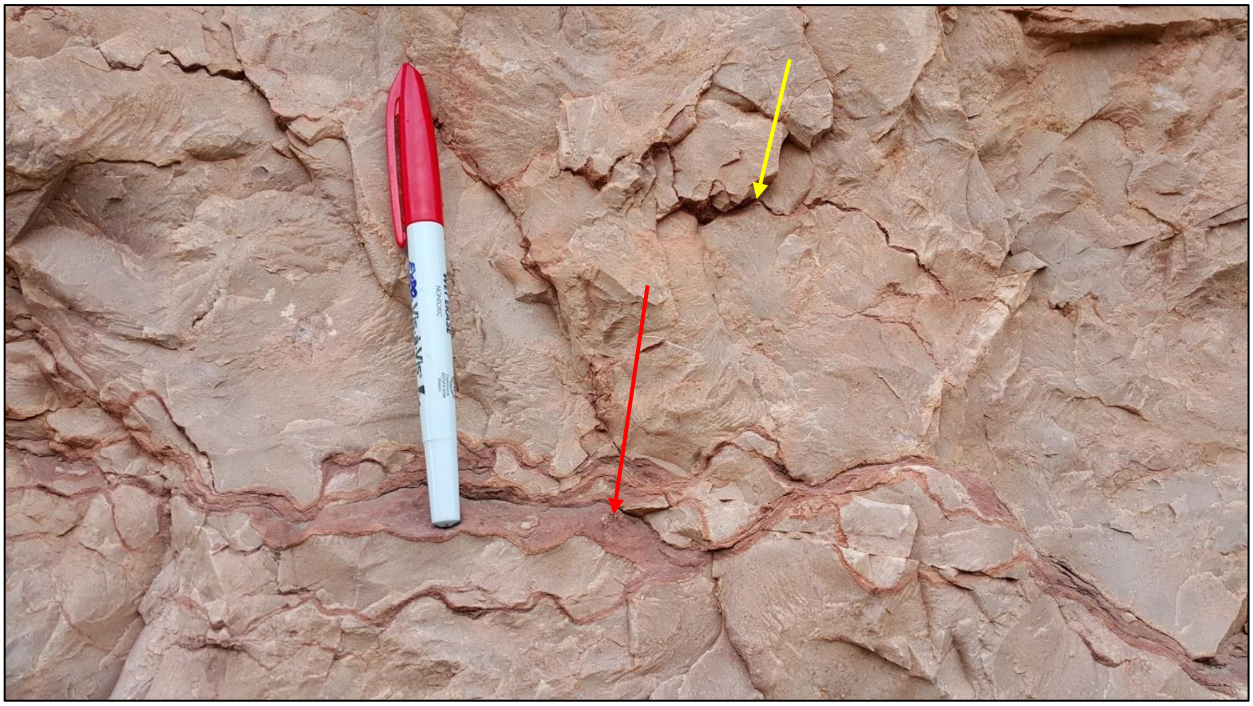

Figure 3-7. Stylolites (yellow arrow) and sand lenses (red arrow) in bed 2. 13 cm pen is for scale.

Bed 3:

This bed is the thickest in the outcrop at approximately 6.2 m to 8.2 m (Fig. 3.8). It consists of massive sandstone with limited displays of sedimentary and other structures. These structures include cross bedding in a few places near the bottom of the bed, bedding, veins filled with calcite, joints, and fractures. The bed shows variation in color, 10R 4/6 and 10R 7/3 in the Munsell color system. Near the contact with the overlying limestone of bed 4, bed 3 contains a few limestone clasts, and they are about 5 cm long. The contact of bed 3 is gradational with overlying bed 4 which is represented by progressively increasing in calcite content. The upper surface of bed 3 is uneven, possibly an erosional surface, which causes a variation in thickness (Fig. 3.9).

Figure 3-8. Bed 3 massive and thick red sandstone. 32.3 cm hammer for scale.

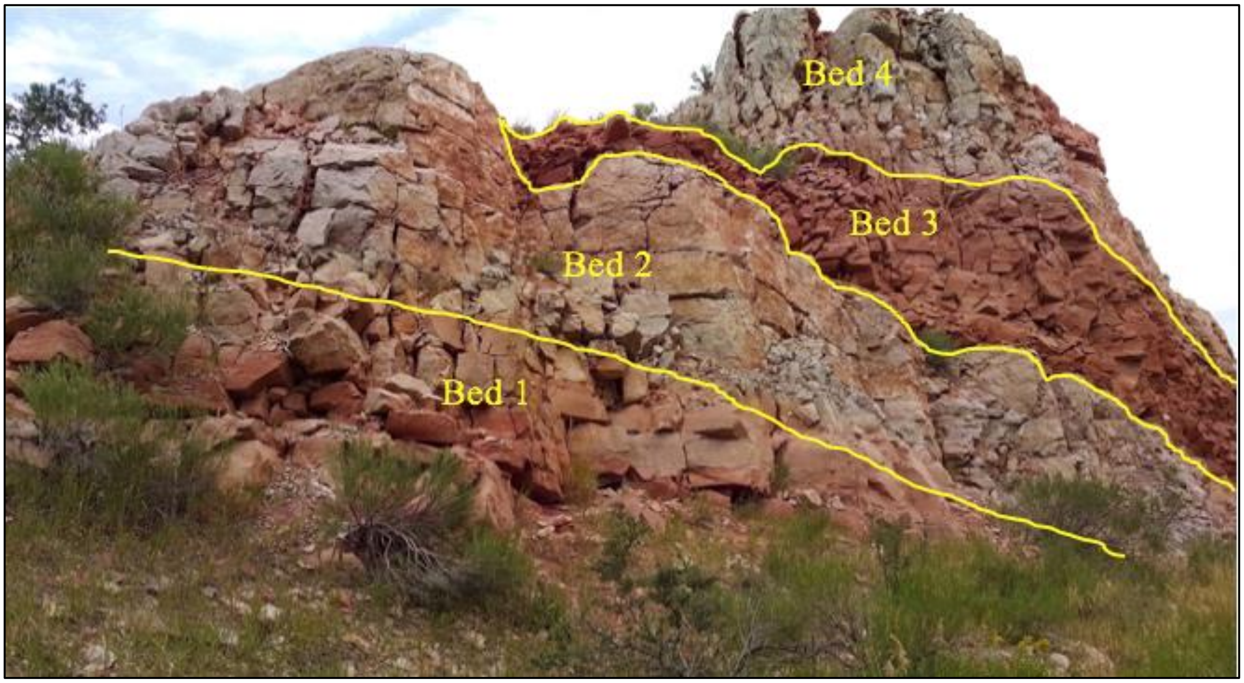

Figure 3-9. The four lowest beds in the exposure. Pink bed 1 at the base is in gradational contact with grey bed 2. Note the sharp contact between bed 2 and bed 3 (the red sandstone) and the gradational contact between bed 3 and the overlying limestone, bed 4.

Bed 4:

This bed consists of thick, massive limestone (Fig. 3.10). The bed's color is 7.5 YR6/1 in the Munsell color system. The non-planar upper surface of bed 4 is probably an erosional surface and causes variation in thickness from approximately 1.4 m to 4.4 m.

Figure 3-10. Bed 4 massive grey limestone. Note the vugs that are spread throughout the bed (yellow arrows). 13.3 cm marker used for scale.

Vugs are more common in bed 4 than in bed 2, and their diameters are approximately 0.5 cm to 4.5 cm. The bed also contains some joints and fractures, but no sedimentary structures can be observed in this bed. The contact with the overlying dolomite (bed 5) is sharp.

Bed 5:

The bed is dolomite approximately 0.5 m to 1 m thick (Fig. 3.11). The bed's color is 7.5YR 8/2 in the Munsell color system. The upper surface is uneven, possibly an erosional surface that caused a variation in thickness, and the bed is discontinuous laterally (Fig. 3.13). There are vugs approximately 0.5 cm to 4 cm in diameter, veins filled with calcite, fractures, and joints associated with this bed. In one place there are some calcite crystals, mostly about 0.5 cm across, that are on the surface of the exposure and do not extend into the rock. The contact between this bed and the overlying siltstone bed (bed 6) is sharp.

Figure 3-11. Bed 5 consists of pinkish white dolomite. 32.3 cm hammer for scale.

Bed 6:

This bed consists of siltstone (Fig. 3.12). The center of the bed is a thin layer of dolomite approximately 0.40 m, with thin layers of siltstone on either side of it. The thickness of the lower siltstone layer is about 0.30 m and the upper layer is about 0.50 m. The siltstone color is 10R 4/6 and the interbedded dolomite color is 10R 6/6 in the Munsell color system. The siltstone is fragile and soft. No distinctive sedimentary or deformational structures were observed in this bed. The contact of this bed with the overlying dolomite (bed 7) is sharp and in places appears erosive. The non-planar lower surface of bed 6 is probably an erosional surface and causes variation in thickness from approximately 0.70 m to 3 m thick (Fig. 3.13).

Figure 3-12. Red fissile siltstone and the thin layer of light red dolomite of bed 6. 32.3 cm hammer for scale.

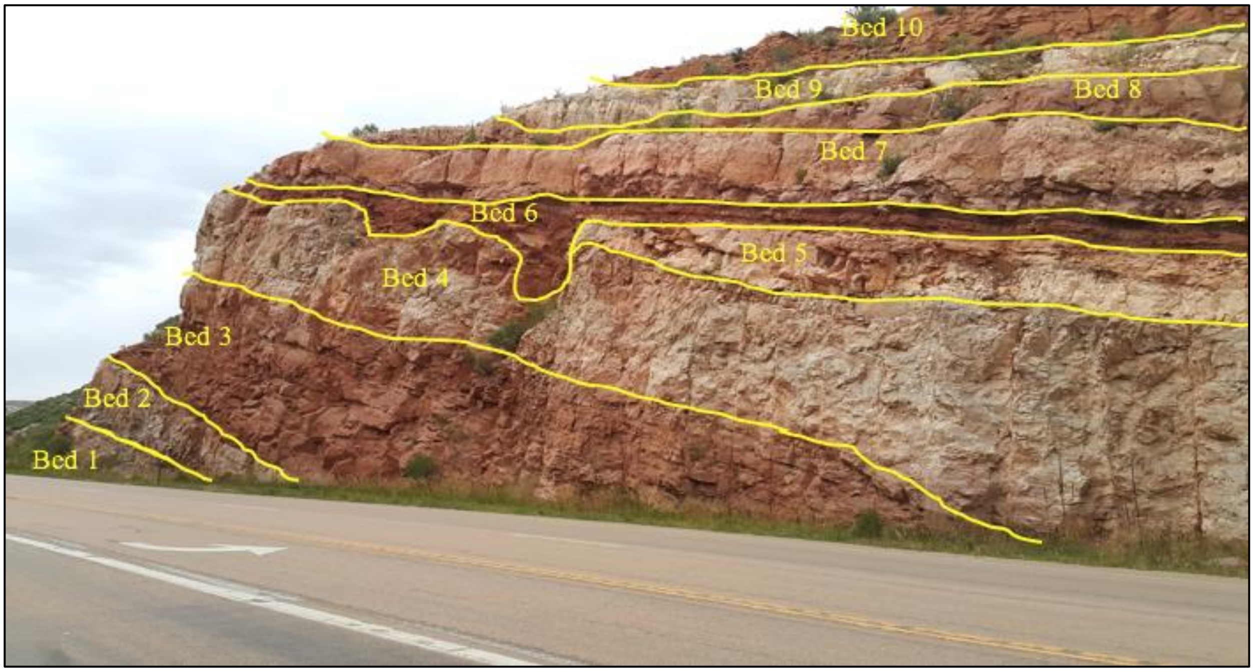

Figure 3-13. Beds 1 through 10 in western part of roadcut.

Bed 7:

This bed comprises massive dolomite. The color is 10R 8/4 in the Munsell color chart. The bed is approximately 2.5 m to 3 m thick (Fig. 3.14). The bed contains some vugs, joints, and fractures, but does not contain other distinctive structures. Most of the vugs are approximately 0.5 cm to 4 cm in diameter. The upper surface of the bed is uneven, possibly an erosional surface, which causes variation in thickness. The upper boundary with the pale red sandstone bed (bed 8) is sharp (Fig. 3.13).

Figure 3-14. Bed 7 massive pink dolomite. Note the vugs in the upper part of the bed (yellow arrows). 13.3 cm marker for scale.

Bed 8:

This bed consists of thinly bedded sandstone. The color is 10R 6/4 in the Munsell color chart. The bed is approximately 0.5 m to 0.9 m thick, which is the thinnest sandstone bed in the outcrop (Fig. 3.15). There were no distinctive sedimentary structures observed in this bed. The bed contains some fractures. The contact with the overlying dolomite bed (bed 9) is sharp in some places and gradational in others which is represented by progressively increasing dolomite content.

Figure 3-15. Thinly bedded pale red sandstone of bed 8 in gradational contact with the overlying white dolomite bed (bed 9). 14.7 cm pen is for scale.

Bed 9:

This bed comprises massive dolomite, approximately 0.5 m to 2 m thick (Fig. 3.16). The color is 7.5YR 8/1 in the Munsell color chart. It differs from the other dolomite beds in the outcrop by hosting the most and the largest vugs, some of which are approximately 15 cm in diameter. In addition, there are fractures in some places. Near the top of the bed dolomite is interbedded with light grey limestone layers. The contact with the overlying sandstone bed (bed 10) is sharp in some places and gradational in others which is represented by progressively increasing sand content (Fig. 3.13).

Figure 3-16. Bed 9 comprises massive white dolomite shown in the upper part of the photo. Note the large vugs at the top (yellow arrows).

Bed 10:

This bed consists of massive sandstone, cross-bedded in places (Fig. 3.17). The color is 2.5YR 6/6 in the Munsell color chart. The bed is about 6.5 m thick, and is the second thickest bed in the outcrop after bed 3. It shows a few joints and fractures in some areas. The bed has a sharp contact with the overlying siltstone bed (bed 11).

Figure 3-17. Thick, cross-bedded light red sandstone of bed 10. 14.6 cm pencil for scale.

Bed 11:

This bed consists of interbedded siltstone and sandstone (Fig. 3.18). The thickness of the lowest siltstone layer is approximately 0.23 m, the thickness of the sandstone layer above it is about 0.22 m. The middle siltstone layer is about 0.23 m thick, the sandstone above it is around 0.35 m and the upper siltstone layer is approximately 0.50 m thick. The siltstone color is 10R 4/4, and the sandstone color is 10R 6/6 in the Munsell color chart. The siltstone is fissile and soft and the interbedded sandstone shows bedding. The contact with the overlying dolomite bed (bed 12) is sharp (Fig. 3.19).

Figure 3-18. Bed 11 shows weak red fissile siltstone interbedded with light red sandstone. 13.3 cm marker for scale.

Figure 3-19. Beds 10 through 14 in eastern part of exposure.

Bed 12:

This bed comprises dolomite (Fig. 3.20). It is approximately 1.8 m thick, and like the other carbonate beds it contains a few vugs, approximately 0.5 cm in diameter. The colors are 2.5YR 8/4 and 2.5YR 8/2 in the Munsell color chart. This bed displays internal bedding and some fractures. The contact with the overlying sandstone bed (bed 13) is sharp (Fig. 3.19).

Figure 3-20. Bed 12 comprises pinkish white dolomite. 14.6 cm pencil for scale.

Bed 13:

This bed consists of sandstone (Fig. 3.21). The bed is approximately 2 m thick, and shows internal bedding. The color is 2.5YR 5/4 in the Munsell color chart. It contains some fractures. There are no other distinctive deformational or sedimentary structures associated with this bed. The contact with the overlying orange sandstone (bed 14) is gradational (Fig. 3.19).

Figure 3-21. Bed 13 is made up of reddish brown sandstone. 14.6 cm pencil for scale.

Bed 14:

This is the stratigraphically highest bed exposed in the roadcut and consists mainly of sandstone (Fig. 3.22). The part of the bed present in the exposure is approximately 3.5 m thick. This bed shows internal bedding, especially in the upper portion, and thinly bedded carbonate layers. The colors are 2.5YR 8/4 and 2.5YR 6/6 in Munsell color chart. The sandstone in this bed is more friable than the sandstone in the other beds in the outcrop. No other distinctive sedimentary structures were observed in this bed.

Figure 3-22. Bed 14 consists mainly of light red sandstone. (26.7 cm * 20.3 cm) notebook for scale.

3.3 Summary of Outcrop Observations

Overall, the Ingleside outcrop is composed of approximately 56% sandstone, 20% limestone, 20% dolomite, and 4% siltstone. The roadcut contains some features related to carbonate. These features include some small veins filled with calcite, calcite vugs that have variable size and occur throughout the carbonate beds, carbonate layers found in some sandstone beds, limestone clasts, and a small patch of calcite crystals that are on the surface exposure of bed 5. Sedimentary structures observed in the roadcut include bedding, cross-bedding, bioturbation, and sand lenses. In addition to the sedimentary structures, joints, fractures, and stylolites, were noted. The contacts between beds vary from sharp to gradational and planar to uneven.

3.4 Petrography

3.4.1 Thin Sections Observations

Thin sections are described in detail, and the numbering for the thin sections is organized from the top to the bottom of the Ingleside outcrop (Table 2.1).

ING- 1 (Bed 14):

This sample is composed mainly of moderately well sorted, very fine to fine sand grains. These grains consist mainly of quartz and minor K-feldspar, albite, chert grains (Fig. 3.23), zircon, and opaques. Also, the sample contains laminations defined by concentrations of the very fine sand grains.

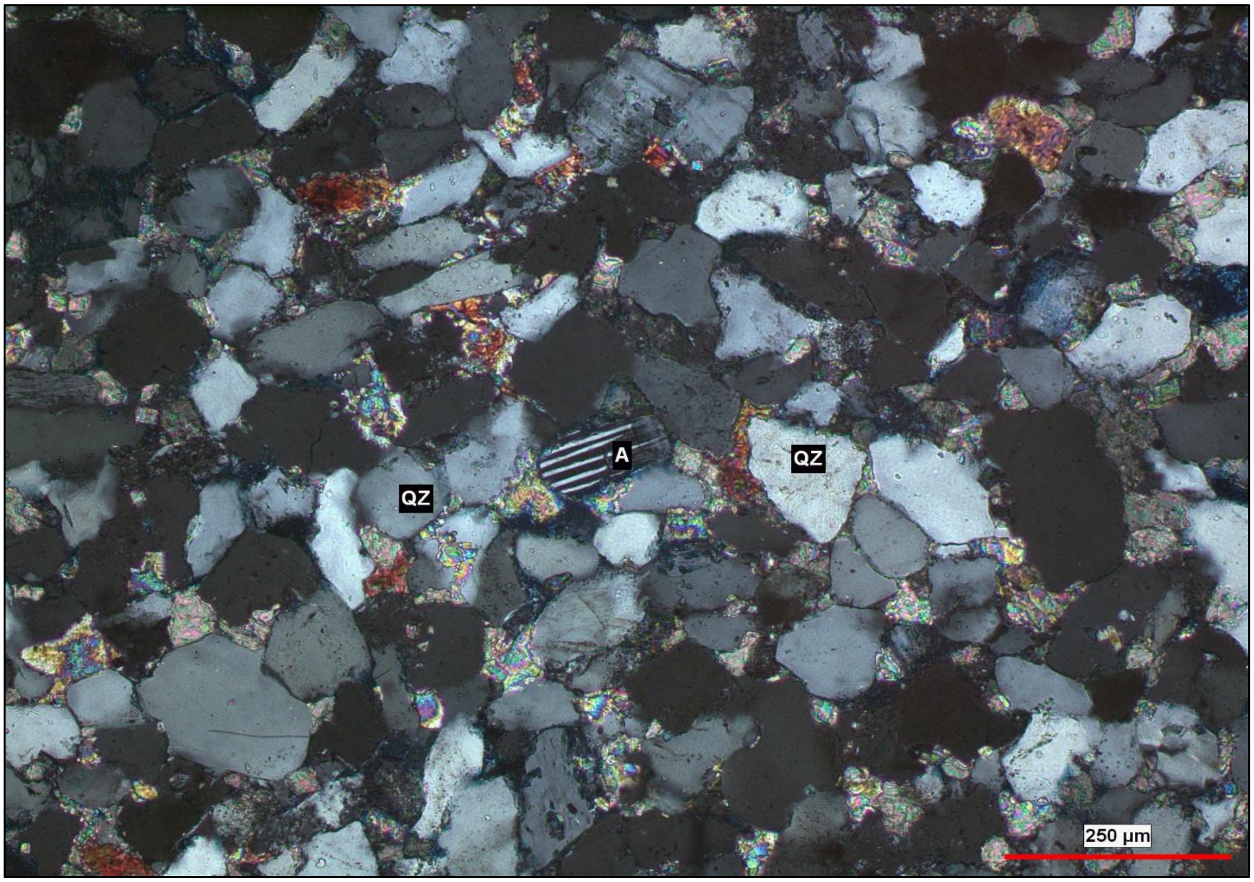

Figure 3-23. Sample ING-1. Albite grain (A) with polysynthetic twinning and abundant quartz grains (QZ). The grains are cemented with calcite (stained red) and dolomite cement. Photo is in cross polarized light.

The grains vary in roundness from angular to sub-rounded, but most are sub-rounded and have low sphericity while a few have high sphericity. Furthermore, the grain contacts are either point, long, or concavo-convex; concavo-convex contacts are the most common. The sample is well-cemented with dolomite, calcite (Fig. 3.24), minor quartz overgrowths, hematite, and kaolinite (Fig. 3.25). However, pore-filling dolomite cement is more abundant in this sample than in the others, and varies little in size and distribution throughout the sample. The grains cemented with quartz overgrowths are rimmed with hematite cement that sits between the primary grains and the quartz overgrowths (Fig. 3.26). The sample is texturally sub-mature, based on the moderate sorting, angular and sub-rounded grains, and the lack of clay.

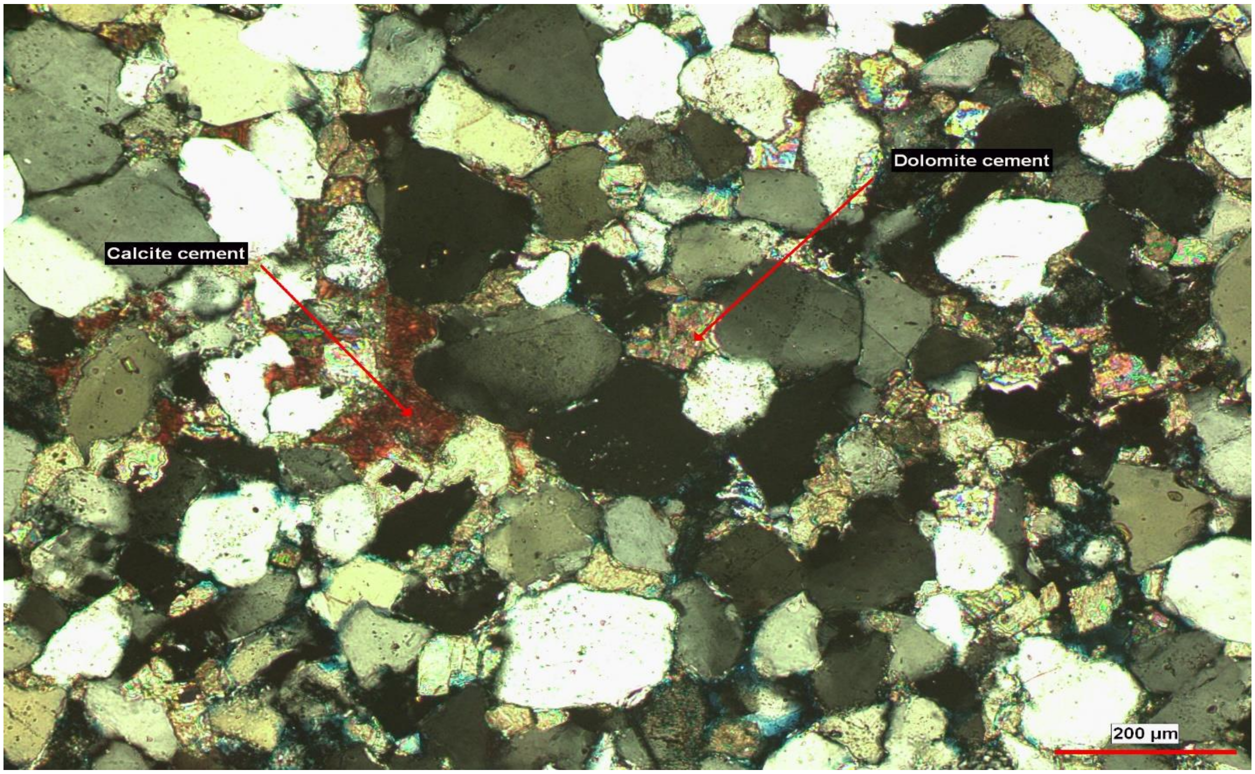

Figure 3-24. Sample ING-1. Sample in cross polarized light showing dolomite and calcite cements.

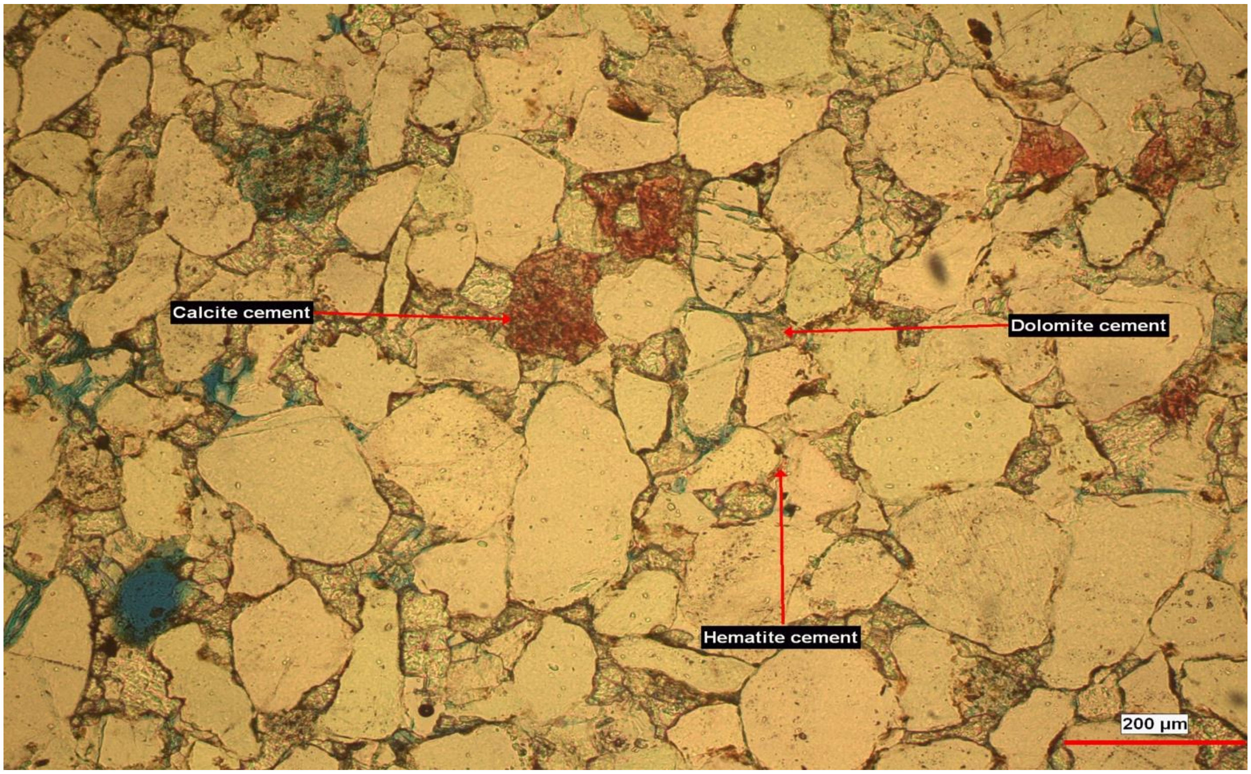

Figure 3-25. Sample ING-1. Sample in plane-polarized light showing dolomite calcite, and hematite cement. Note the cements are present with compacted grains.

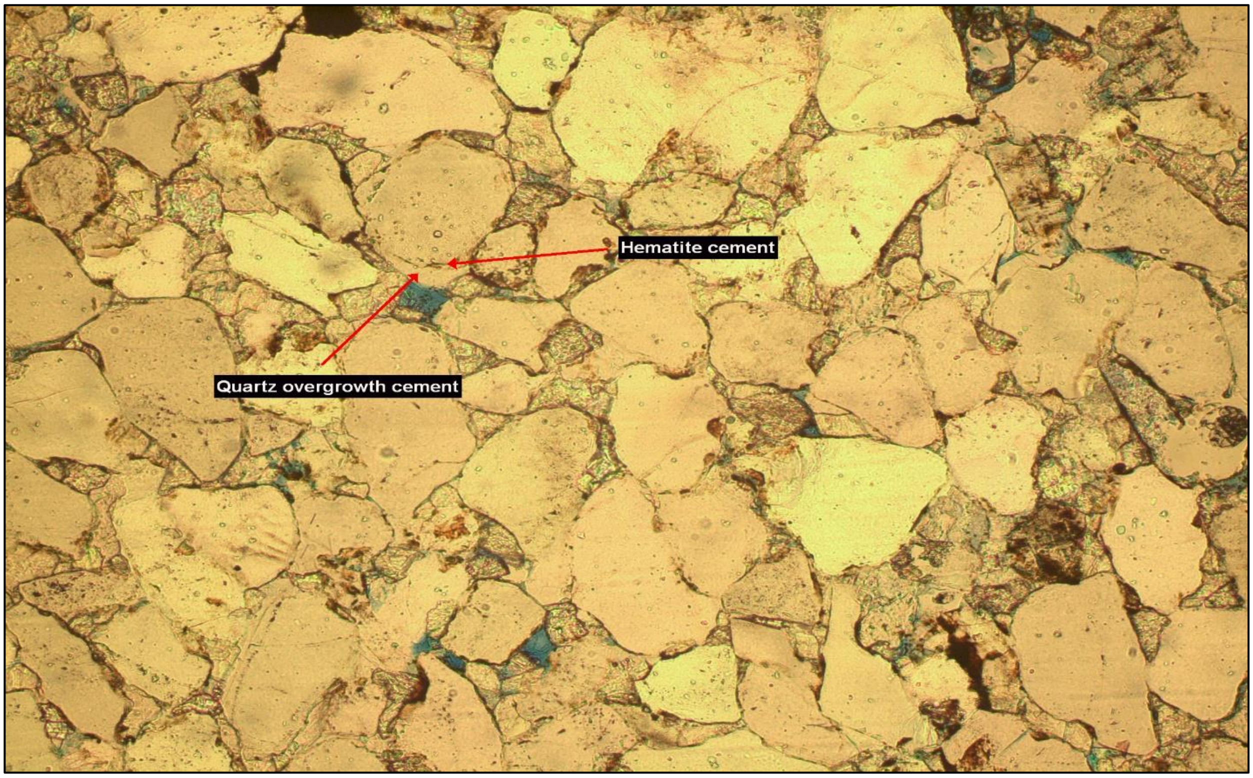

Figure 3-26. Sample ING-1. Sample in plane-polarized light showing hematite cement and quartz overgrowth cement.

The porosity is both intergranular and intragranular. The intergranular porosity makes up about 95% of the total porosity. The intragranular porosity is associated with the partially dissolved feldspar grains. In addition, there is some material in intergranular pore spaces that might be bitumen (Fig. 3.27).

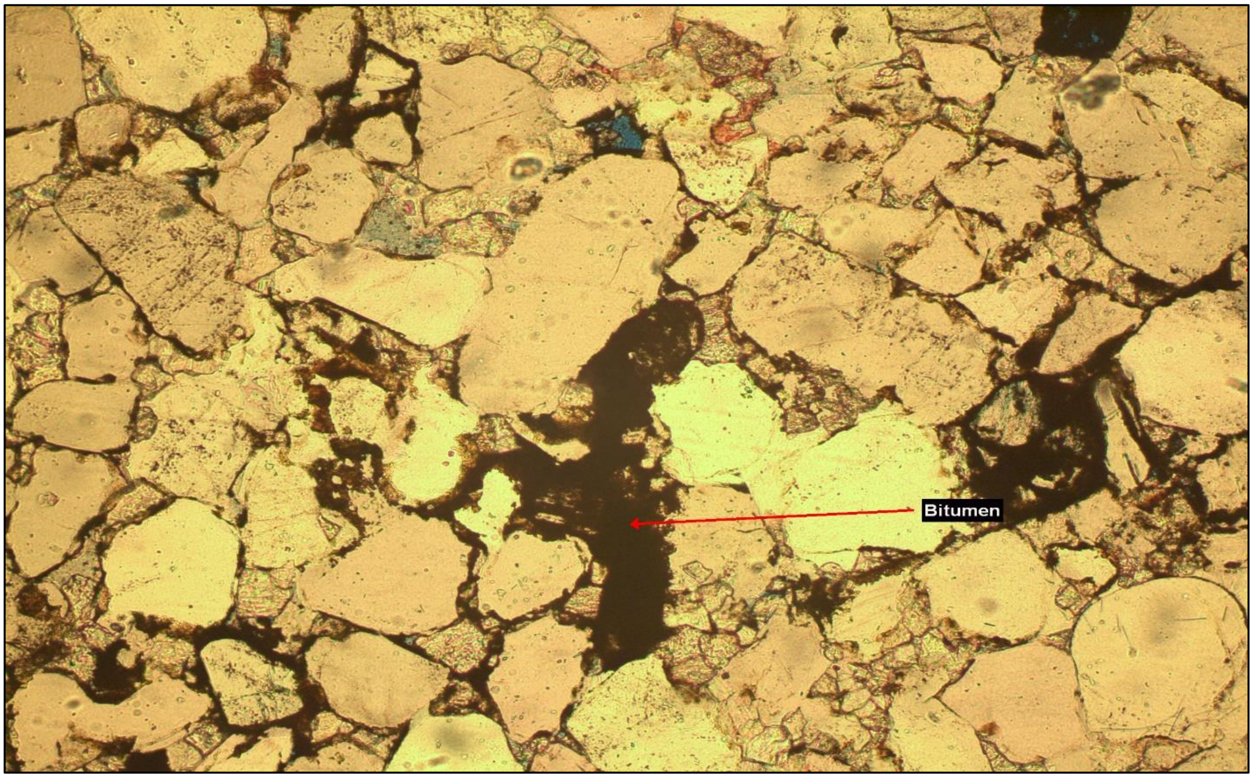

Figure 3-27. Sample ING-1. Sample in plane-polarized light showing possible remnant of bitumen.

ING- 2 (Bed 14):

The sample consists of moderately sorted very fine, fine, and medium sand grains. These grains are composed of quartz, K-feldspar, minor chert grains, opaque minerals, minor zircon, and glauconite. Most of the grains are sub-rounded, with some rounded, and have variable sphericity. The boundaries of the grains show concavo-convex, long, and point contacts. Long contacts are the most common type.

The sample is cemented most commonly with calcite, but also dolomite, silica, kaolinite, and hematite. The calcite and dolomite cements are patchy in some areas of the sample. Porosity is approximately 17% of the sample (Fig. 3.28). Intergranular porosity is common, with minor intragranular porosity. The sample is texturally mature, based on the moderate sorting and the lack of clay.

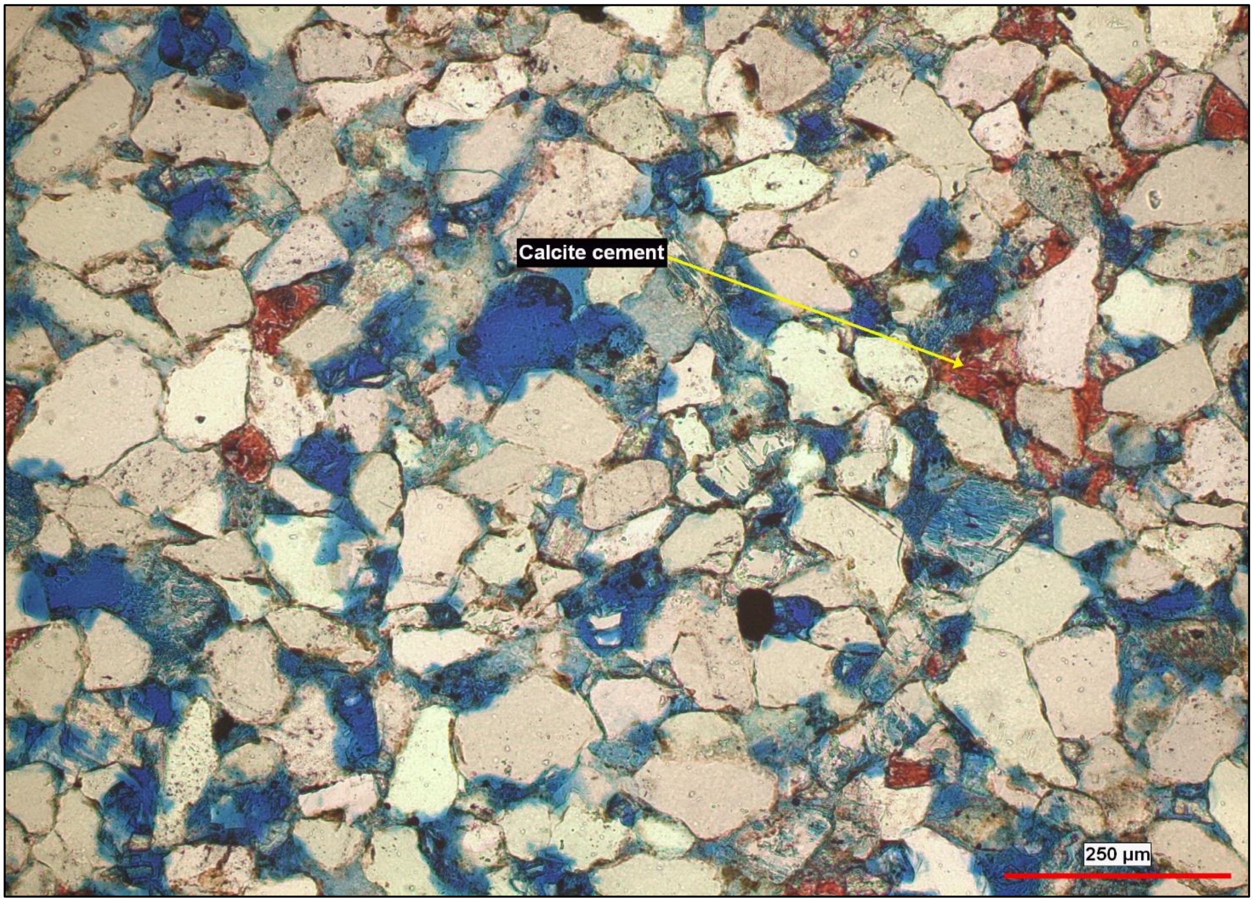

Figure 3-28. Sample ING-2. Intergranular and intragranular porosity (blue color). Photo is in plane-polarized light.

ING-5 (Bed 13):

The sample is composed mainly of moderately sorted very fine and fine sand grains consisting of quartz and minor K-feldspar, chert, opaques, and zircon. The grains are sub-rounded and rounded, but most of them are rounded with low sphericity to high sphericity. The grains have concavo-convex, point, and long contacts, with long contacts being the most common type. The sample contains laminations that are defined by bands of very fine sand grains (Fig. 3.29) and bands of calcite cement.

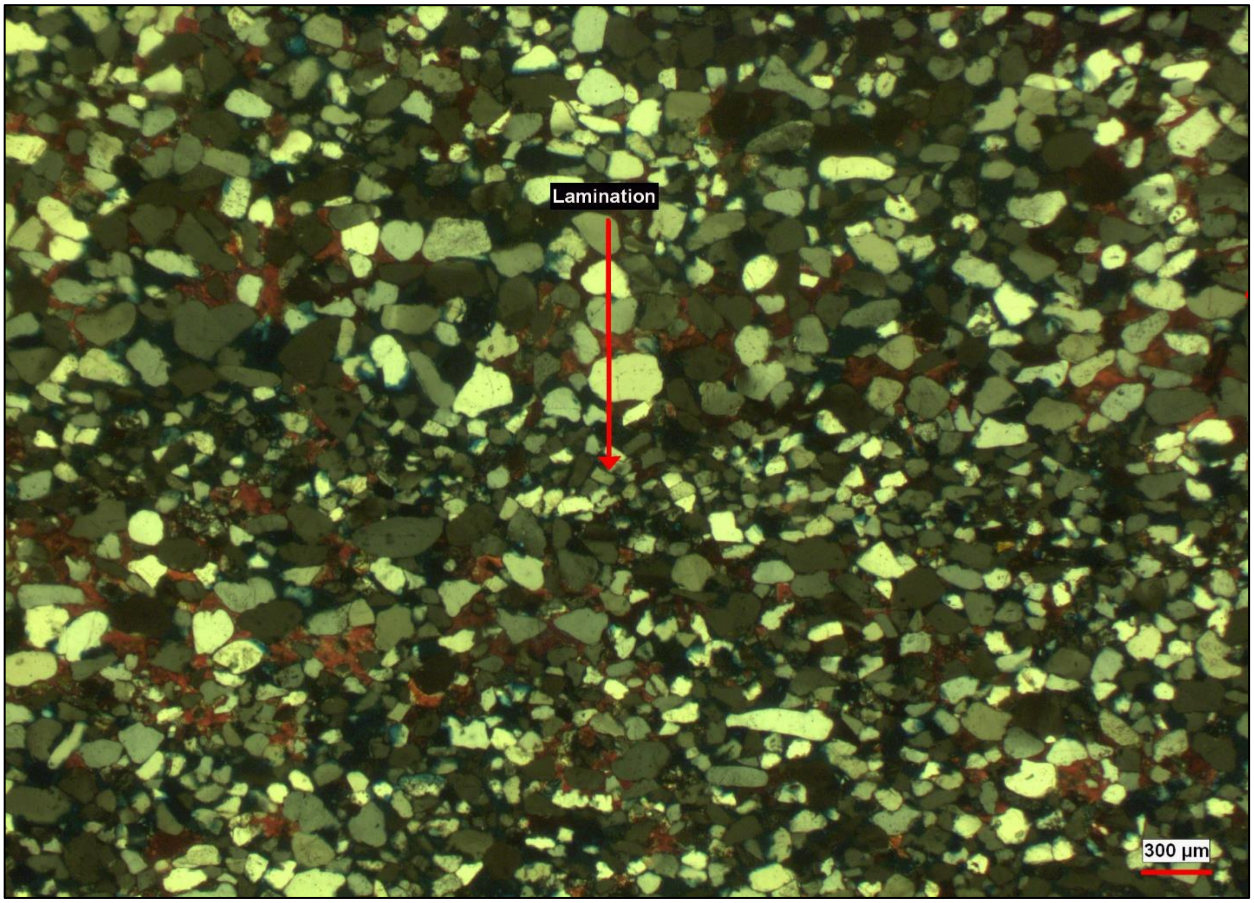

Figure 3-29. Sample ING-5. Lamination (horizontal in field of view) defined by very fine sand grains in cross polarized light. Note that there are multiple laminations in the picture.

The grains are well cemented with calcite (Fig. 3.30). Dolomite, hematite, kaolinite, and silica cements also occur. Intergranular porosity is common in the sample with minor intragranular porosity associated with partially dissolved feldspar grains.

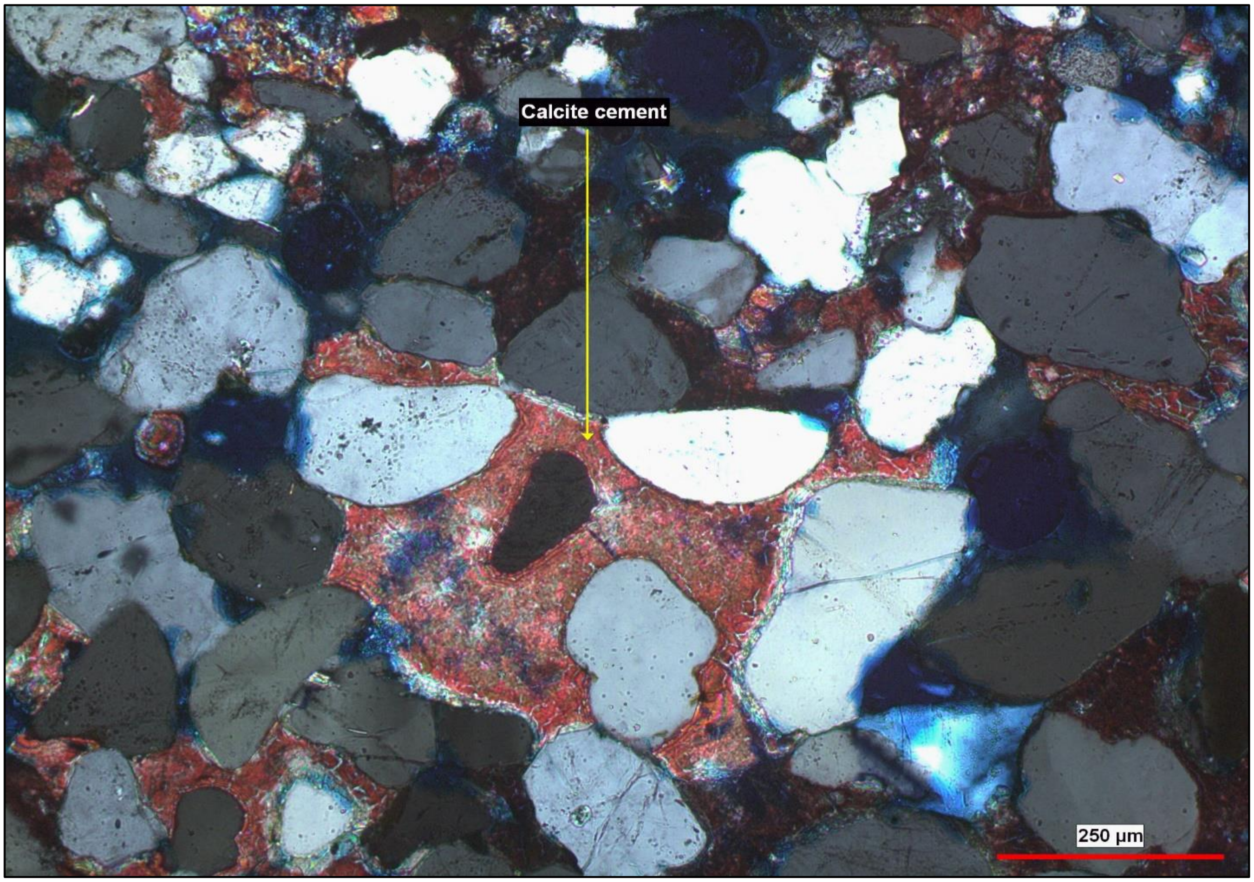

Figure 3-30. Sample ING-5. Calcite cement (stained red). Photo is in cross polarized light.

ING- 6 (Bed 13):

The sample is composed of poorly sorted fine, medium, and coarse sand grains consisting of quartz and minor K-feldspar, albite, minor zircon, and glauconite. Furthermore, there are some carbonate (Fig. 3.31) and sandy siltstone rock fragments. Some of the feldspar grains are partially dissolved, creating secondary porosity.

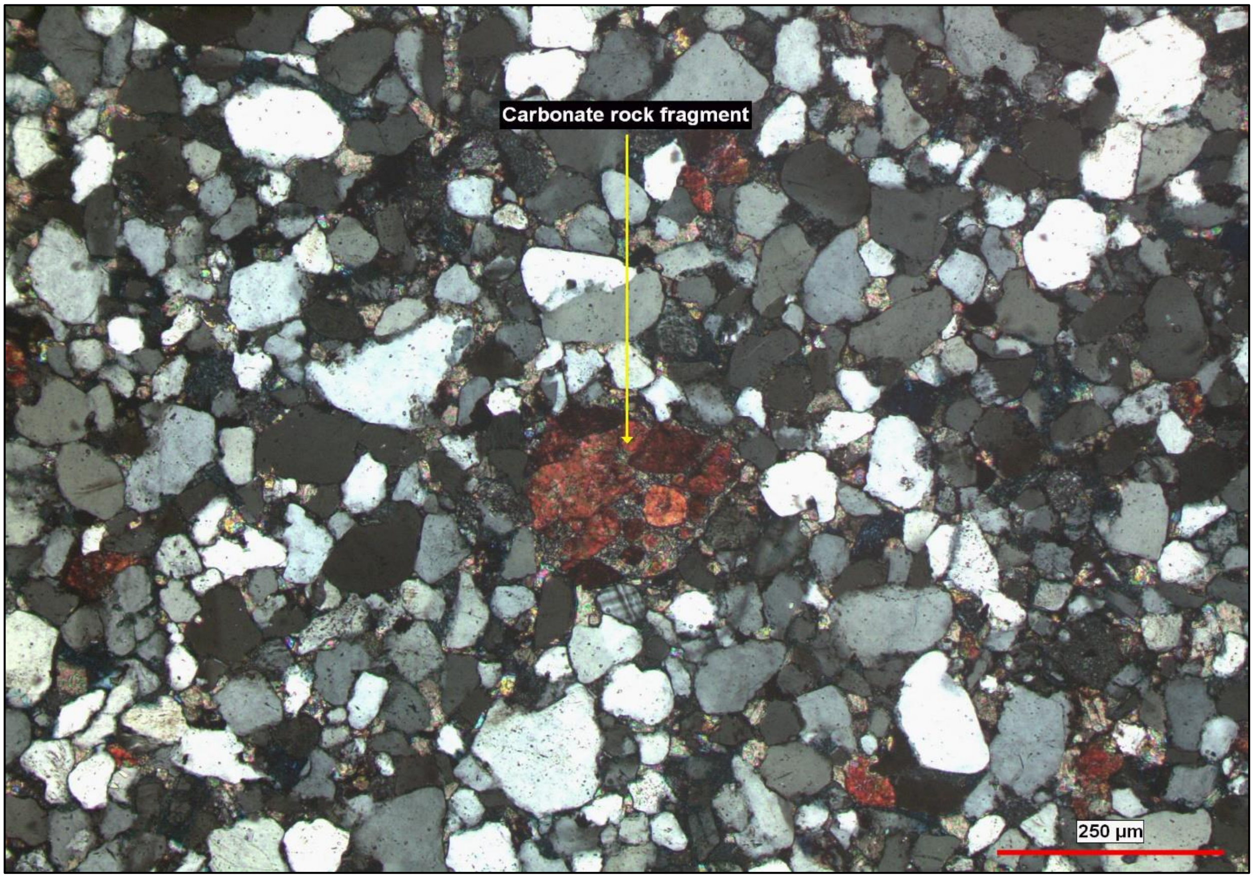

Figure 3-31. Sample ING-6. Carbonate rock fragment (calcite and dolomite). Photo is in cross polarized light.

One large, twinned microcline grain has a fracture that contains calcite and dolomite precipitated in it. (Fig. 3.32). Some of the feldspar is altered to calcite, dolomite, and kaolinite (Fig. 3.33). The sphericity of the grains is mainly low, but some have high sphericity and the roundness is variable. The contacts of the grains are point, concavo-convex, and, most commonly, long.

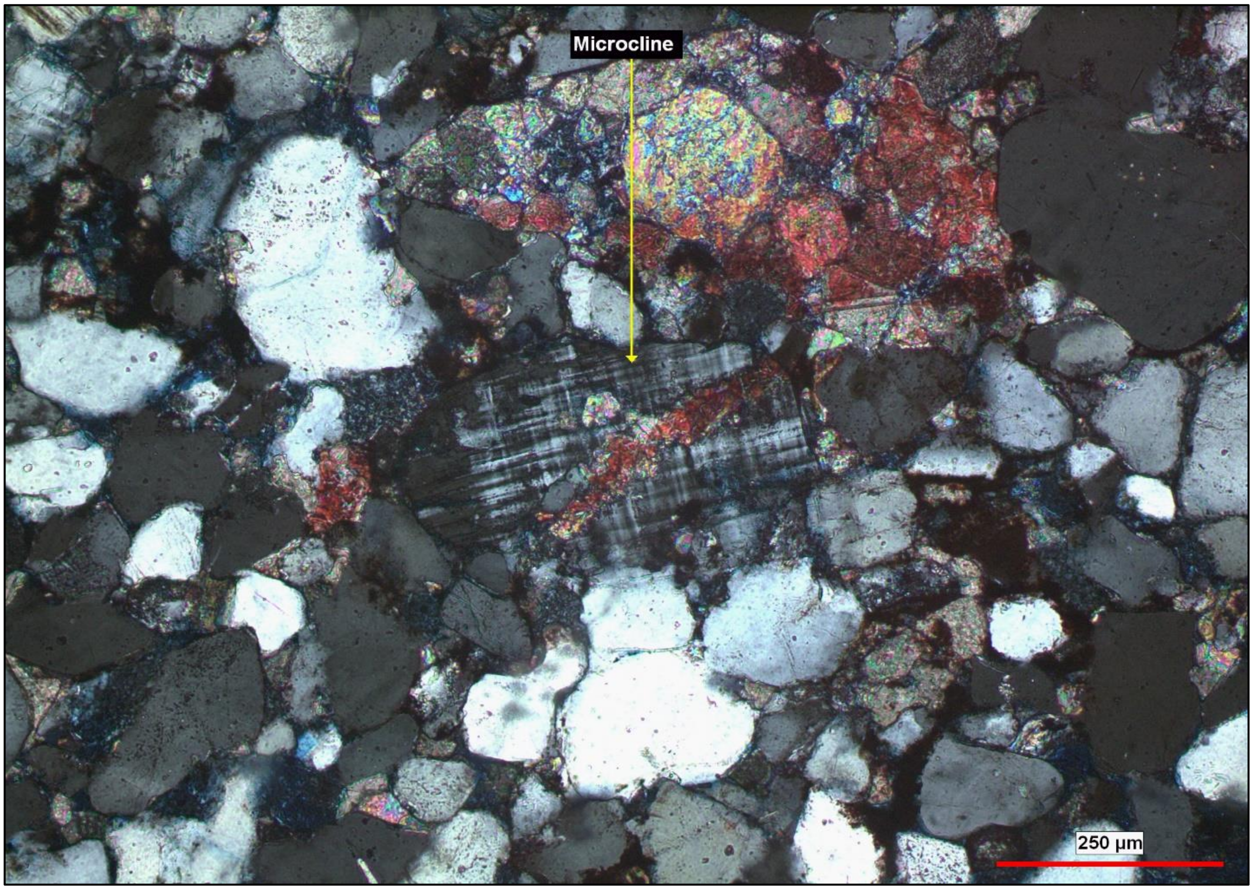

Figure 3-32. Sample ING-6. Large microcline grain with a fracture filled with calcite (stained red) and dolomite. Photo is in cross polarized light.

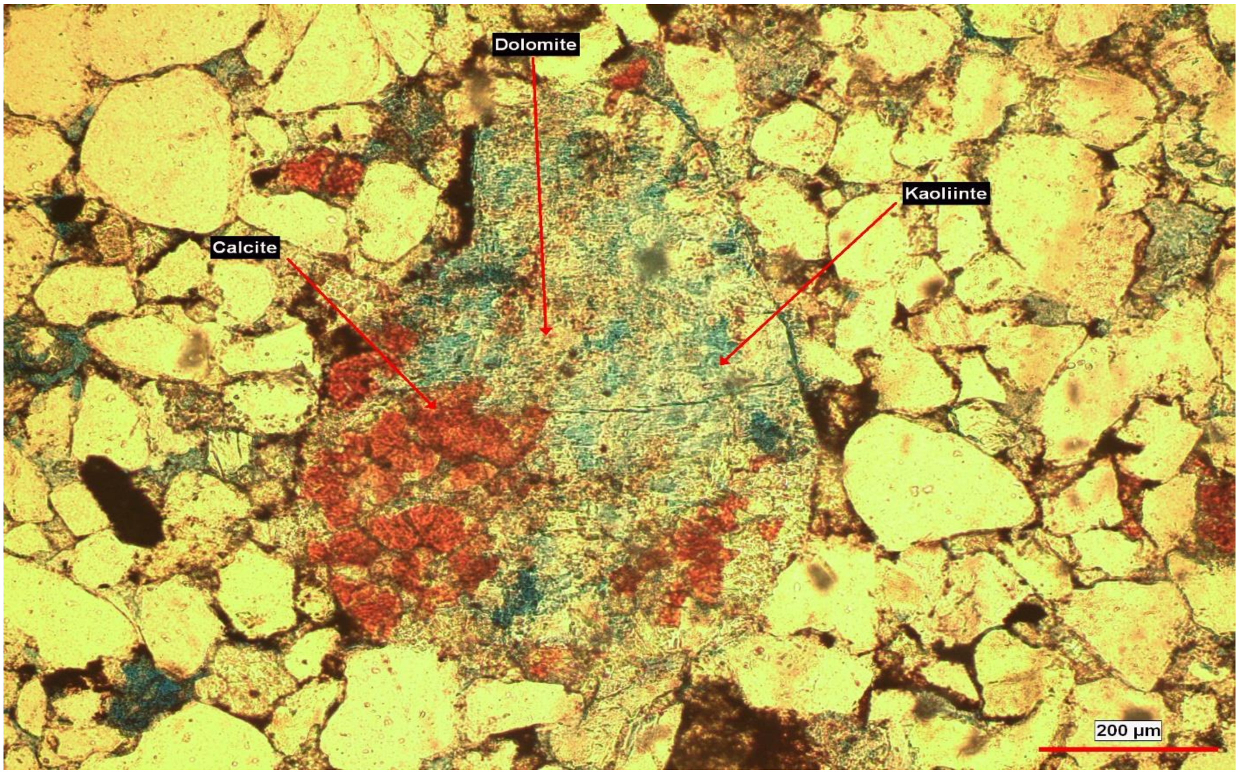

Figure 3-33. Sample ING-6. Feldspar grain is partially altered to dolomite, calcite (stained red), and kaolinite. Photo is in plane-polarized light.

The grains are cemented mainly with dolomite, calcite, silica, hematite, and kaolinite. Kaolinite is more abundant in this sample than the other samples. Hematite cement is present between grains that were affected by compaction. The dolomite cement is patchy in some areas of the thin section. There is some dark material that may be bitumen in some areas and is associated with the fine sand grains (Fig. 3.34). Porosity is mainly intergranular, with lesser intragranular porosity in partially dissolved feldspar grains.

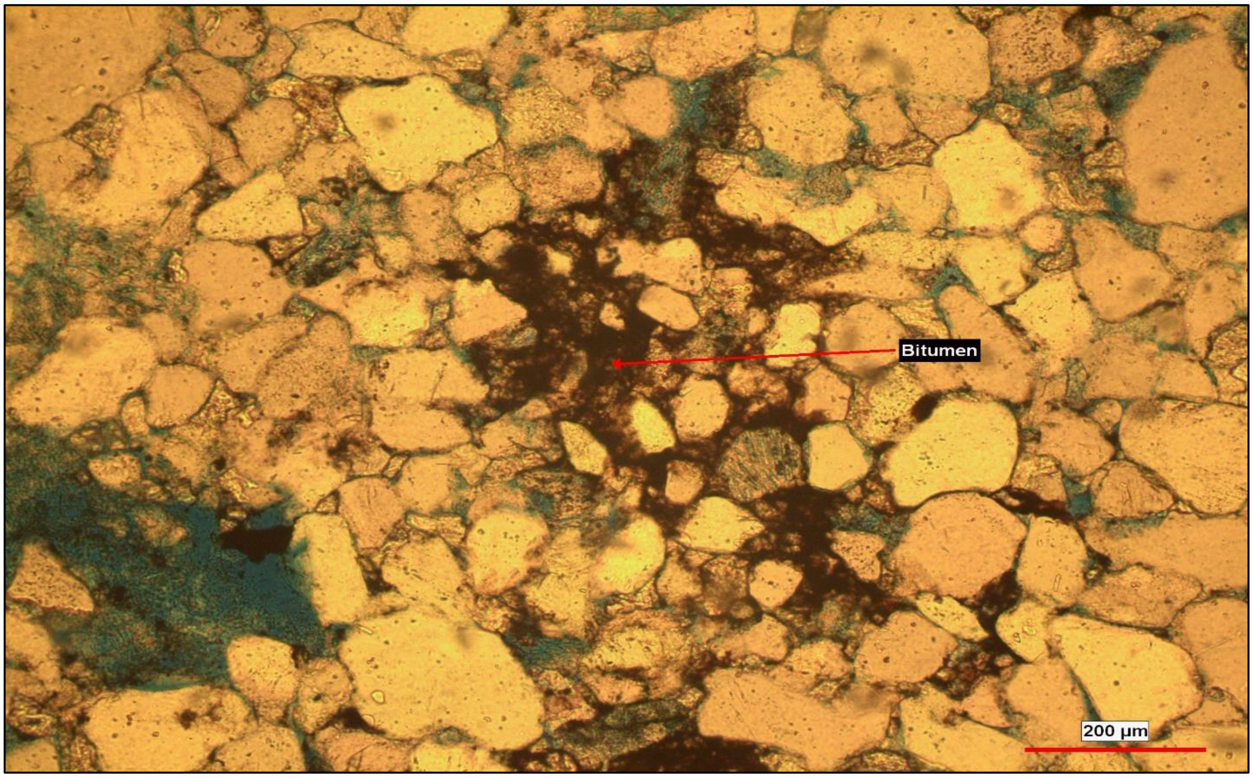

Figure 3-34. Sample ING-6. Bitumen distributed in some places. Photo is in plane-polarized light.

ING- 7 (Bed 12):

The sample consists mainly of dolomite with minor angular, very fine quartz sand grains. The dolomite crystal sizes and shapes are variable, but most are between 0.06 mm and 0.4 mm and have a subhedral shape (Fig. 3.35). The sample contains some calcite veins and stylolites hosting dark material (Fig. 3.36). The veins cut across each other in some places. Porosity is very rare and is intragranular or associated with veins.

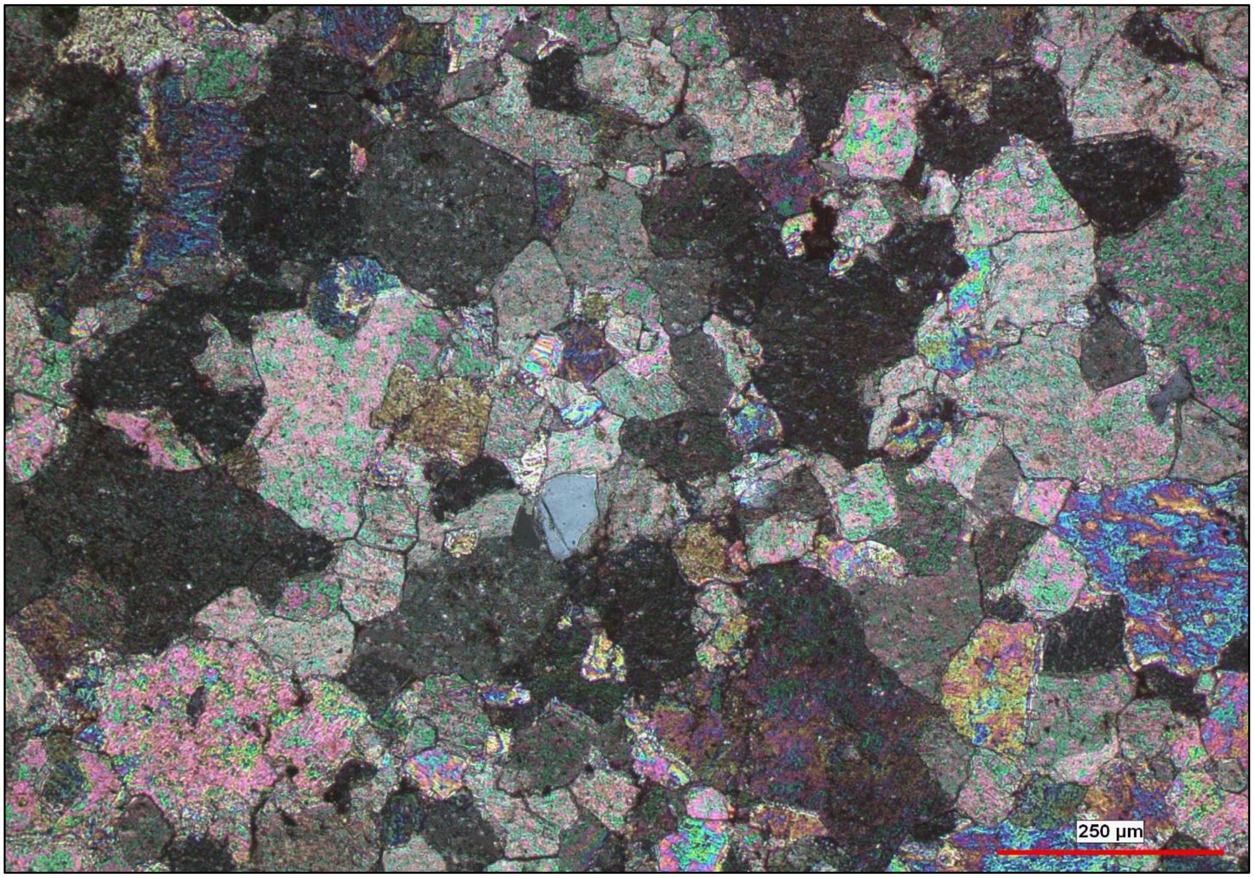

Figure 3-35. Sample ING-7. Dolomite in cross polarized light.

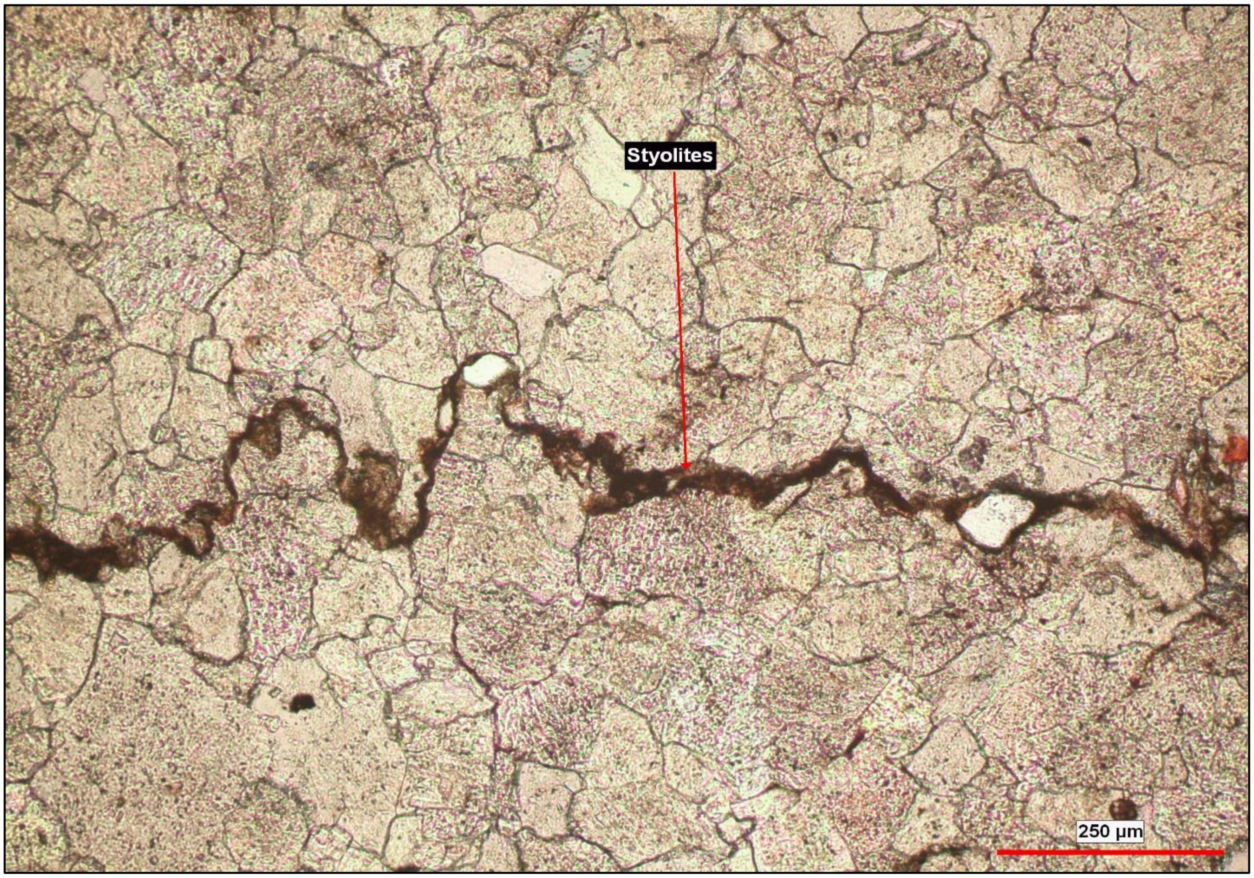

Figure 3-36. Sample ING-7. Stylolite in carbonate (dolomite) in plane-polarized light.

ING- 8 (Bed 12):

The sample is composed primarily of dolomite and calcite with some very fine sand grains. The sand grains are well-sorted, with diameters of about 0.08 mm, and are composed of quartz and minor K-feldspar. The dolomite crystals are up to 0.36 mm across and euhedral or subhedral in shape, whereas calcite crystals are anhedral. The sand grains are mostly concentrated in one part of the thin section (Fig. 3.37). The angular sand grains mainly have high sphericity. The sample contains some dark material that may be bitumen residue. In addition, intergranular porosity is common in the sample.

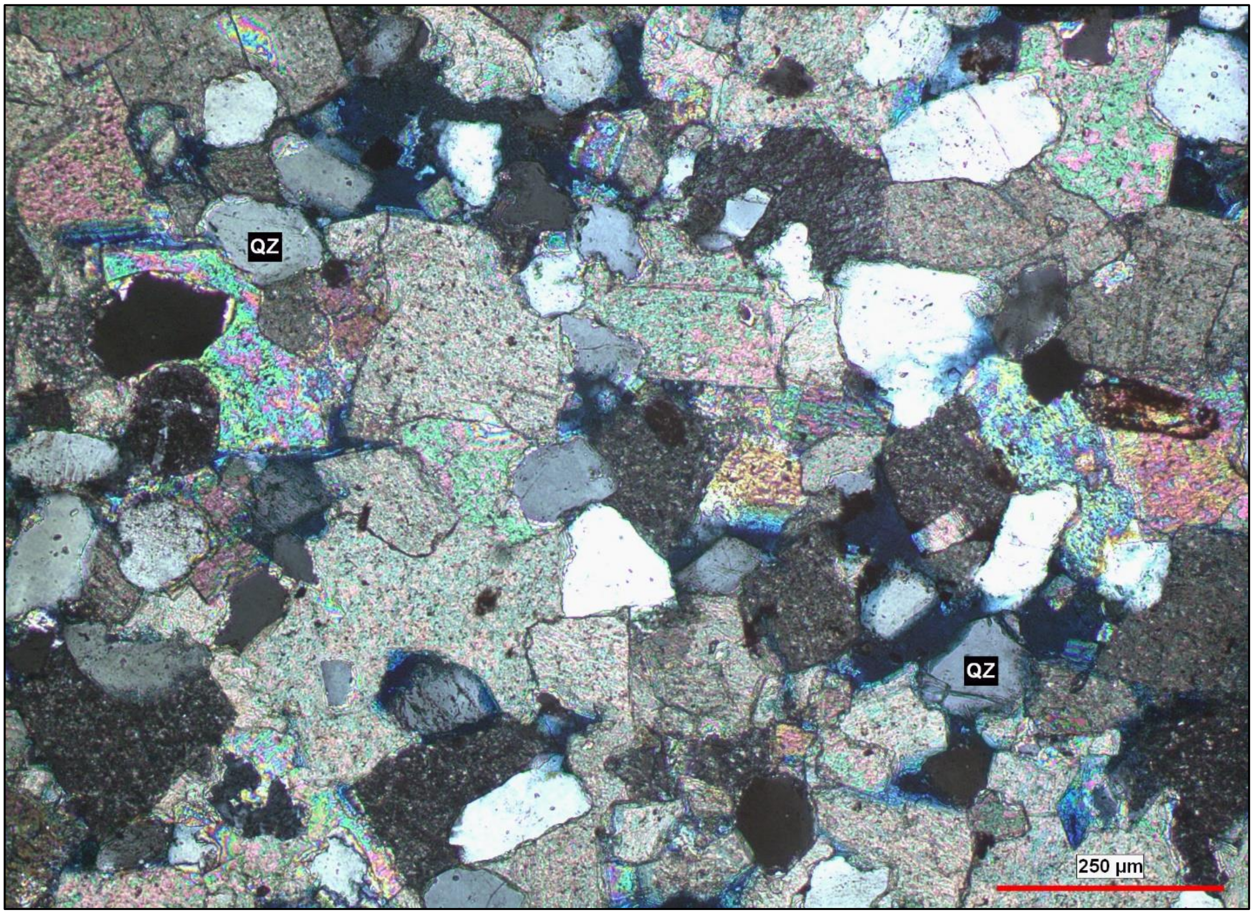

Figure 3-37. Sample ING-8. Quartz (QZ) grains associated with carbonate. Photo is in cross polarized light.

ING-9 (Bed 11):

The sample is composed of poorly sorted, very fine and fine sand grains composed of quartz, K-feldspar, albite, and minor glauconite, biotite, zircon, and opaques. Most of the grains have concavo-convex contacts and some have long and point contacts. The roundness of the grains is variable, but most are sub-rounded with low sphericity. The sample is well-cemented, dominantly with dolomite and patchy calcite, but also silica, kaolinite, and hematite. The cements are much more abundant than the porosity, especially the dolomite cement.

Moreover, the sample contains some fractures hosting secondary porosity, calcite, and possible residual of bitumen. The bitumen is also found in scattered pore spaces, and associated with the calcite and dolomite cement (Fig. 3.38). Most of the porosity is intergranular, with intragranular porosity associated with the partially dissolved feldspar grains. Overall, the sample is texturally sub-mature, based on the sorting, roundness, and lack of clay.

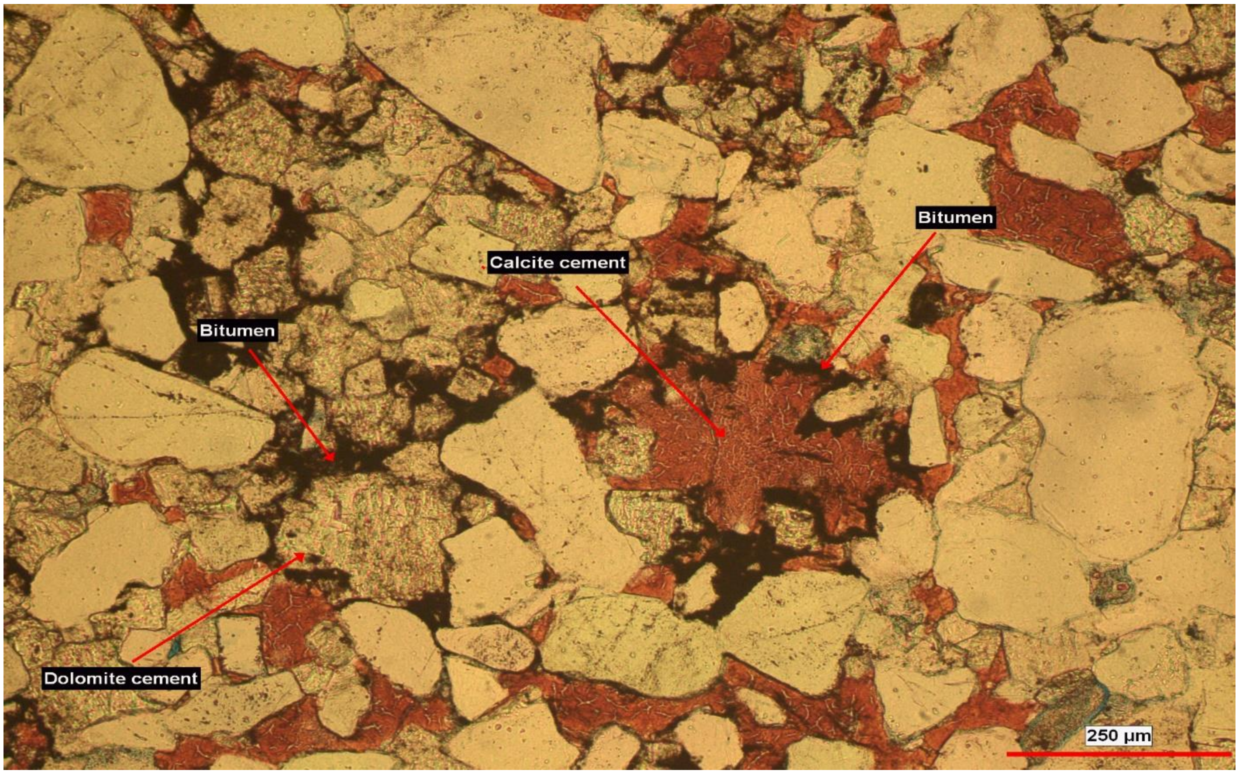

Figure 3-38. Sample ING-9. Bitumen found between grains and calcite and dolomite cement. Photo is in plane-polarized light.

ING-10 (Bed 11):

The sample is made up of well-sorted fine sand grains that are composed of quartz, K-feldspar, albite, sideritic mud clasts, and minor biotite, muscovite (Fig. 3.39), opaques, chlorite, and glauconite. Most of the sand grains are sub-angular, with some rounded; sphericity is high. Grain contacts are point, long, and concavo-convex. The grains are well cemented with calcite, dolomite composed of large crystals (Fig. 3.40), and minor silica. The sample contains calcite filled veins cuts across the sample (Fig. 3.41)

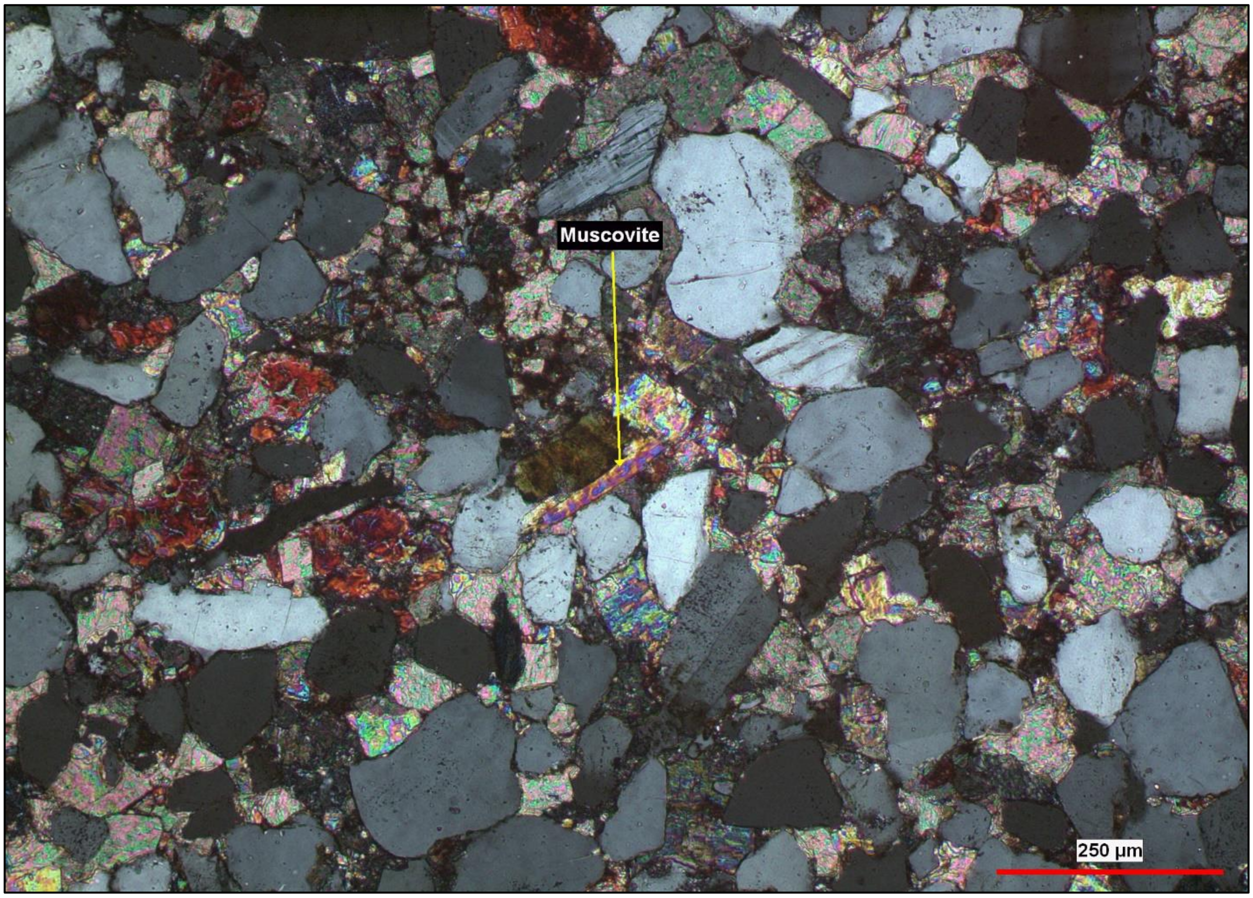

Figure 3-39. Sample ING-10. Muscovite surrounded by quartz grains in cross polarized light.

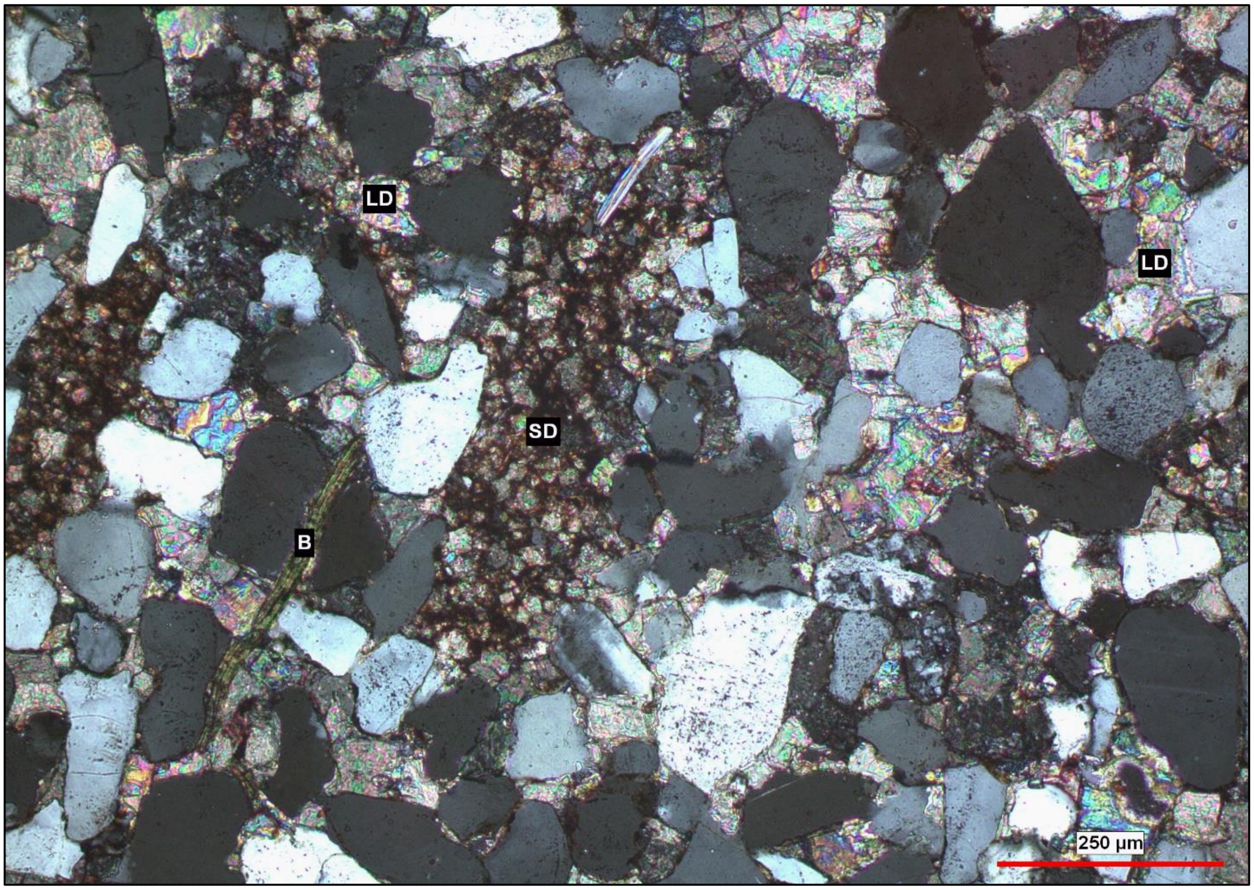

Figure 3-40. Sample ING-10. Small or fine siderite (SD) crystals in a clast, large dolomite (LD) crystals and biotite(B) surrounded by quartz grains. Photo is in cross polarized light.

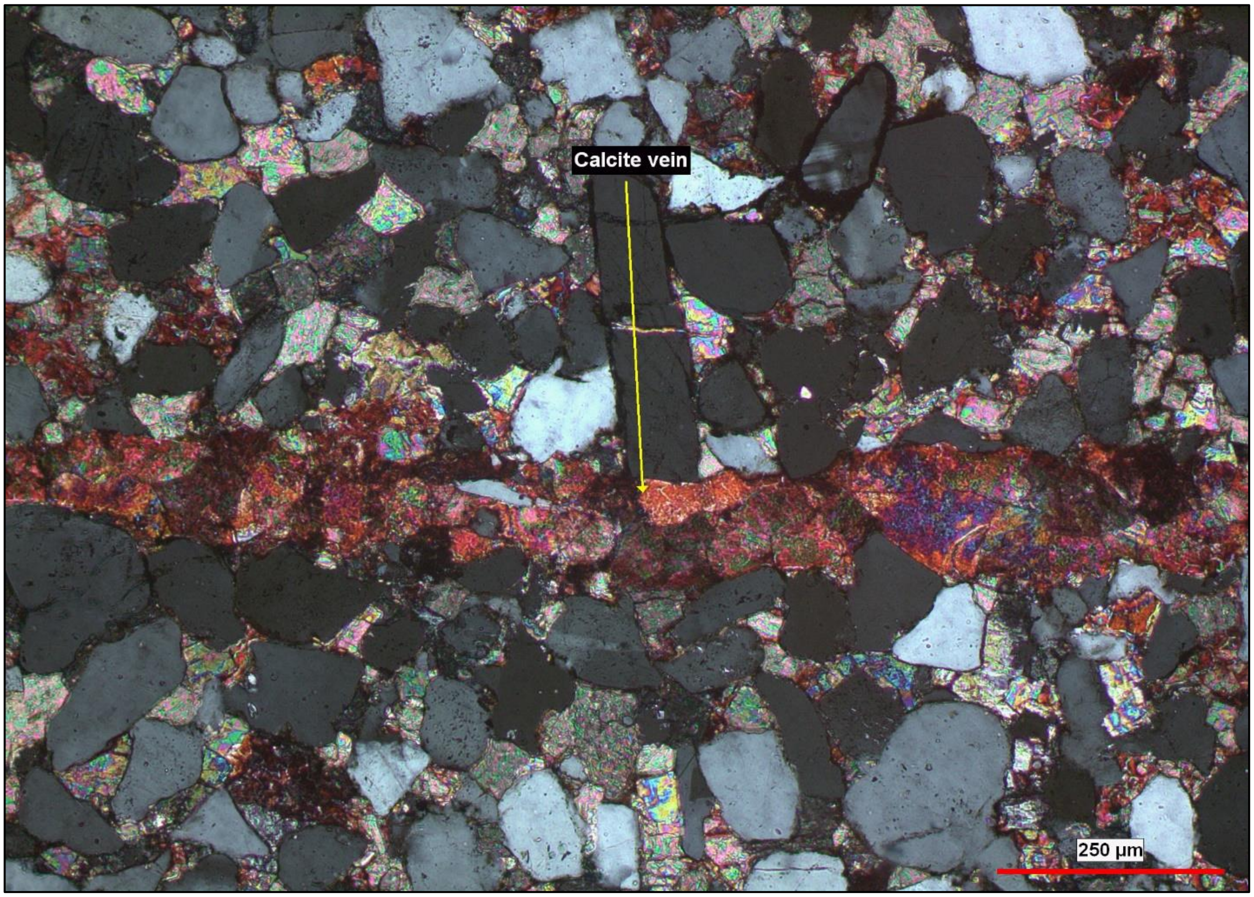

Figure 3-41. Sample ING-10. Vein filled with calcite in cross polarized light.

ING-11 (Bed 10):

The sample comprises well-sorted very fine and fine sand grains, but mostly fine grains. The sand grains are composed of quartz and minor K-feldspar, albite, glauconite, chert grains, and opaques. Most of the grains are rounded or well-rounded with high sphericity. In addition, most of the grains have point contacts, with some concavo-convex contacts.

The grains are dominantly cemented with dolomite, which has partially replaced some quartz grains (Fig. 3.42), and with lesser patchy calcite, minor silica, kaolinite, and hematite. There are two types of dolomite, one with quite large crystals and the other with small crystals. However, the large crystals are the dominant type. There is dark material on some grain boundaries that is more prominent than in some samples and may be bitumen residue. Porosity is rare, and is intergranular and fracture. Overall, the sample is texturally mature, based on the sorting, rounding, and lack of clay.

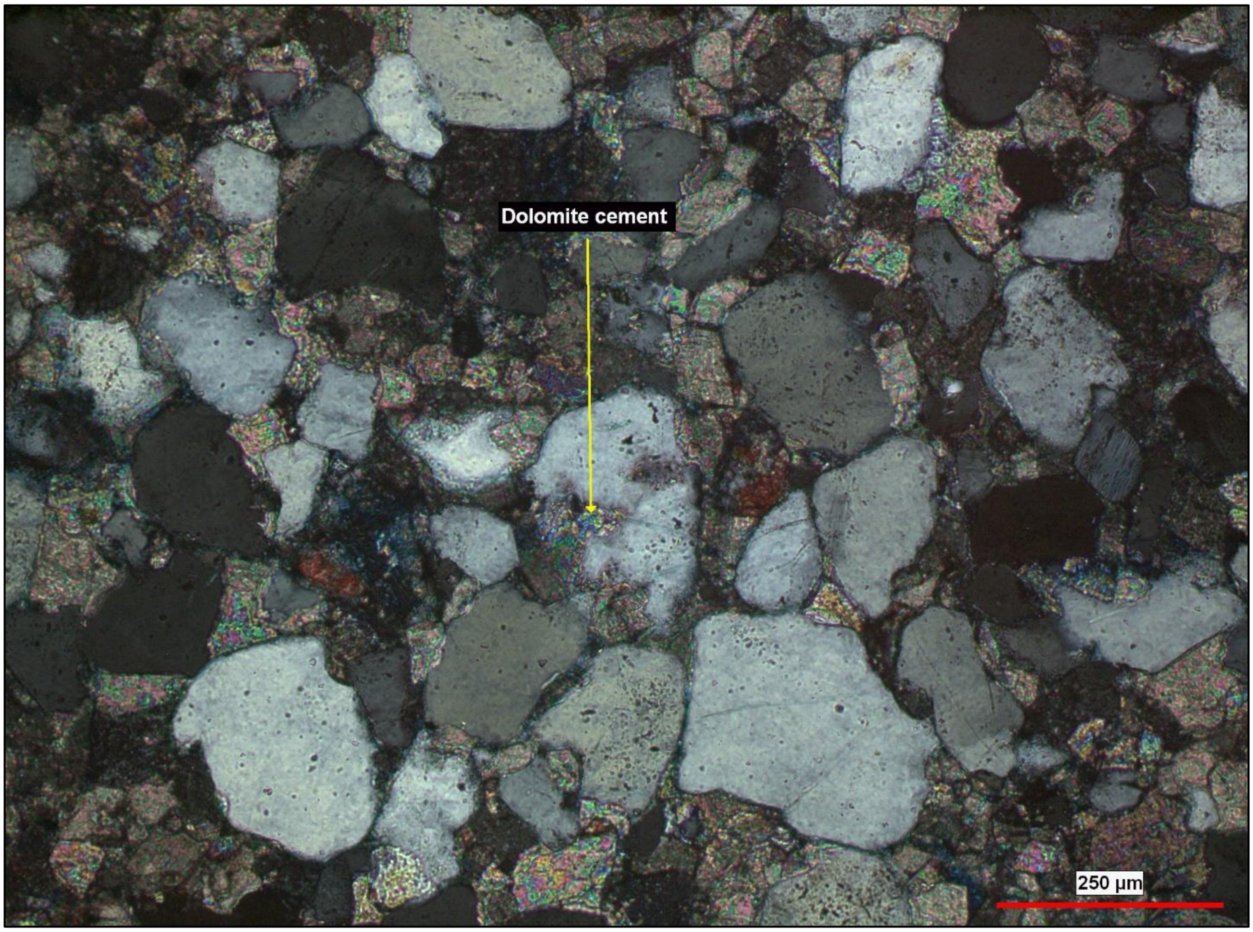

Figure 3-42. Sample ING-11. Dolomite cement partially replacing quartz grain. Photo is in cross polarized light.

ING- 12 (Bed 10):

The sample has moderately sorted very fine, fine, and medium sand grains. Fine grains dominate. Most of the sand grains are rounded and well-rounded with high sphericity. Both point contacts and concavo-convex contacts occur. The grains are composed of quartz and minor K-feldspar, albite, and opaques. There are laminations in the sample defined by concentrations of very fine sand grains. Cements include dolomite, calcite, kaolinite, and hematite. Dolomite, the dominant cement, has large crystals throughout the sample and calcite cement is patchy. The sample contains small traces of dark material that may be bitumen residue. Porosity is both intergranular and intragranular.

ING- 14 (Bed 10):

The sample is made up of moderately sorted very fine, fine, and medium sand grains, but mostly fine grains. The sand grains are composed of quartz, carbonate clasts that have variable shapes, and minor K-feldspar, albite, zircon, opaques, (Fig. 3.43). The roundness of the grains is variable, but most of them are angular with low sphericity, and some have high sphericity.

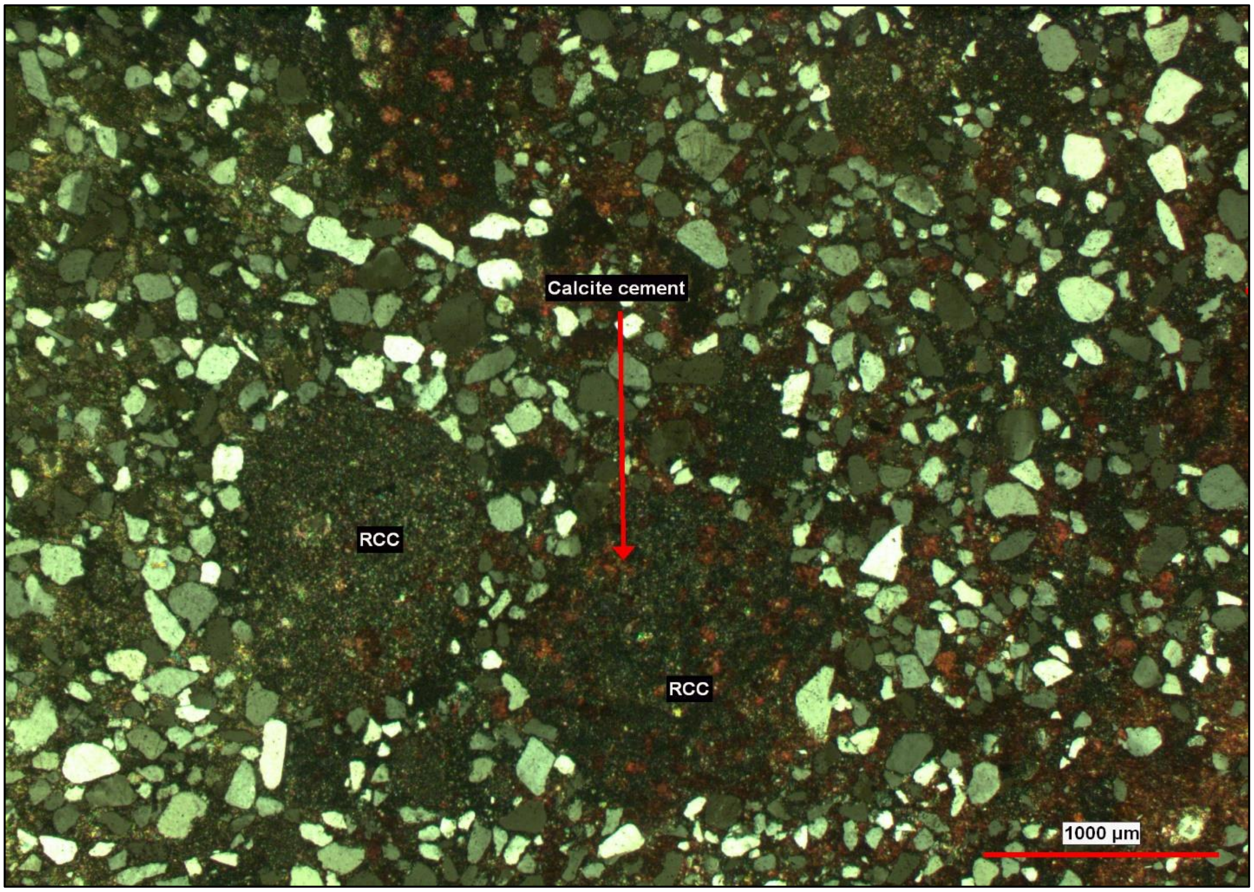

Figure 3-43. Sample ING-14. Rounded carbonate clasts (RCC). Note calcite cement (stained red) inside some of the carbonate clasts. Photo is in cross polarized light.

Calcite cement is distributed throughout the sample, and fills veins and replaces some of the carbonate mud. Dolomite cement occurs as small crystals in some places and with silica cement. Most of the grains do not contact each other within the plane of the thin section. However, some grains show point contacts. Porosity is rare intergranular and intragranular. Due to the angular grains and poor sorting, the sample is texturally immature.

ING-15 (Bed 9):

The sample is composed of variably sized dolomite and calcite crystals. The dolomite is mostly large crystals of saddle (baroque) dolomite. Most of the dolomite crystals are euhedral in shape and some of them show zoning, with slightly darker color that might be due to imperfection in the center surrounded by cleaner-appearing dolomite and then a very thin calcite zone and to the outside of that a very thin dolomite zone (Fig. 3.44). The saddle dolomite crystals were observed only in this carbonate bed, and were not observed in sandstone samples. The calcite occurs as small crystals that surround the large dolomite crystals. The few sand grains present are quartz. The sample contains some dark material that may be residue after bitumen that moved through the calcite. There is intragranular, intergranular, and fracture porosity.

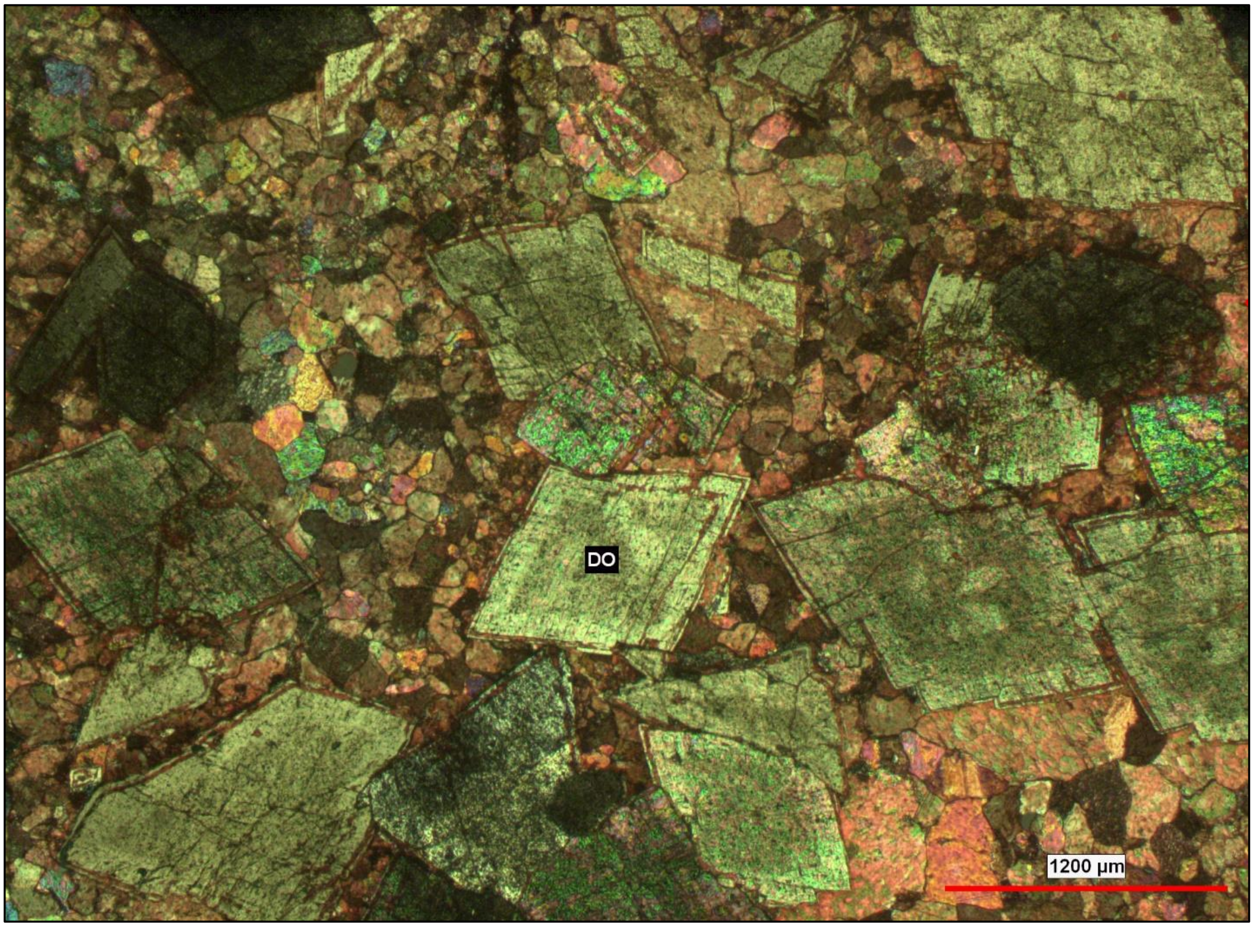

Figure 3-44. Sample ING-15. (DO) Saddle or baroque dolomite and small calcite crystals. Note the zoning in dolomite crystals. Photo is in cross polarized light.

ING- 16 (Bed 9):

The sample consists mostly of dolomite with some calcite and some quartz grains. The very fine to fine quartz grains are distributed evenly throughout the sample and surrounded by carbonate. The calcite crystals are smaller than the dolomite crystals, and anhedral in shape, whereas the dolomite crystals are mainly subhedral. The sand grains are angular to sub-rounded and have low sphericity. The scarce porosity is mainly intergranular.

ING- 17 (Bed 9):

The sample is composed mainly of dolomite, with minor calcite. A calcite filled fracture cuts across the sample (Fig. 3.45). The calcite also is scattered throughout the sample, commonly occurring around voids. There are some vugs or cavities, with some about 0.5 mm across. The sample contains a few fine fractures hosting porosity. Porosity here includes intergranular, fractures not filled with calcite, and that associated with cavities.

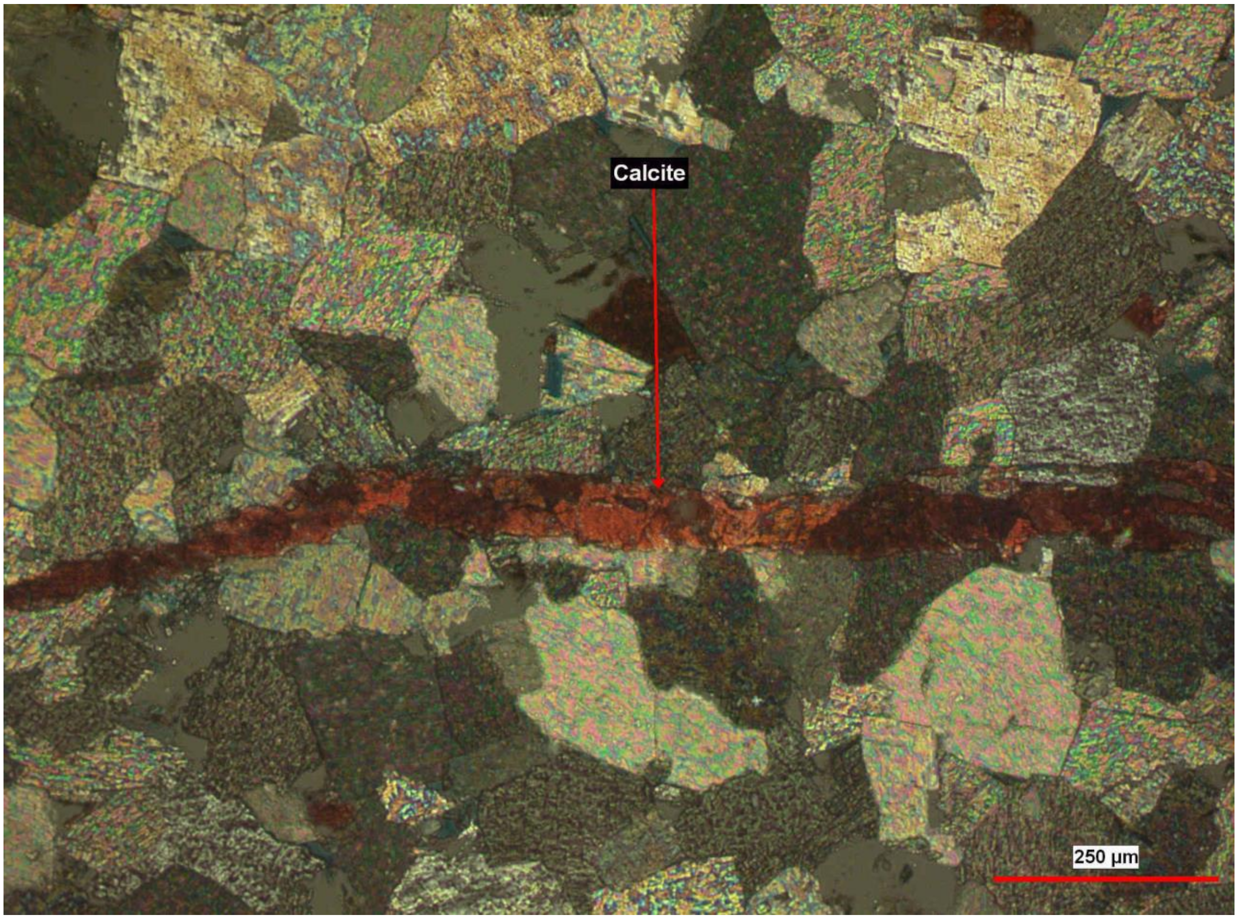

Figure 3-45. Sample ING-17. Calcite filling fracture through dolomite in cross polarized light.

ING- 18 (Bed 7):

The sample is composed mainly of dolomite, with lesser calcite. The dolomite crystals are fairly uniform in size and shape, and are mostly euhedral rhombic. The calcite occurs in patches and as fracture filling. There are a few vugs in the thin section. The sample contains small traces of dark material that may be a residue of bitumen. Porosity is both intergranular and in fractures.

ING-19 (Bed 7):

The sample consists mainly of subhedral to euhedral dolomite, with lesser calcite. Some very fine sand grains composed of quartz, are distributed evenly through the sample; these are angular and have low sphericity. The dolomite here is of two types, very small (mostly around 0.06 mm), anhedral crystals, and large (mainly about 0.16 mm), euhedral crystals. The small dolomite crystals in some areas are organized into faint laminations. The sample contains dark material, which may be a residue of bitumen and which is mostly associated with calcite. Porosity is almost absent in the sample.

ING- 20 (Bed 7):

The sample consists of very fine dolomite, with very fine sand grains scattered throughout. The sand grains consist of quartz and minor K-feldspar. These sand grains are angular to sub-angular with low sphericity and some of them are elongate. Porosity is uncommon in the sample and consists of intragranular and fracture porosity.

ING-21 (Bed 6):

The sample is made up of moderately sorted very fine, fine, and medium sand grains that are composed of quartz and minor K-feldspar, albite, and opaques. The sand grains are angular to sub-angular and have low sphericity. The grains have point and long contacts, with point contacts more common. The sample also contains some partially dissolved feldspar grains in some areas. The grains are cemented with dolomite which is the dominant cement, and poikilotopic in some areas (Fig. 3.46). The grains that are cemented with the poikilotopic cement are coated with hematite cement (Fig. 3.47). It is pervasive and has large crystals in most areas of the thin section. Patchy calcite cement is also present. The sample also is cemented with hematite, kaolinite, and silica overgrowths. There is a vein filled with calcite cutting across the sample.

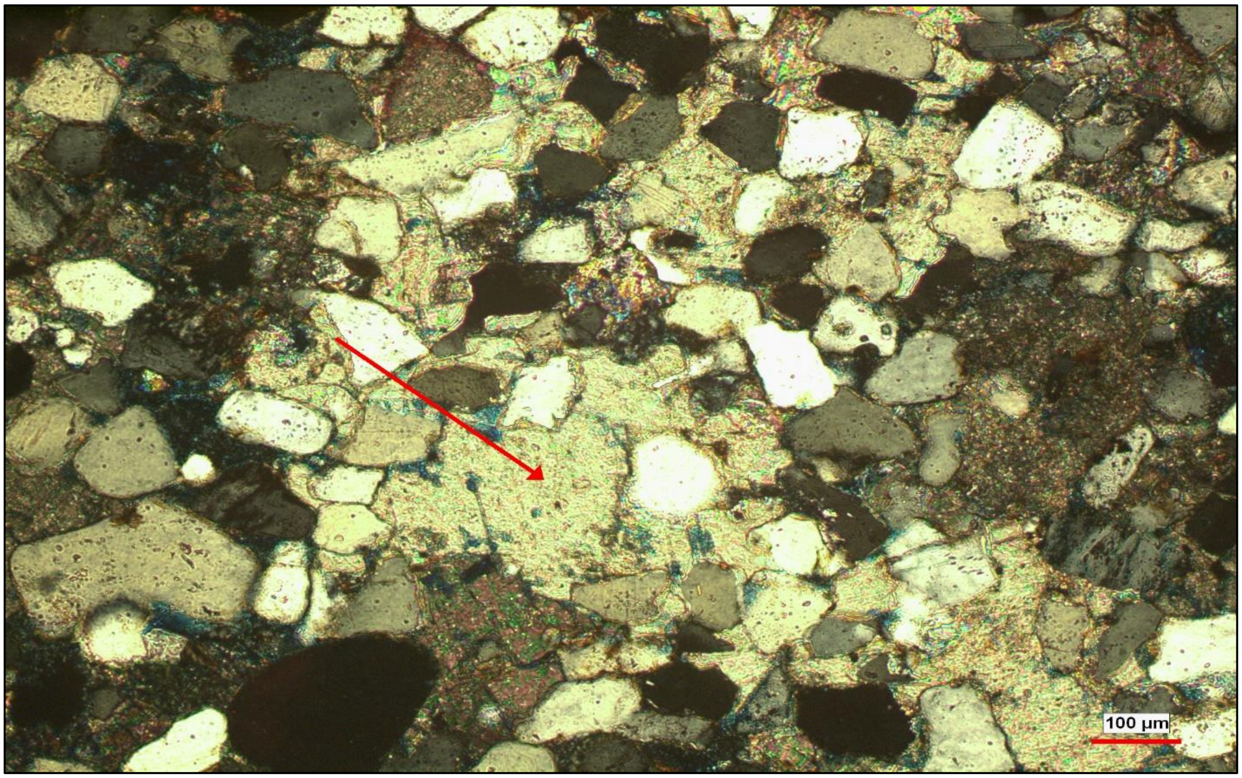

Figure 3-46. Sample ING-21. Poikilotopic dolomite cement (red arrow). Photo is in cross polarized light.

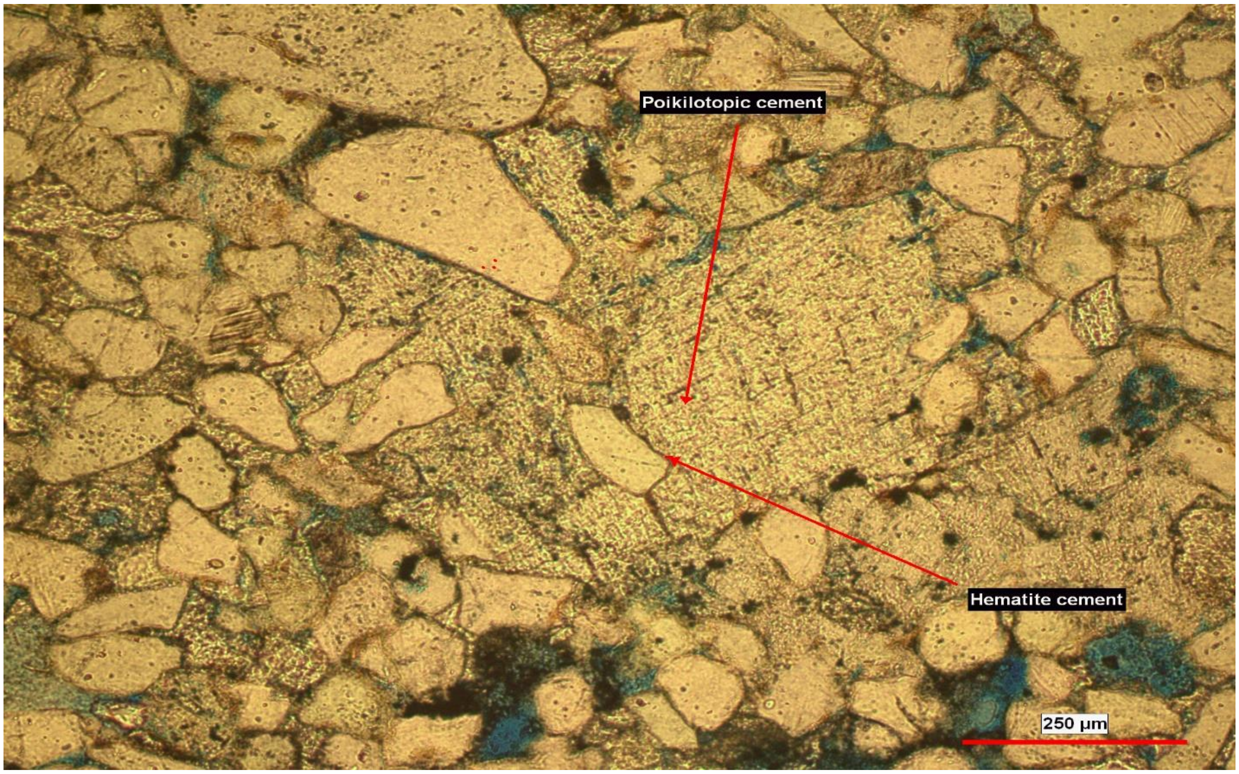

Figure 3-47. Sample ING-21. Poikilotopic dolomite cement. Note the grains are coated with hematite cement. Photo is in plane-polarized light.

The sample contains some dark material, especially along the fracture filled with calcite, which may be residue of bitumen (Fig. 3.48). Porosity occurs as fractures, intergranular porosity, and intragranular porosity. Additionally, the sample is texturally sub-mature based on the moderate sorting, angular grains, and lack of clay.

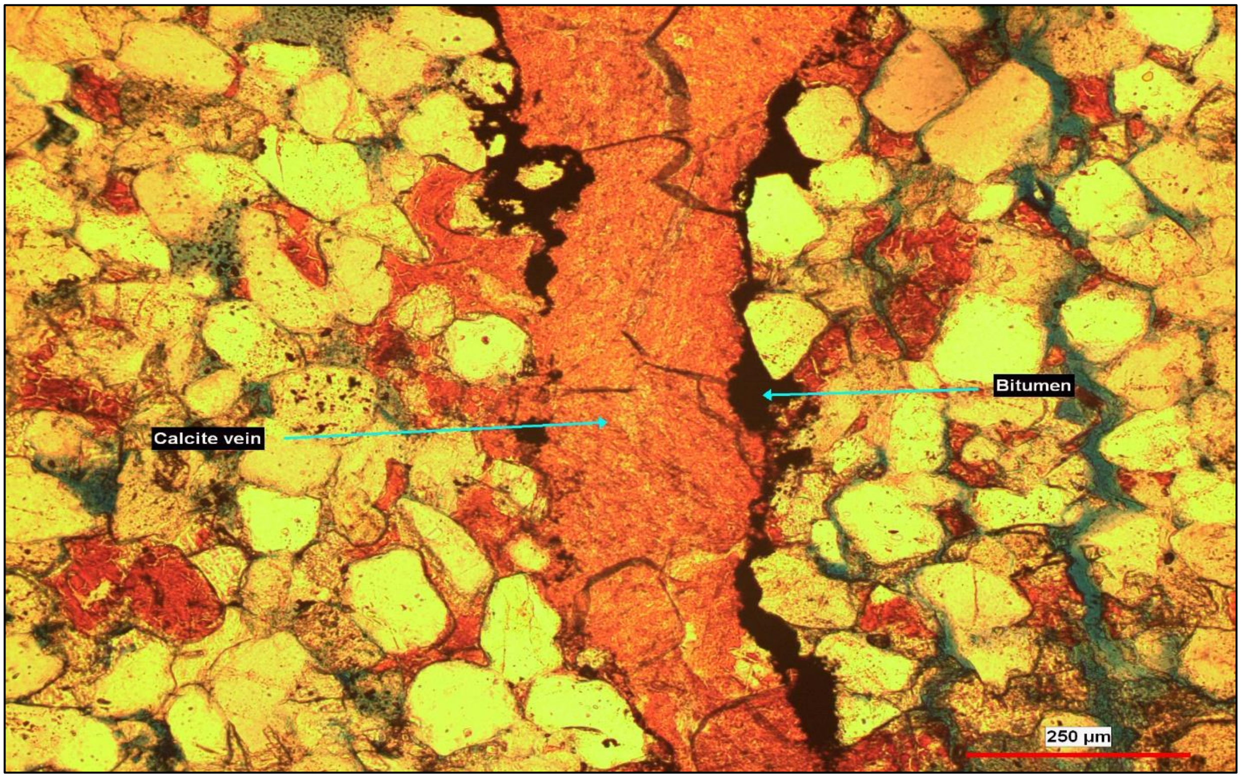

Figure 3-48. Sample ING-21. Possible residue of bitumen along fracture filled with calcite. Photo is in plane-polarized light.

ING- 22 (Bed 6):

The sample is composed of fine calcite and minor dolomite, with minor very fine scattered sand grains composed of quartz. There are a few fossil fragments (crinoid) present in the sample (Fig. 3.49). The sample contains some fractures filled with some possible residue of bitumen (Fig. 3.50, 3.51). There is porosity associated with the fractures.

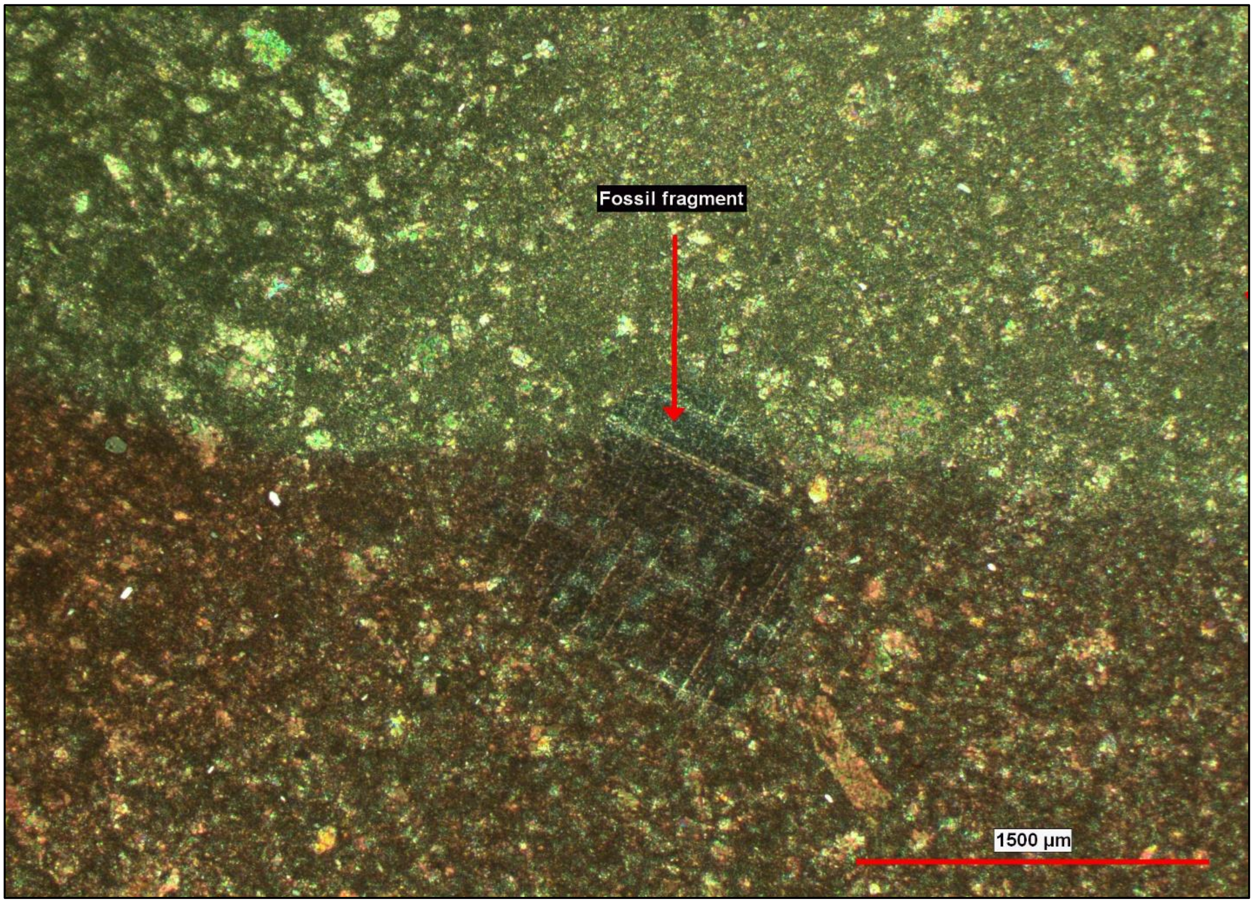

Figure 3-49. Sample ING-22. Fossil fragment (crinoid) that is surrounded by calcite (red). Photo is in cross polarized light. The upper half of the photo is unstained calcite.

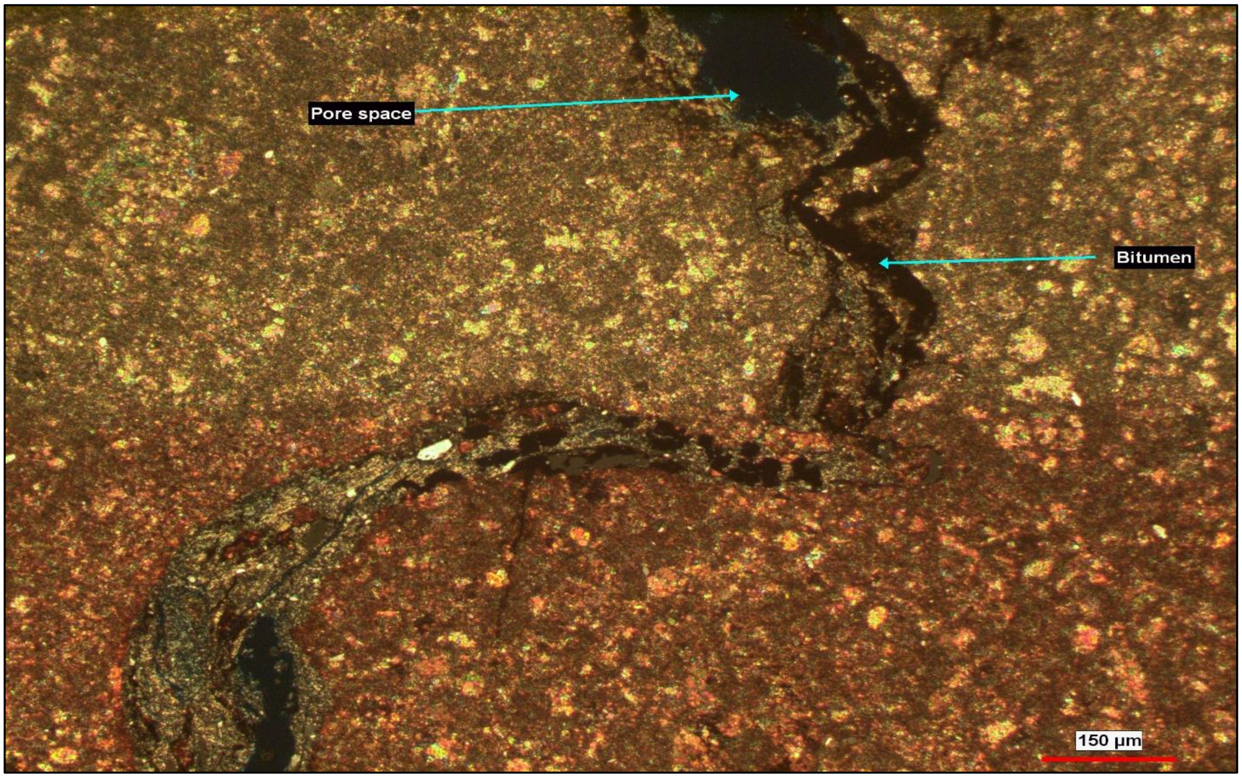

Figure 3-50. Sample ING-22. Possible bitumen through vein calcite. Note the large pore spaces. Photo is in cross polarized light. The upper half of the photo is unstained calcite.

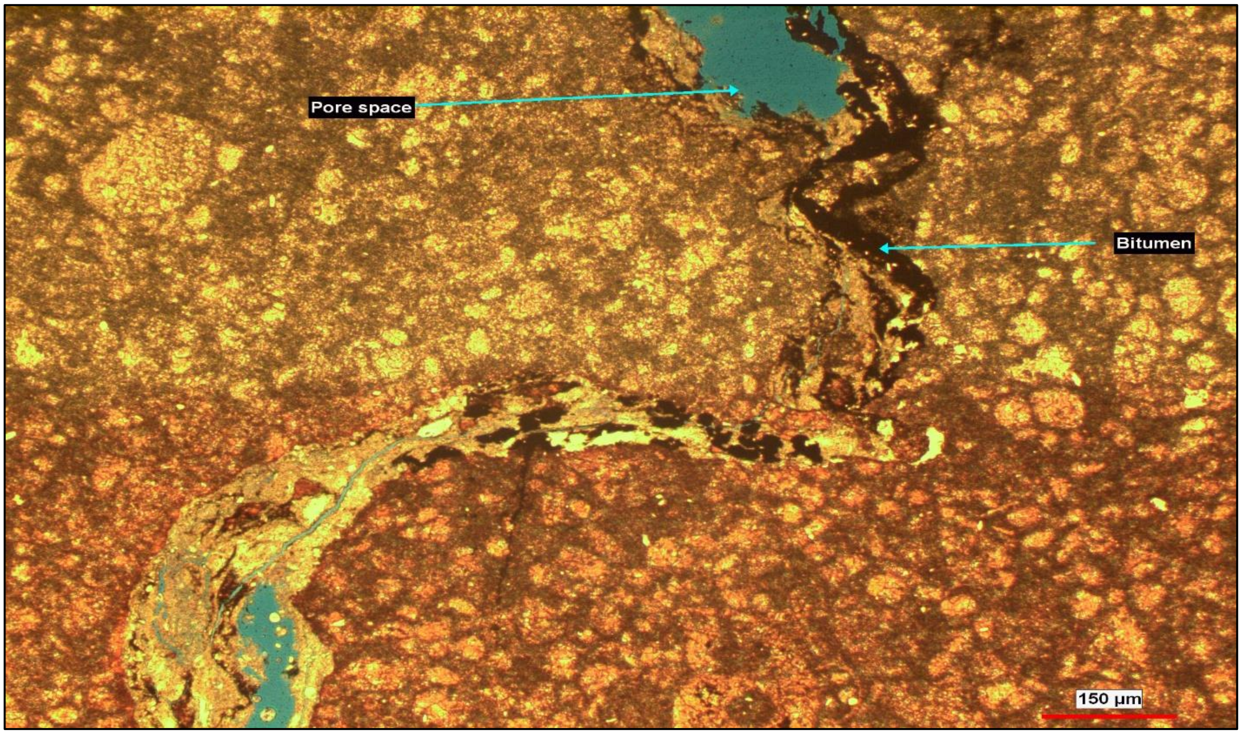

Figure 3-51. Sample ING-22. Same as the previous figure but in plane-polarized light. The blue color is porosity and the black is the bitumen. The upper half of the photo is unstained calcite.

ING- 23 (Bed 5):

The sample is composed mainly of dolomite with lesser calcite and minor very fine quartz sand grains. The dolomite crystals are mainly euhedral, variable in shape, and fairly uniform in size, and the calcite is distributed between the dolomite crystals. The sample also contains small veins filled with calcite. There is rare intergranular, intragranular, and fracture porosity. The intergranular pore spaces contain some traces of dark material that may be residue of bitumen.

ING- 24 (Bed 4):

The sample consists of calcite with rare sand grains. The texture looks different from the other carbonate samples. The texture shows circular groups of large calcite crystals with rims formed by very small calcite crystals (Fig. 3.52, 3.53). This texture is clearer in plane-polarized light. The texture suggests the rock was originally composed of ooids, which have recrystallized.

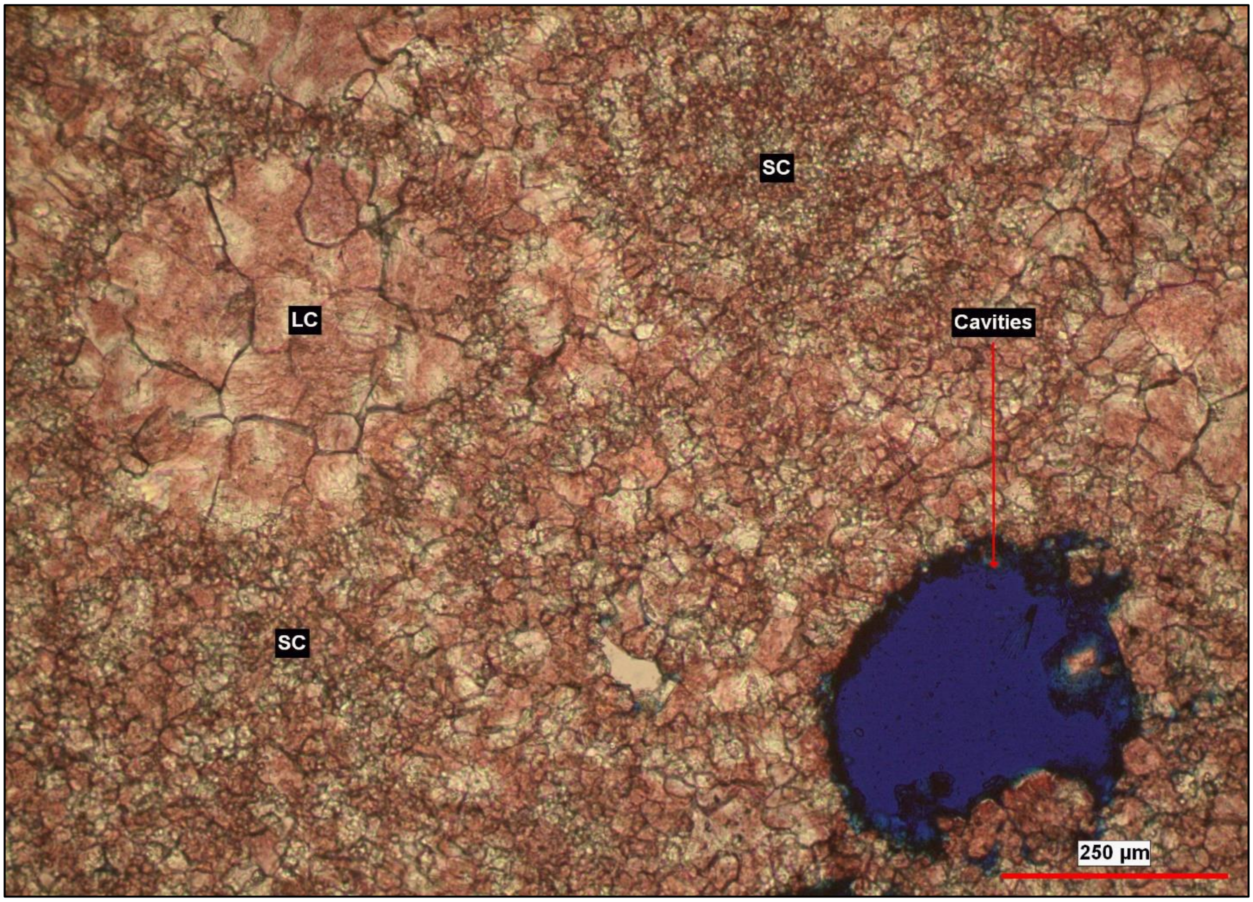

Figure 3-52. Sample ING-24. (LC) are the large calcite crystals that are surrounded by (SC) the small calcite crystals. Note the cavities in plane-polarized light.

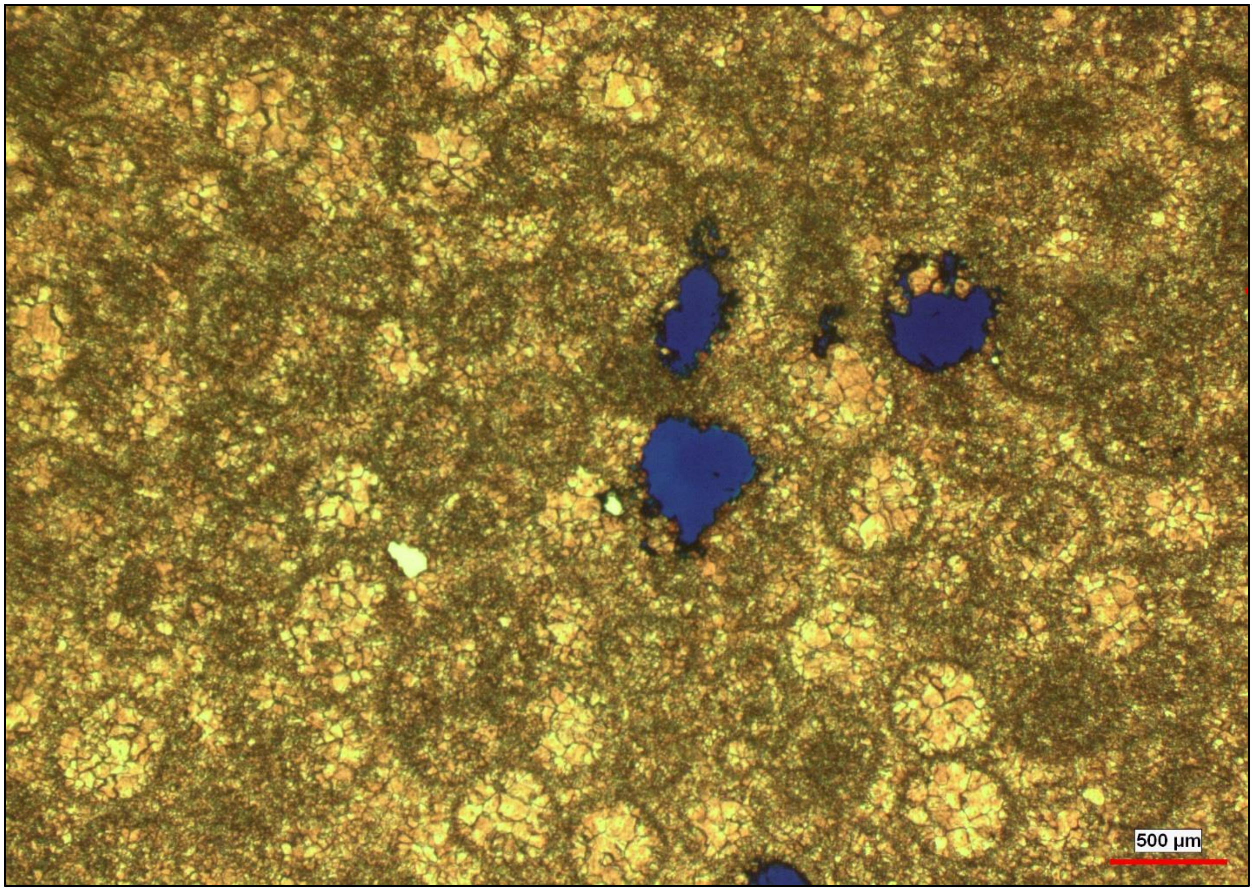

Figure 3-53. Sample ING-24. Same as the previous figure but with a different scale. This more clearly shows the rounded shape of the calcite patches. Porosity is filled by blue-dyed epoxy. Photo is in plane-polarized light.

The sample contains fractures, including some that are filled with calcite and some just hosting porosity. Also, it contains some large cavities dispersed throughout the sample. Small traces of dark material, possibly residue after bitumen, are associated with the cavities. Porosity is mainly in fractures and large cavities, with minor intergranular porosity.

ING- 25 (Bed 4):

The sample is composed of calcite with minor very fine scattered sand grains. The sand grains are angular and sub-angular with high sphericity. Large calcite crystals are surrounded by smaller calcite crystals, which are the most abundant. This sample contains traces of dark material that may be residue of bitumen. The sample contains some crinoid fossil fragments (Fig. 3.54). Porosity is almost absent, except minor intergranular porosity.

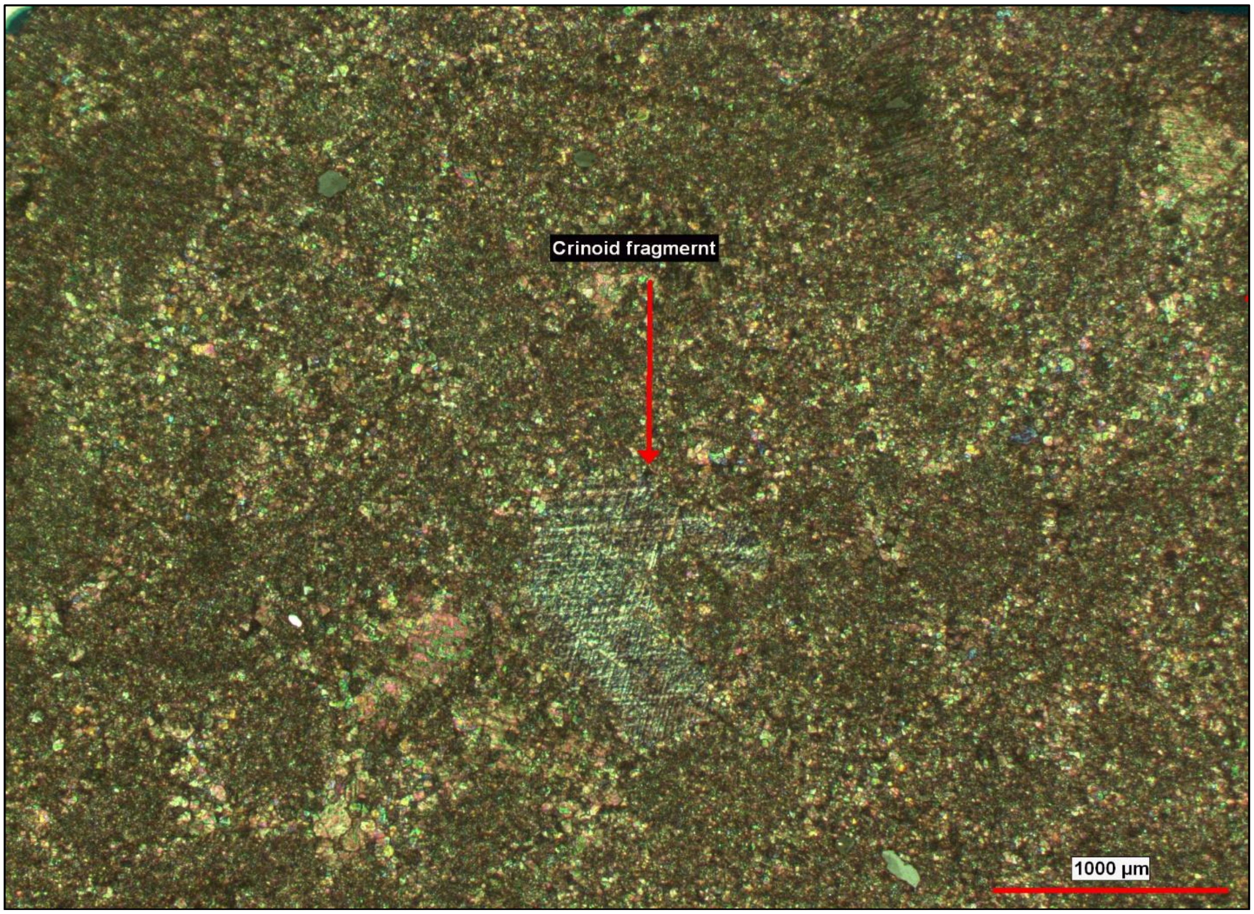

Figure 3-54. Sample ING-25. Crinoid fragment in cross polarized light.

ING- 26 (Bed 4):

The sample consists mainly of very fine calcite with minor dolomite. There are some scattered very fine sand grains composed of quartz. The sand grains are angular, but some grains are rounded with high sphericity. The sample contains some fossil fragments, including crinoid columnals. There is rare intergranular porosity in the sample.

ING-28 (Bed 3):

The sample is composed of very fine to fine, well sorted sand grains with some fossil fragments. The sand grains consist of quartz and minor K-feldspar, albite, glauconite, zircon and opaques. The grains are well cemented mainly with calcite, as well as lesser dolomite, hematite, kaolinite, and silica. The grains are mainly angular, with some sub-rounded or rounded, but most of them are angular with low sphericity. Sphericity is generally low, although there are some grains with high sphericity. The grains have point, long, and concavo-convex contacts, with point contacts the most common. In addition, the sample contains some partially dissolved feldspar grains and some grains that are partially replaced by the calcite cement. The sample is laminated on the scale of a few mm, with the laminations defined by variation in grain size and degree of cementation. The porosity, mainly intergranular, is abundant and includes some cavities and intragranular porosity. There is a very small amount of dark material that may be a residue of bitumen. Overall, the sample is texturally sub-mature, based on the sorting, angular grains and the lack of clay.

ING-30 (Bed 3):

Sand gains present are well-sorted and mainly very fine, with a few fine grains. The grains are composed of quartz and minor K-feldspar, albite, glauconite, chert, zircon, opaques, and carbonate rock fragments (some around 0.34 mm in size) (Fig. 3.55). Most of the grains are angular in shape, but some are sub-rounded, and some have point contacts and high sphericity. The sample contains fossil fragments in the carbonate rock fragments (Fig. 3.56). The grains are well cemented, mainly with patchy calcite, as well as dolomite, hematite, kaolinite, and silica overgrowths. The porosity is mainly intragranular.

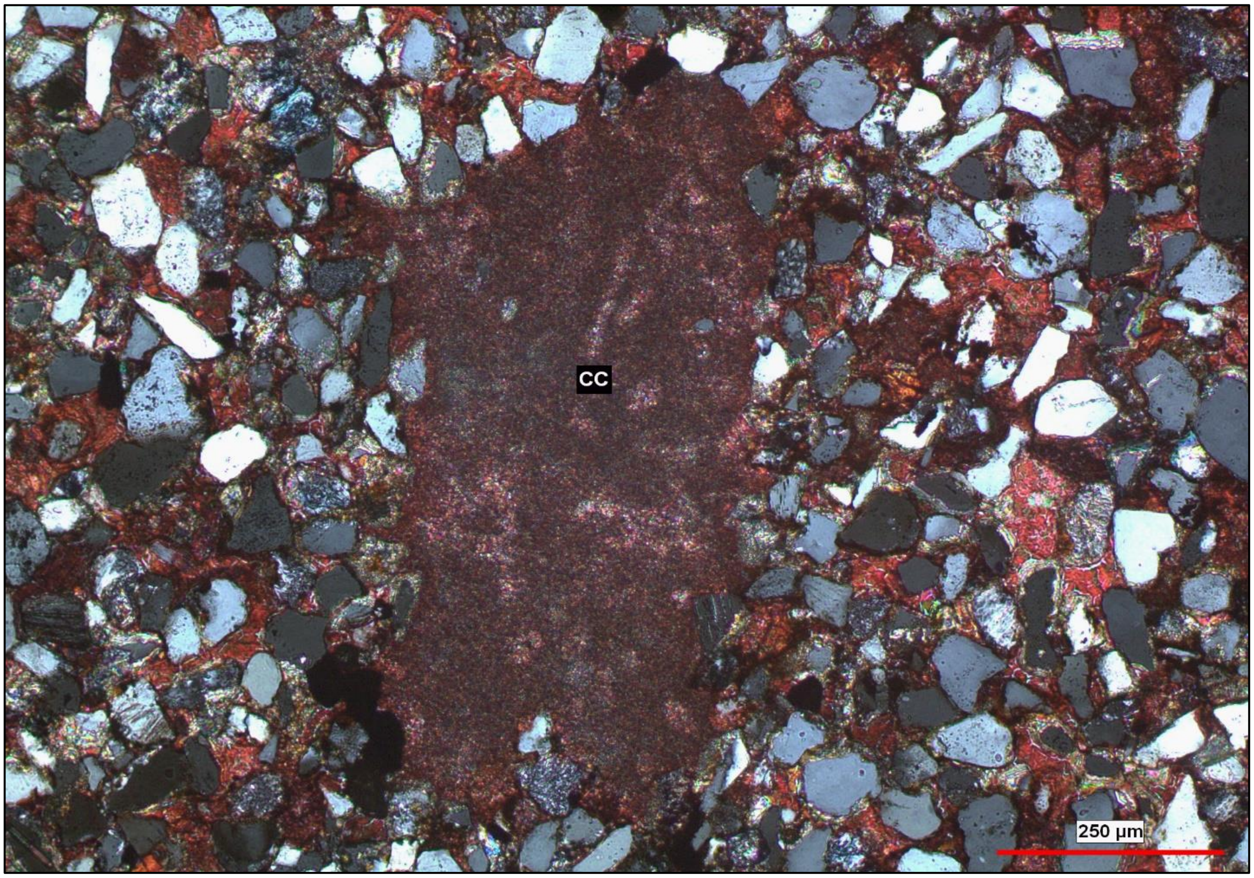

Figure 3-55. Sample ING-30. (CC) are carbonate clasts that are surrounded by quartz grains. Photo is in cross polarized light.

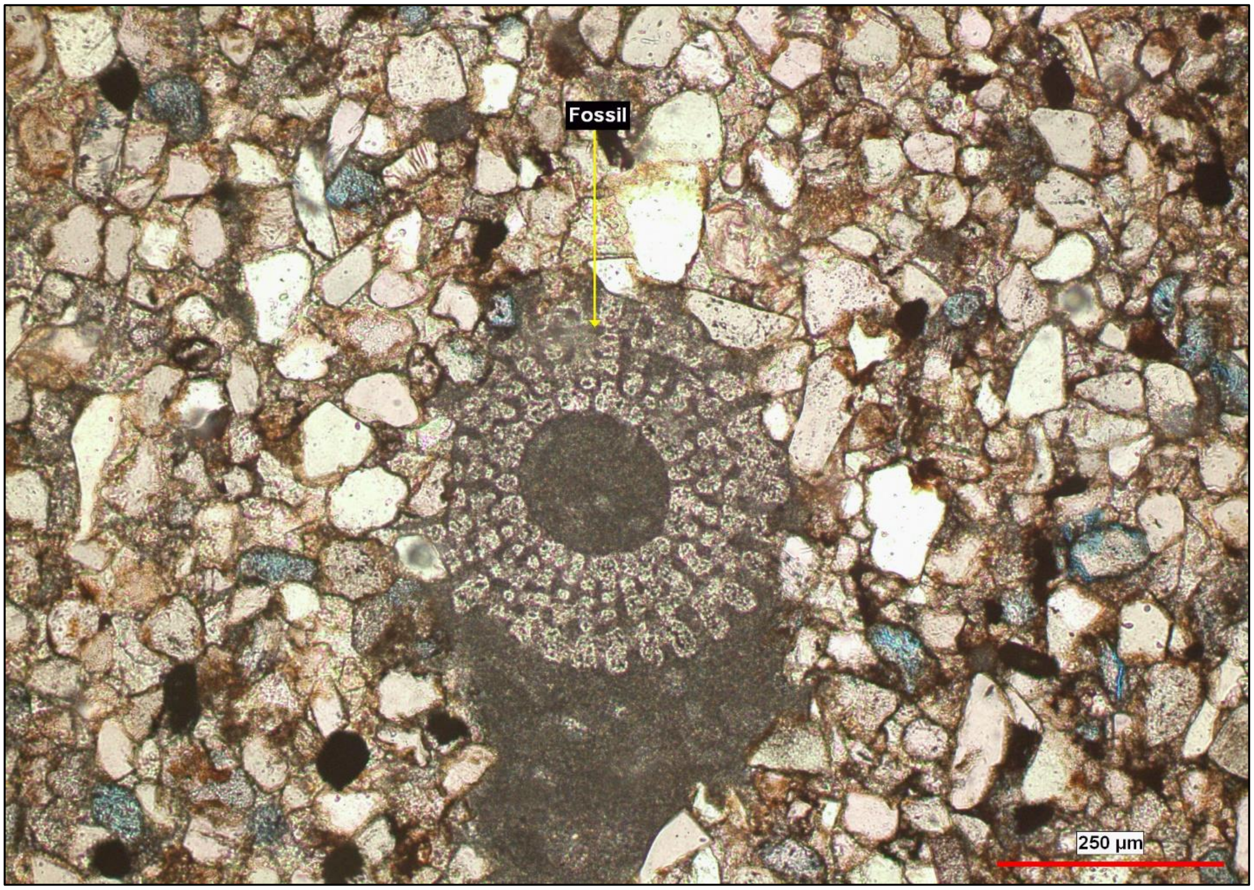

Figure 3-56. Sample ING-30. Shows well preserved fossil (probably coral). Photo is in plane-polarized light.

ING-32 (Bed 2):

The sample is composed of very small carbonate crystals. Most of these crystals are calcite, with some irregular dolomite patches. There are some large calcite crystals in veins. There is almost no porosity except for a small amount of fracture porosity. No evidence of hydrocarbons is observed in the sample.

ING-33 (Bed 2):

The sample consists of very small and large calcite crystals, with some small dolomite crystals. The small calcite crystals dominate the sample. The sample contains some scattered very fine and fine sand grains that are composed of quartz. The sand grains are angular to sub-rounded and some grains are well-rounded. Most of the sand grains have high sphericity. There are some sand grains that have point and long contacts. The sample has some porosity, including intergranular and intragranular.

ING-34 (Bed 1):

The sample consists of well-sorted very fine, fine, and medium sand grains. These grains are composed of quartz and minor K-feldspar, chert, and albite. Most grains are angular to sub-rounded, with some grains well-rounded; most have low sphericity. The grains have point, long, and concavo-convex contacts. The sample is well cemented with calcite cement, which is the dominant cement. There are also dolomite, kaolinite, and silica cements. Rare porosity is intergranular and intragranular.

ING-35 (Bed 1):

The sample consists of well-sorted very fine and fine sand grains. These grains are composed of quartz and minor K-feldspar, albite, biotite, muscovite, and opaques. The mica minerals (biotite and muscovite) are more abundant in this sample. The grains are mostly angular to sub-rounded, but some grains are well-rounded. The grains have low to moderate sphericity. The long contacts between the sand grains suggest the grains were affected by compaction. Some of the feldspar grains are partially dissolved. The sample is well cemented with calcite which is the common cement, and is patchy in some areas of the samples. There is also dolomite, kaolinite, and silica cement. Porosity is both intergranular and interagranular.

3.4.2 Quantitative Petrographic Analysis

Overall, point-counted data show most sandstone samples to be quartz arenites, with one subarkose, one sublitharenite, and one litharenite, using the classification scheme of Folk (1974) (Fig. 3.57). The variable rounding and the typically moderate degree of sorting, indicate most of the sandstone samples can be considered texturally sub-mature to mature.

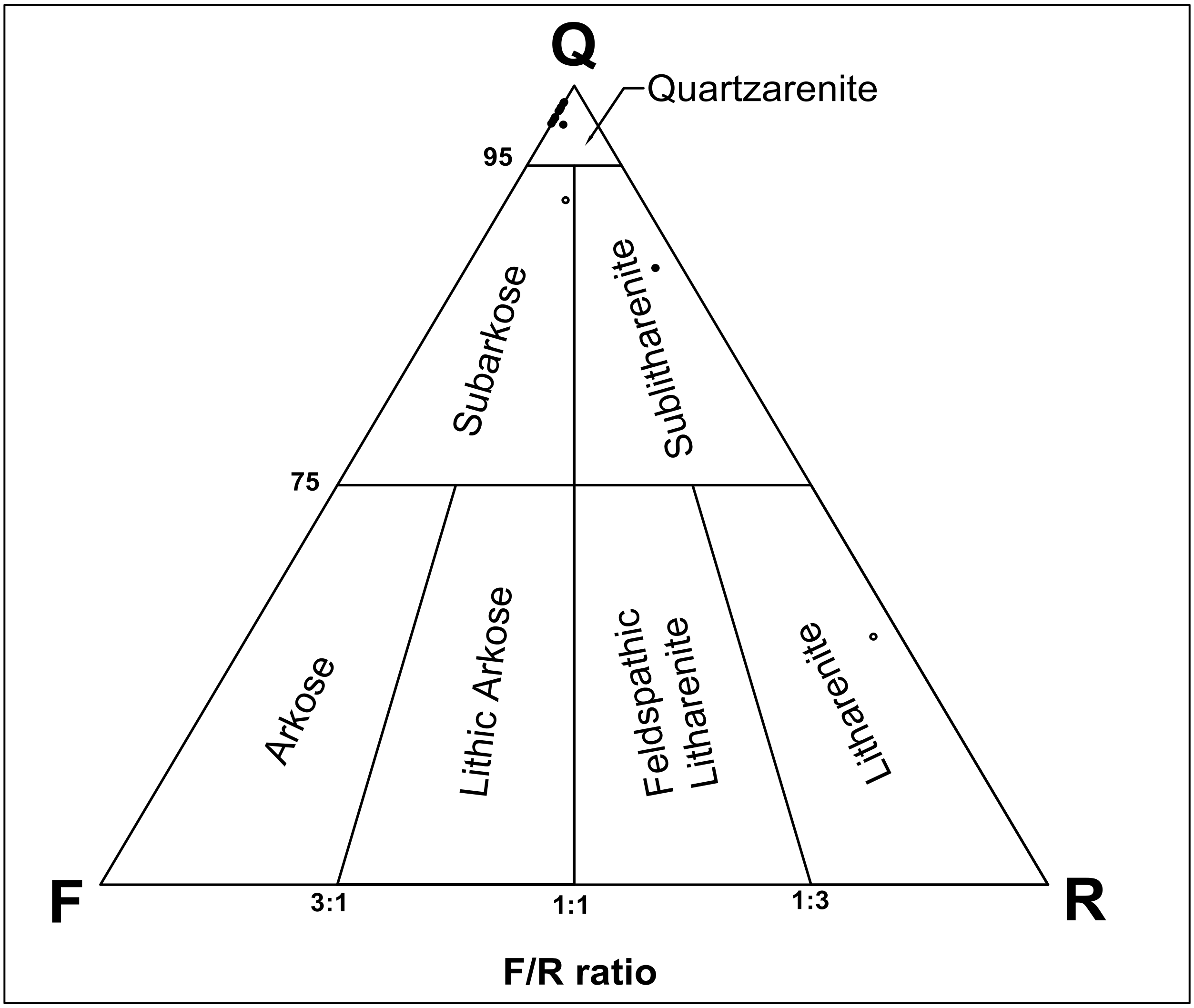

Figure 3-57. Sandstone classification of the Ingleside Formation sandstones. Most of the samples plot in the quartz arenite field (classification of Folk, 1974).

Table 3.1. Sandstone point counting results given as % by sample, and average and standard deviation for the analyzed sandstones. A minimum of 250 points were counted for each sample. Std = standard deviation; Ave = average.

Sample NO	Bed NO	Quartz	Calcite cement	Dolomite cement	Porosity	Hematite cement	Quartz cement	kaolinite cement	Opaque minerals	Albite	Rock fragments	K-feldspar	Biotite	Muscovite	Chert	Glauconite	Siderite
ING-1	Bed 14	61.6	0.4	21.6	4	4.4	4.4	0.8	0.8	1.6	0	0	0	0	0.4	0	0
ING-2	Bed 14	59.2	4.8	8	17.2	4.8	1.2	2	0.4	1.2	0	0.8	0	0	0.4	0	0
ING-5	Bed 13	52	13.6	4.4	21.2	4.8	2.8	0	0	0	0	0.8	0	0	0.4	0	0
ING-6	Bed 13	66.4	2.8	12.4	6	0.4	0	6.8	2	0.8	0.8	0.8	0	0	0	0.8	0
ING-9	Bed 11	64.4	6.4	22	0.8	0	2.4	0	2.4	1.2	0	0.4	0	0	0	0	0
ING-10	Bed 11	54	26.4	14.4	0.8	0	0	0	0.8	0	0	1.6	0.4	0.8	0	0	0.8
ING-11	Bed 10	54.4	1.6	40	0.8	0	0.4	0	1.2	0.4	0	0	0	0	0.8	0.4	0
ING-12	Bed 10	65.6	2.4	21.2	7.6	0	0	2	0.8	0.4	0	0	0	0	0	0	0
ING-14	Bed 10	36.4	40.4	1.2	0	0	0	0	0.8	0.4	19.6	1.2	0	0	0	0	0
ING-21	Bed 6	63.6	10.8	16.8	5.6	0	0	1.6	0.8	0.4	0	0.4	0	0	0	0	0
ING-28	Bed 3	59.6	28	1.2	8.8	0	0	0	0.4	0.8	0	0.8	0	0	0	0.4	0
ING-30	Bed 3	53.6	34.3	0	1.2	0	0	0	2	0.8	6.8	0.8	0	0	0	0.4	0
ING-34	Bed 1	64.8	30.8	0.4	0.8	0	2	0	0	0.4	0	0.4	0	0	0.4	0	0
ING-35	Bed 1	67.6	14.4	0	8.8	0	0.8	0.4	1.2	0.8	0	0.4	3.6	2	0	0	0
Ave	-	58.8	15.5	11.7	5.97	1.11	1.00	1.05	1.05	0.66	2.09	0.60	0.31	0.22	0.17	0.15	-
Std	-	8.31	13.8	11.8	6.48	2.03	1.39	1.90	0.70	0.46	5.58	0.46	1.00	0.58	0.26	0.26	-

Quartz, mainly monocrystalline, varies in abundance within the sandstones, but is a very high proportion of the sand grains in all sandstone samples, except ING-14. Feldspar, including both albite and potassium feldspar, is present in most samples in small amounts. Some of the feldspar grains are partially dissolved or partially altered. Rock fragments, mainly carbonate, are present in a few samples. Minor biotite and muscovite are present in a few samples with somewhat more in the two stratigraphically lowest samples. Additionally, chert, glauconite, and siderite are present in small amounts in a few samples. The small amount of glauconite present is well-rounded. Opaque minerals are present in most samples, but in small amounts. Porosity varies from sample to sample, and includes intergranular and intragranular porosity formed by dissolution of feldspar. The two samples with the highest porosity are relatively high stratigraphically, but there is otherwise no stratigraphic trend in porosity apparent.

Cements include calcite, dolomite, kaolinite, quartz overgrowths, and hematite (Fig. 3.58) Calcite is the dominant cement in some samples and dolomite in others. Calcite cement is generally more abundant in stratigraphically lower samples. Calcite cement is patchy in some samples. Dolomite cement content is variable, but generally higher in samples from the middle and upper parts of the section studied (Fig. 3.59). It is sometimes patchy with large and small crystals. In some samples the dolomite and calcite cement appear to have partially replaced some quartz grains and altered some feldspar grains. Carbonate cement is observed to occur in three types, poikilotopic dolomite cement, blocky calcite cement, and blocky dolomite cement. Poikilotopic cement precipitated between grains that are not affected much by compaction, and grains coated with hematite cement (Fig. 3.46, 47). The blocky calcite and dolomite cements are present with grains that are affected by compaction (Fig. 3.24). The grains that are cemented with the carbonate blocky cement are sometimes rimmed with hematite cement (Fig. 3.25).

Hematite cement is not abundant, and is more common in samples near the top of the section studied. Hematite cement coats some grains or has precipitated between grains boundaries. Kaolinite cement appears in some samples, but is not common. In some samples it fills large pore spaces. Quartz overgrowth cement is minor, and particularly scarce in the middle part of the section. The sum of each component for all points counted is shown in Table 3.2.

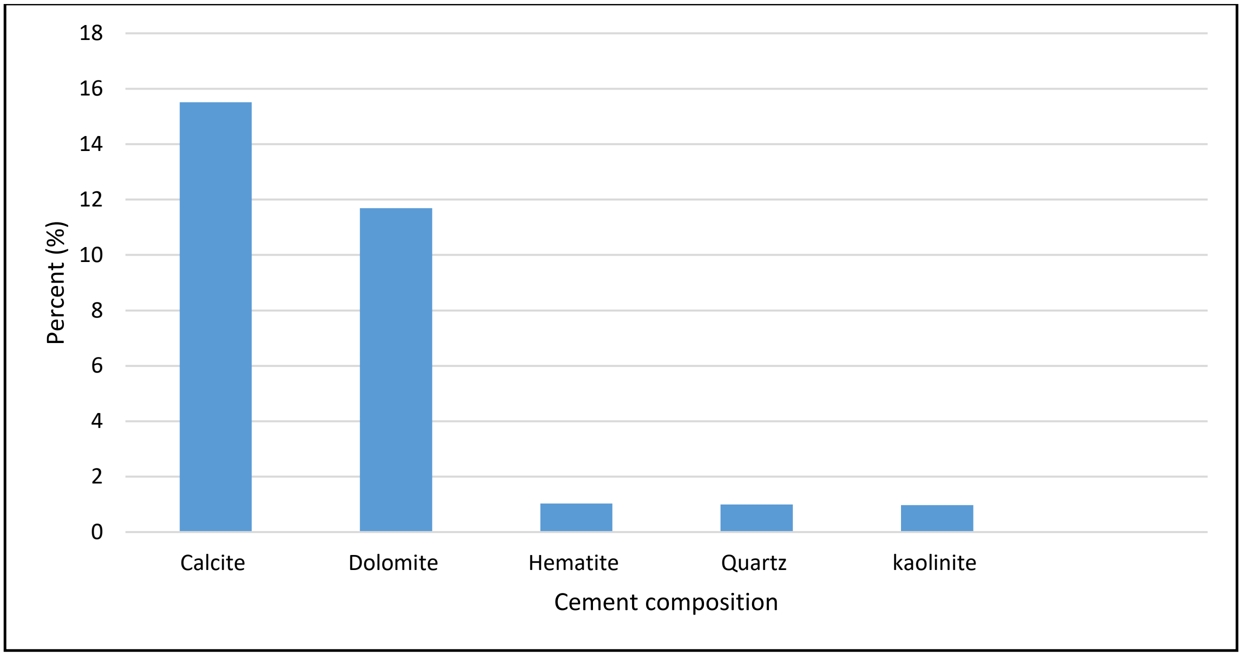

Figure 3-58. Average percent of each type of cement in sandstones from point count data.

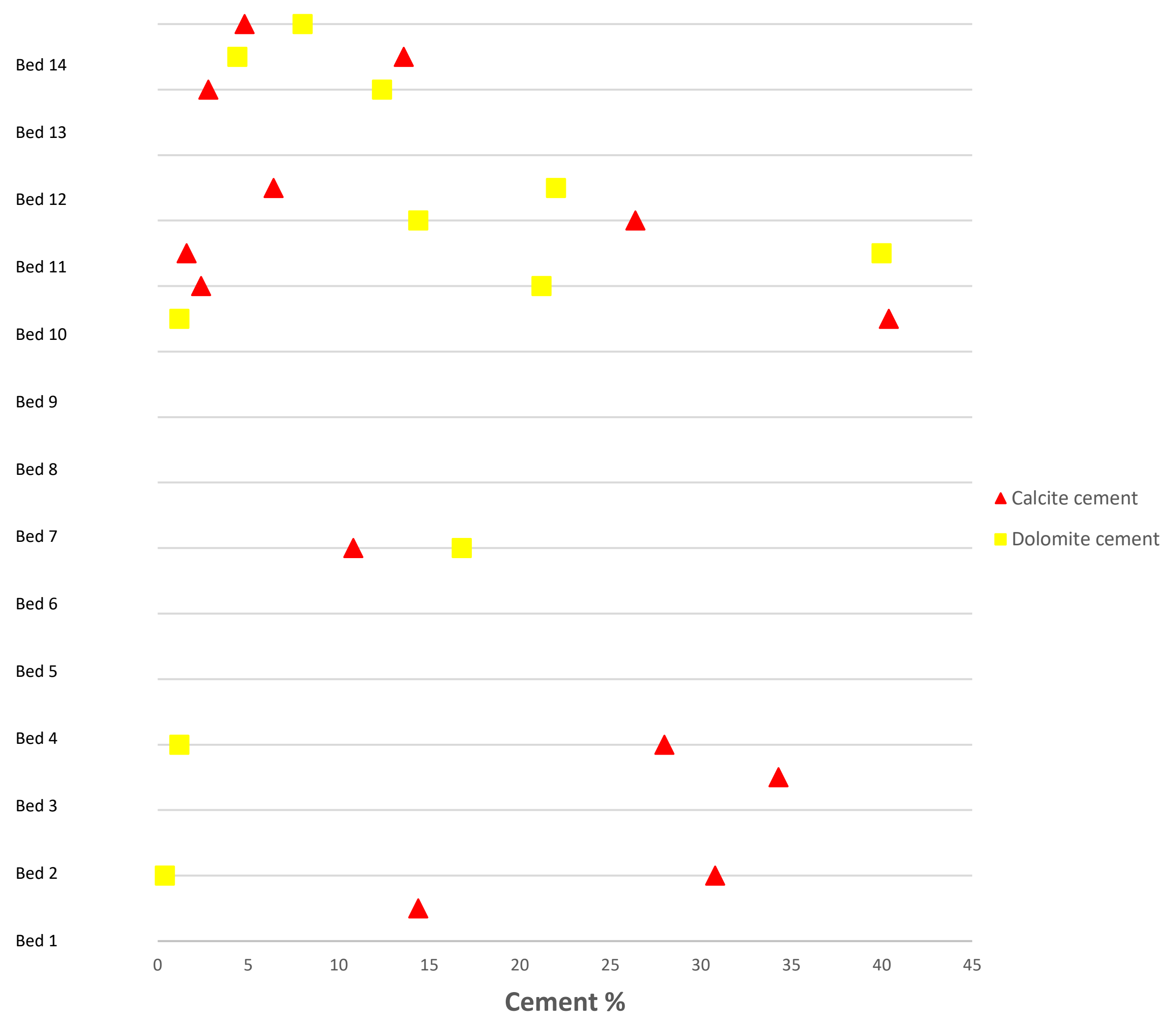

Figure 3-59. Variation in calcite and dolomite cements in sandstones with approximate stratigraphic position.

Table 3.2. The sum of each component for all points counted in sandstones.

Point Counted	The Sum of each point counted	Percent (%)
Quartz	2058	58.8
Calcite cement	543	15.5
Dolomite cement	409	11.7
Porosity	209	5.97
Rock fragments	68	1.94
Hematite cement	36	1.03
Quartz cement	35	1
Kaolinite cement	34	0.97
Opaque minerals	34	0.97
Albite	23	0.66
K-feldspar	21	0.60
Biotite	10	0.29
Muscovite	7	0.20
Chert	6	0.17
Glauconite	5	0.14
Siderite	2	0.06
Total	3500	100

3.5 Geochemistry

The purpose of studying the geochemistry of the Ingleside is to understand the chemical composition and chemical variations and to permit evaluation of geochemical effects of diagenesis. The quality of the geochemical data presented here appears to be poor and that is further addressed in the discussion chapter. Also, as noted in the methods chapter, the detection limits reported here were not determined for these analyses. The average and the standard deviation of the major elements for each sample are shown in Table 3-3. Among the major elements for which analyses were obtained, the Ingleside Formation is predominantly composed of Si, Al, Fe, Mg, and Ca, with lesser amounts of Ti, Mn and K. All but one value for P are below the detection limit published by the manufacturer of the XRF unit and are therefore not reported. Among the trace elements analyzed, those generally above the published detection limits are S, Sr, Rb, V, Cr, Cu, Zn, Zr, Pb, whereas Ni and Y values are below detection limits (10 ppm and 2 ppm, respectively) in most samples (Table 3-4). Some trace elements, including Co, Nb, U, Th, As, Cd, Sn, Sb, W, Pt, Au, Hg, Rh, Ag, Mo, and Pd, are not included in Table 3-4 because most or all of their values are below detection. There are samples for which one of the four analyses conducted was just above detection and the other three were below detection, so the average was treated as below detection.

The data (Table 3.3, Fig. 3.60) show that the sandstone samples are variable in SiO_2, which ranges from 60 to 80 wt. %. Al_2O_3 values for sandstone samples are higher for the stratigraphically higher samples, and range from 1.4 to 6.8 wt. % (Fig. 3.61). The content of CaO for sandstone samples ranges from 7.9 to 22 wt. % and is highest in the two stratigraphically lowest sandstone samples (Fig. 3.62). The data for Fe_2O_3 in the sandstones (Fig. 3.63) varies from 0.45 to 2.5 wt. %. Concentration of MgO ranges from below detection to 7.8 wt. % (Fig.

3.64), with the stratigraphically lowest beds having no detectable MgO. The K_2O values vary for sandstone but are mostly low, and range from 0.036 to 2 wt. %. (Fig. 3.65). The MnO sandstone values (Fig. 3.66) range from 0.010 to 0.030 wt. %, and are higher for the stratigraphically higher samples. The TiO_2 sandstone values range from 0.086 to 0.32 wt. % with higher concentrations for the stratigraphically higher samples (Fig. 3.67).

Table 3.3. Major elements reported as weight percent % oxide. Std = standard deviation; b.d. = below manufacturer's published limit of detection. Ave = average; SS = sandstone; DO = dolomite; LST = limestone.

Sample NO	Bed NO	Rock Type	Number of Analyses	Ave SiO_2	Std	Ave TiO_2	Std	Ave Al_2O_3	Std	Ave Fe_2O_3	Std	Ave MnO	Std	Ave MgO	Std	Ave CaO	Std	Ave K_2O	Std
Published Detection Limits				**0.17**		**0.0017**		**0.26**		**0.0029**		**0.0009**		**1.65**		**0.0049**		**0.006**	
GS-14	Bed 14	SS	4	72	1	0.27	0.058	4.8	0.25	0.91	0.12	0.015	0.004	1.9	0.27	10	0.79	1	0.085
GS-13	Bed 13	SS	4	66	2.1	0.16	0.0056	4.5	0.37	0.78	0.042	0.025	0.0014	5.5	0.32	8.9	0.08	0.84	0.039
GS-12	Bed 12	DO	4	11	1.9	0.08	0.018	1	0.25	0.25	0.052	0.14	0.0049	19	0.79	33	1.1	0.055	0.03
GS-11	Bed 11	SS	4	60	3.5	0.32	0.026	6.8	0.43	2.5	0.19	0.03	0.0042	7.8	0.28	12	1.4	2	0.19
GS-10	Bed 10	SS	4	63	7.1	0.086	0.024	1.5	0.17	0.45	0.025	0.028	0.0013	6.7	0.3	16	3	0.036	0.037
GS-9	Bed 9	DO	4	8.7	5.3	0.044	0.029	0.48	0.23	0.32	0.048	0.19	0.023	20	1	35	0.54	b.d.	-
GS-8	Bed 8	SS	4	80	1.7	0.16	0.011	4.3	0.29	0.94	0.27	0.017	0.0007	3.7	0.23	7.9	0.28	0.18	0.1
GS-7	Bed 7	DO	3	3.1	0.31	0.049	0.005	0.39	0.1	0.28	0.069	0.04	0.0037	23	0.51	36	0.13	b.d.	-
GS-6	Bed 6	DO	4	32	3.5	0.29	0.012	4.9	0.63	2.3	0.54	0.072	0.0048	14	0.46	25	0.85	1.2	0.19
GS-5	Bed 5	DO	3	1.7	0.48	0.047	0.0038	b.d.	-	0.12	0.024	0.13	0.0018	19	1.3	37	1.3	b.d.	-
GS-4	Bed 4	LST	4	1.6	0.1	0.071	0.0094	b.d.	-	0.094	0.028	0.015	0.0015	b.d.	-	61	0.7	b.d.	-
GS-3C	Bed 3	LST	4	39	8.6	0.071	0.018	1.6	0.35	0.17	0.016	0.0085	0.0013	b.d.	-	41	6.6	b.d.	-
GS-3B	Bed 3	LST	3	19	3.2	0.085	0.0036	1.1	0.22	0.25	0.028	0.012	0.0016	b.d.	-	53	0.61	b.d.	-
GS-3A	Bed 3	SS	4	62	0.71	0.17	0.051	2.8	0.21	0.63	0.087	0.015	0.0017	b.d.	-	22	1.3	0.68	0.081
GS-2	Bed 2	LST	4	1.8	0.14	0.074	0.0075	b.d.	-	0.11	0.0073	0.02	0.0021	b.d.	-	61	0.4	b.d.	-
GS-1	Bed 1	SS	4	66	1.7	0.1	0.048	1.4	0.26	0.46	0.07	0.01	0.001	b.d.	-	22	2.8	0.087	0.064

Table 3.4. Trace elements reported as parts per million (ppm). Std = standard deviation; b.d. = below manufacturer’s published limit of detection; SS = sandstone; DO = dolomite; LST = limestone.

Sample No	Bed NO	Rock Type	Number of Analyses	S	Std	Rb	Std	Sr	Std	V	Std	Cr	Std	Ni	Std	Cu	Std	Zn	Std	Zr	Std	Pb	Std	Y	Std
Published Detection Limits				**150**		**2**		**2**		**10**		**9**		**10**		**6**		**3**		**2**		**4**		**2**	
GS-14	Bed 14	SS	4	b.d.	–	33	1.7	59	3.1	130	84	32	32	b.d.	–	28	25	8	0.82	201	57	7.3	0.96	3.3	1.3
GS-13	Bed 13	SS	4	1013	930	24	1.7	45	1	144	23	b.d.	–	b.d.	–	8.8	4	10	1.5	140	13	5	0	b.d.	–
GS-12	Bed 13	DO	4	b.d.	–	3.8	0.96	27	1.7	b.d.	–	36	21	b.d.	–	b.d.	–	13	2.5	18	13	4.5	2.1	b.d.	–
GS-11	Bed 11	SS	4	481	97	58	2.5	130	3.7	166	26	46	28	16	8.4	14	0.82	19	1.2	121	13	9	1.2	10	0.82
GS-10	Bed 10	SS	4	b.d.	–	9.3	0.96	39	3.5	56	59	37	22	b.d.	–	9.3	4.2	10	2.3	68	19	b.d.	–	b.d.	–
GS-9	Bed 9	DO	4	530	331	b.d.	–	67	13	45	80	74	23	b.d.	–	6.5	4.1	19	3.3	12	9.7	b.d.	–	b.d.	–
GS-8	Bed 8	SS	4	176	122	15	1.7	78	4.3	b.d.	–	47	29	b.d.	–	8.5	3.8	8.3	1.5	113	9.2	5.8	2.1	b.d.	–
GS-7	Bed 7	DO	3	355	75	b.d	–	29	1	84	69	b.d.	–	b.d.	–	b.d.	–	9.7	1.5	4	0.58	b.d.	–	b.d.	–
GS-6	Bed 6	DO	4	224	130	35	5.5	62	4.1	105	67	49	31	16	7.1	12	1.8	28	4.3	77	12	4.5	1.7	10	0.96
GS-5	Bed 5	DO	3	802	239	b.d.	–	52	0.58	b.d.	–	b.d.	–	b.d.	–	8	4.4	19	0.58	b.d.	–	b.d.	–	b.d.	–
GS-4	Bed 4	LST	4	b.d.	–	b.d.	–	82	0.96	114	74	36	36	b.d	–	b.d.	–	7	0.82	b.d.	–	4.3	2.6	b.d.	–
GS-3C	Bed 3	LST	4	b.d.	–	3.5	1	79	11	75	80	42	25	b.d.	–	b.d.	–	4.5	3.5	42	11	6	0.82	b.d.	–
GS-3B	Bed 3	LST	3	b.d.	–	2.7	1.2	106	5.5	b.d.	–	50	39	b.d.	–	11	9.1	8.7	3.8	16	4.4	6	1.7	b.d.	–
GS-3A	Bed 3	SS	4	b.d.	–	23	1.5	70	2.5	81	94	48	32	b.d.	–	7	4.7	8.5	1.7	93	55	7.8	2.2	2.8	0.5
GS-2	Bed 2	LST	4	b.d.	–	b.d.	–	252	19	73	78	76	10	13	8.7	7.3	4.9	7.8	1.7	6.5	1.3	b.d.	–	b.d.	–
GS-1	Bed 1	SS	4	b.d.	–	8.5	3.8	77	8.3	68	73	b.d.	–	b.d.	–	11	5	7.5	1.9	106	94	7	2.2	b.d.	–

In carbonate samples the concentration of SiO_2 ranges from 1.6 to 39 wt. % in limestone and from 1.7 to 32 wt. % in dolomite (Fig. 3.60). The Al_2O_3 content (Fig. 3.61) varies in carbonate samples, ranging from 0.39 to 4.9 wt. %. The carbonate samples show high values of CaO, higher in limestone samples than in dolomite samples, ranging from 25 to 61 wt. % (Fig. 3.62). Dolomite samples show MgO values ranging from 14 to 23 wt. %, whereas in all limestone samples MgO values are below detection (Fig. 3.64). Fe_2O_3 content in limestone and dolomite samples varies from 0.094 to 2.3 wt. % (Fig. 3.63). The MnO concentration for all carbonate samples ranges from 0.0085 to 0.19 wt. %, and is higher in dolomite than in limestone (Fig. 3.66). The TiO_2 content varies in carbonate samples, ranging from 0.044 to 0.29 wt. % (Fig. 3.67). Finally, the carbonate samples do not have detectable K_2O except for two dolomite sample at 0.055 and 1.2 wt. % (Fig. 3.65).

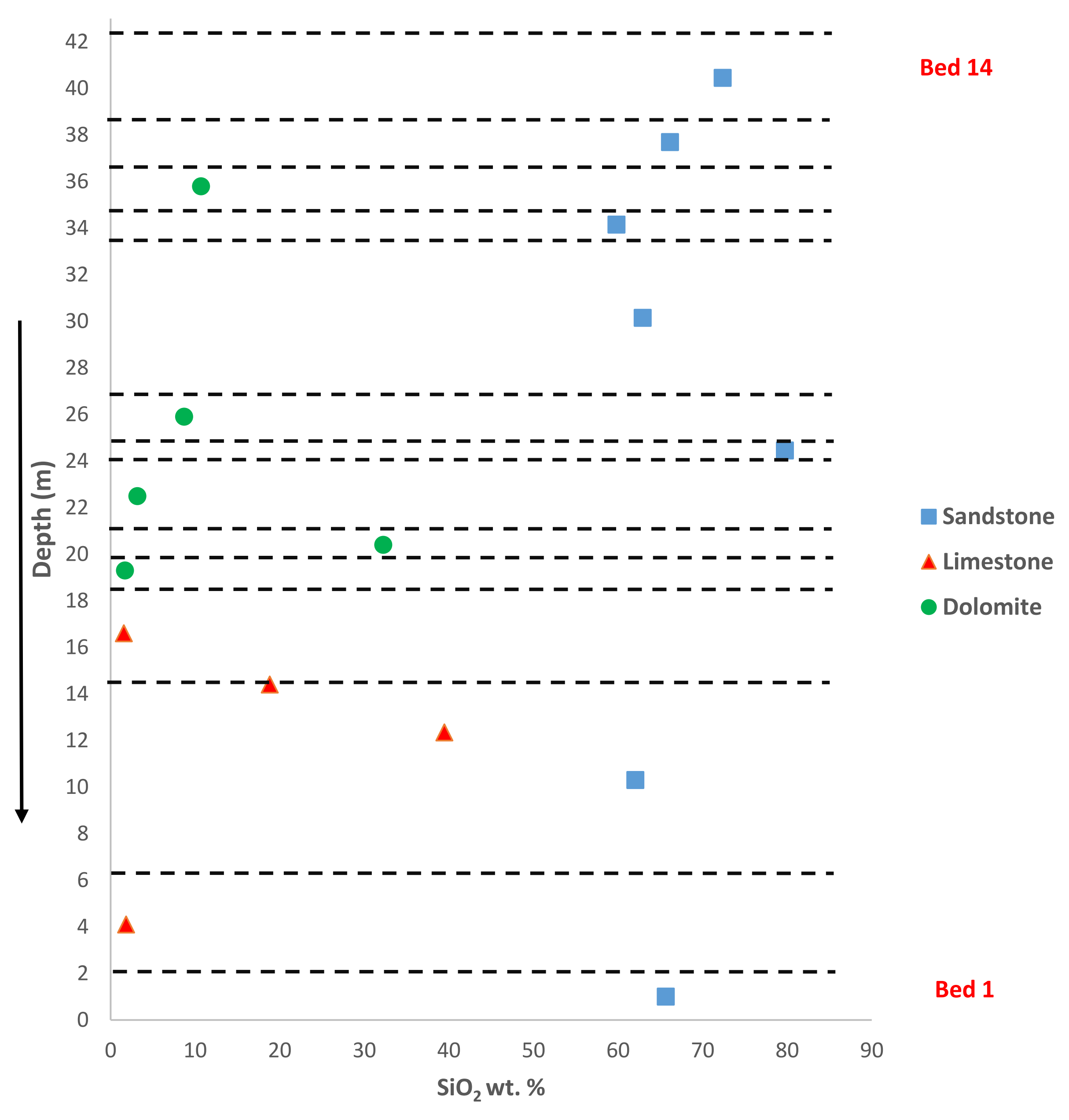

Figure 3-60. SiO$_2$ weight % versus depth. The black dashed lines represent bed contacts.

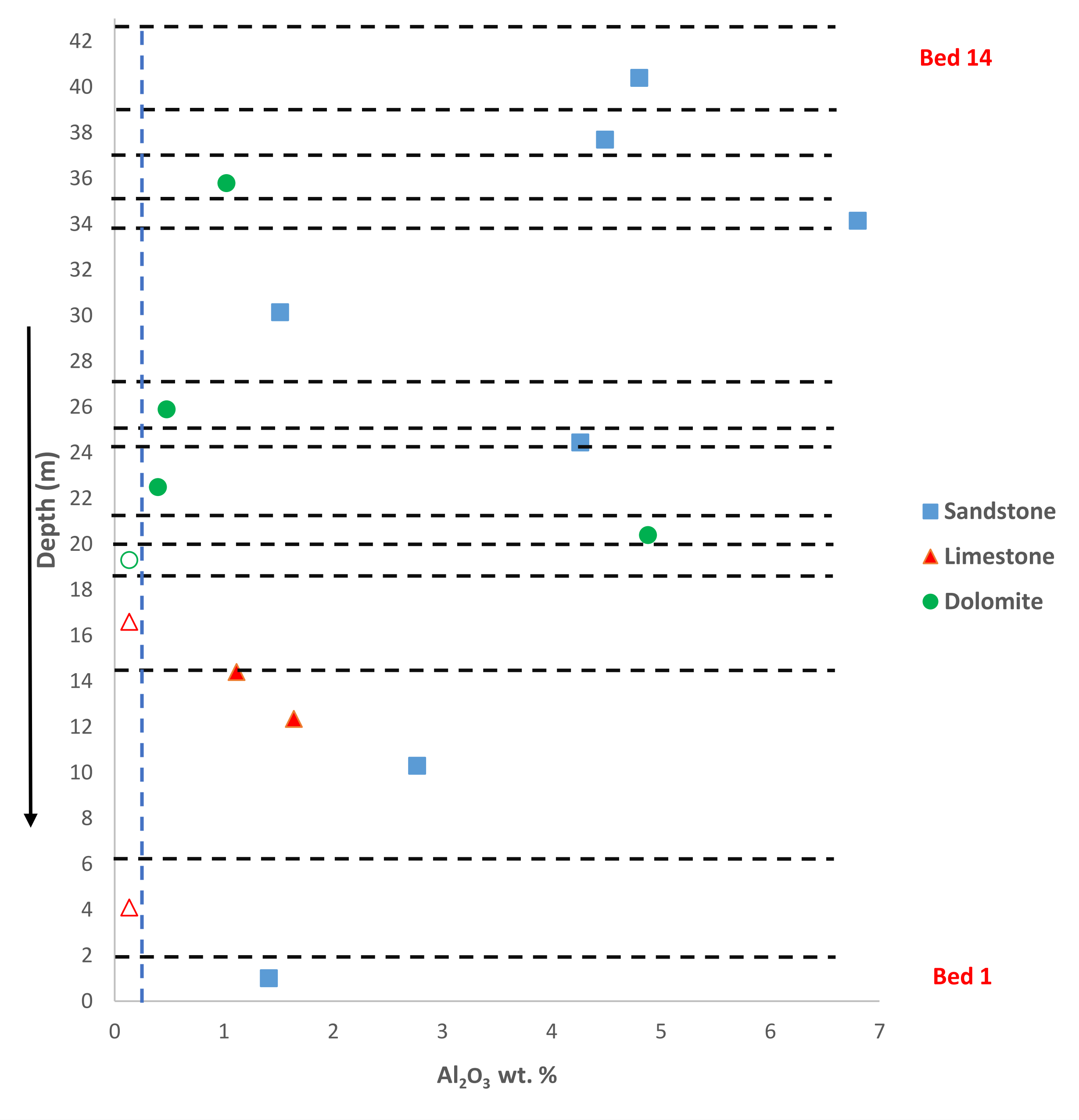

Figure 3-61. Al_2O_3 weight % versus depth. The red triangular with white core data points are limestone samples in which Al_2O_3 is below detection; they are plotted at half the detection limit. The green with white core circular data point is a dolomite sample in which Al_2O_3 is below detection; it is plotted at half the detection limit. The blue dashed line on the plot shows the detection limits. The black dashed lines represent bed contacts.

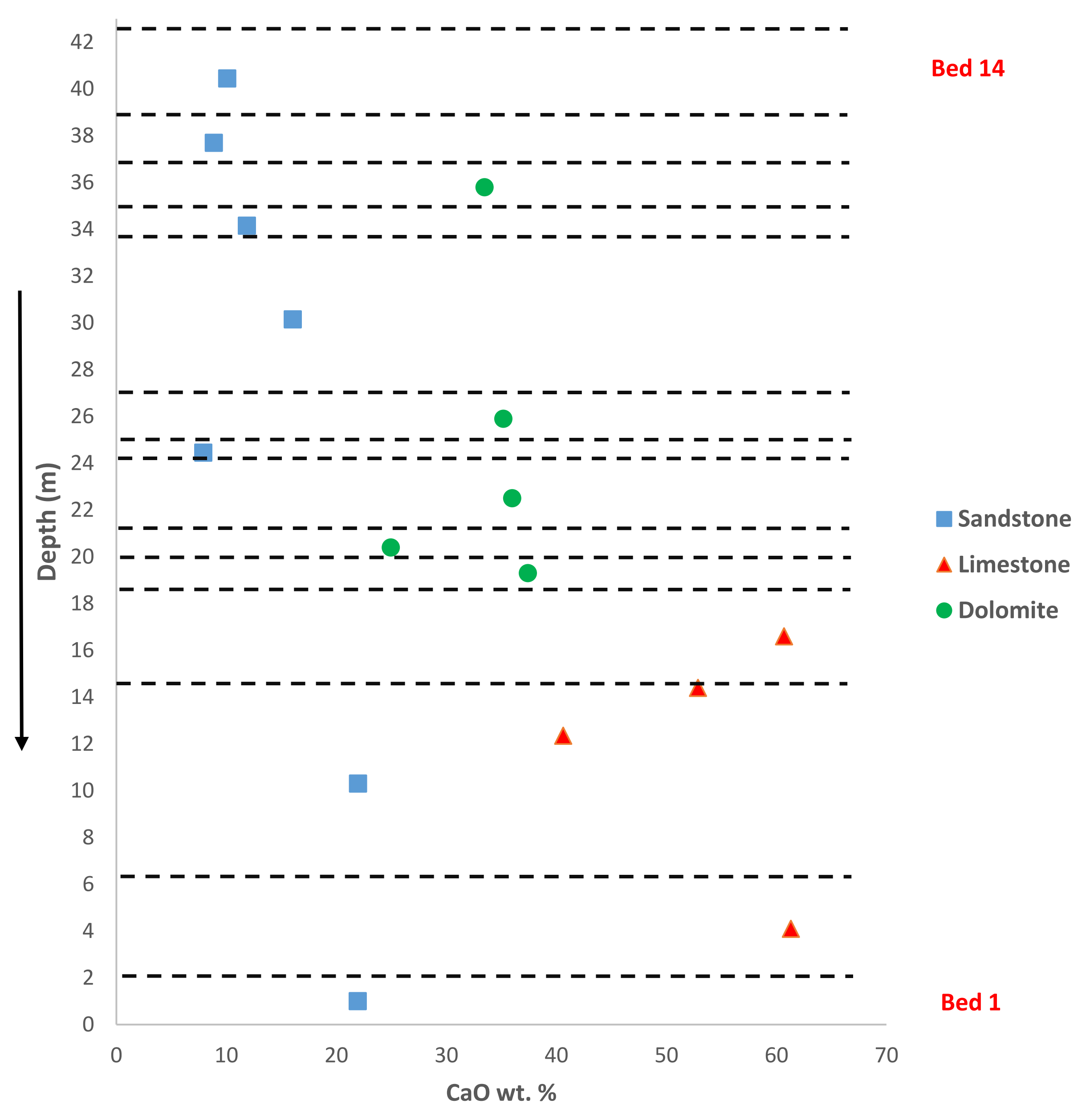

Figure 3-62. CaO weight % versus depth. The black dashed lines represent bed contacts.

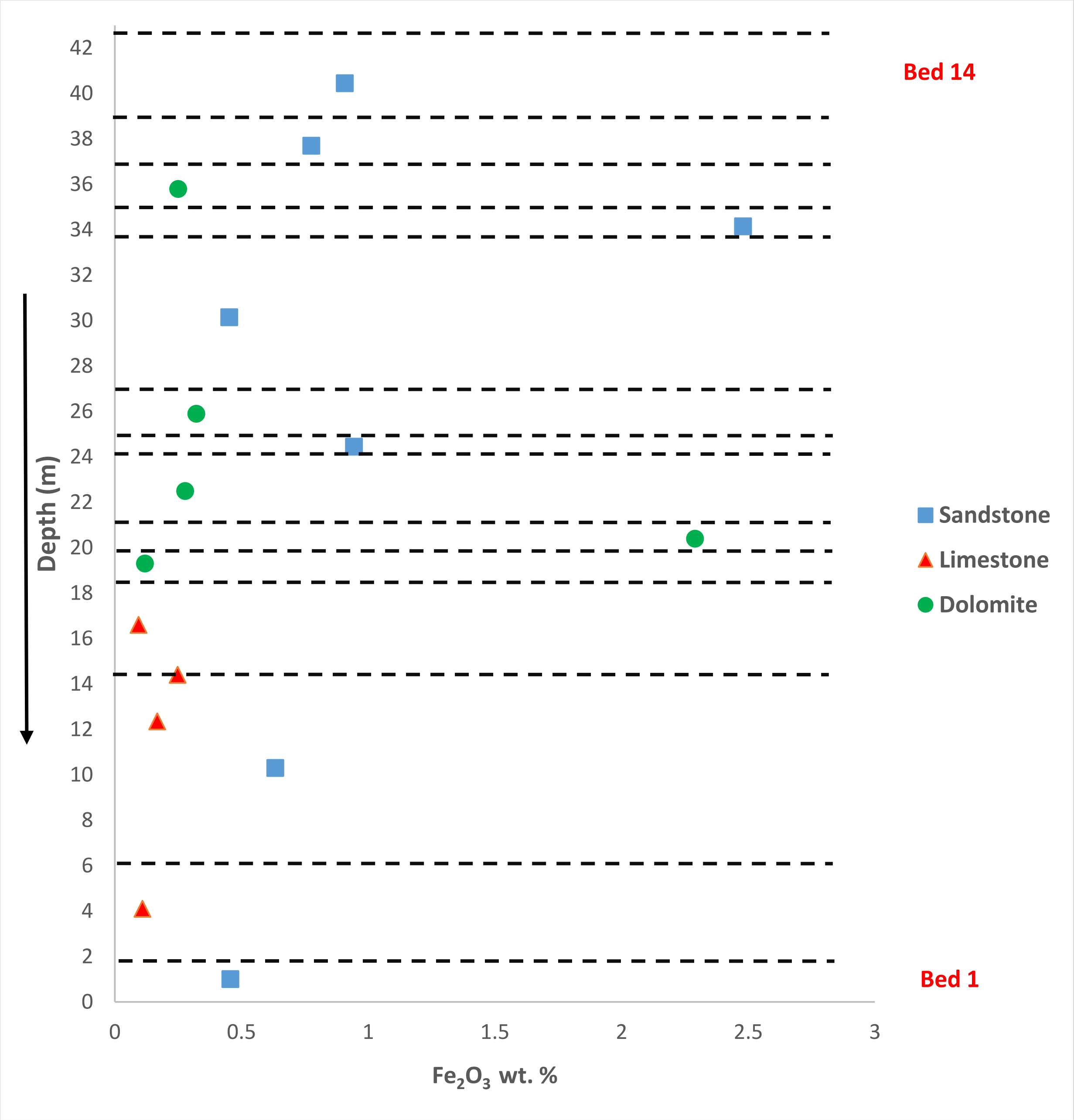

Figure 3-63. Fe_2O_3 weight % versus depth. The black dashed lines represent bed contacts.

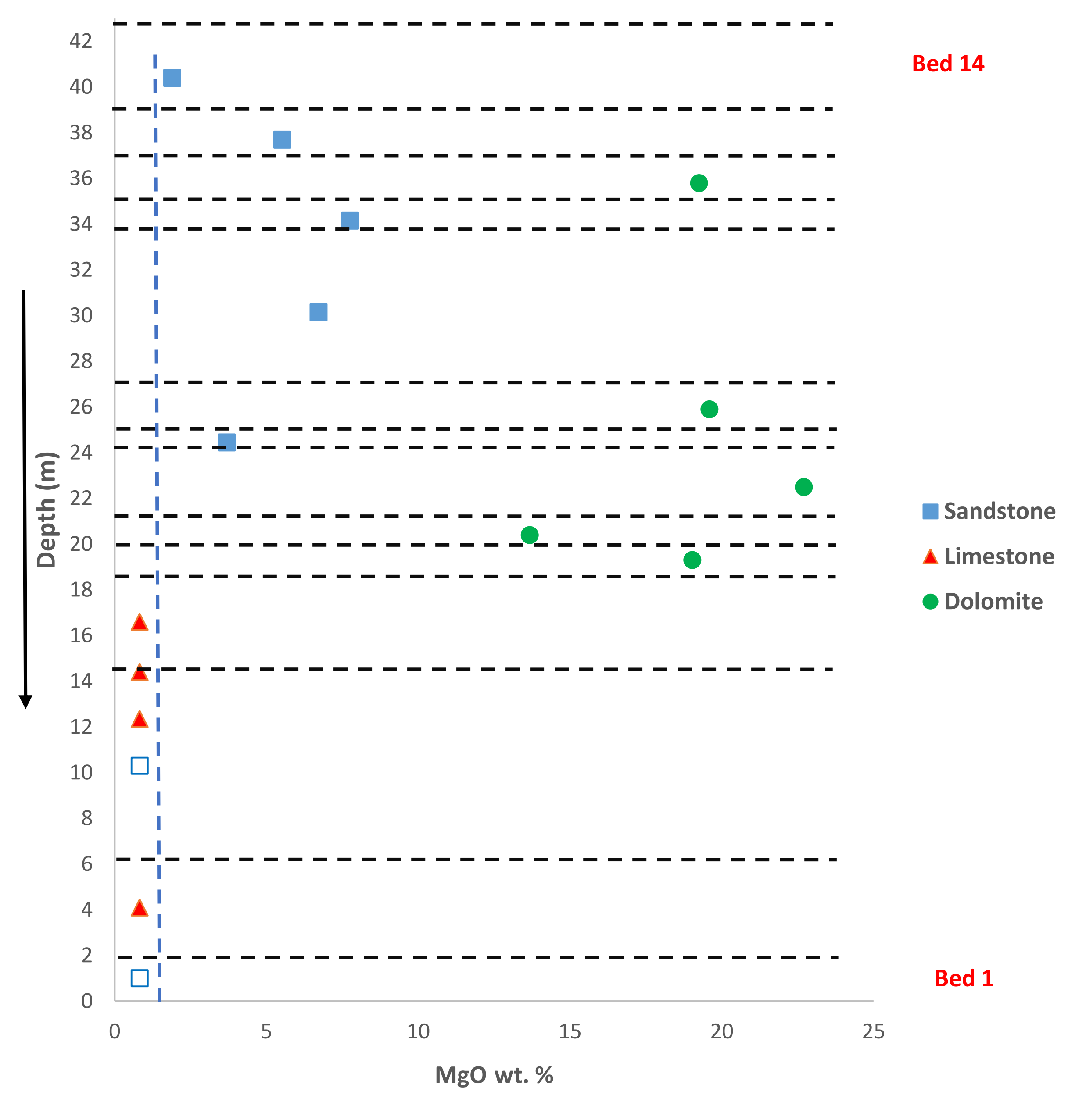

Figure 3-64. MgO weight % versus depth. The blue with white core square data points are sandstone samples in which MgO is below detection; they are plotted at half the detection limit. All limestone samples show MgO below detection. The blue dashed line on the plot shows the detection limits. The black dashed lines represent bed contacts.

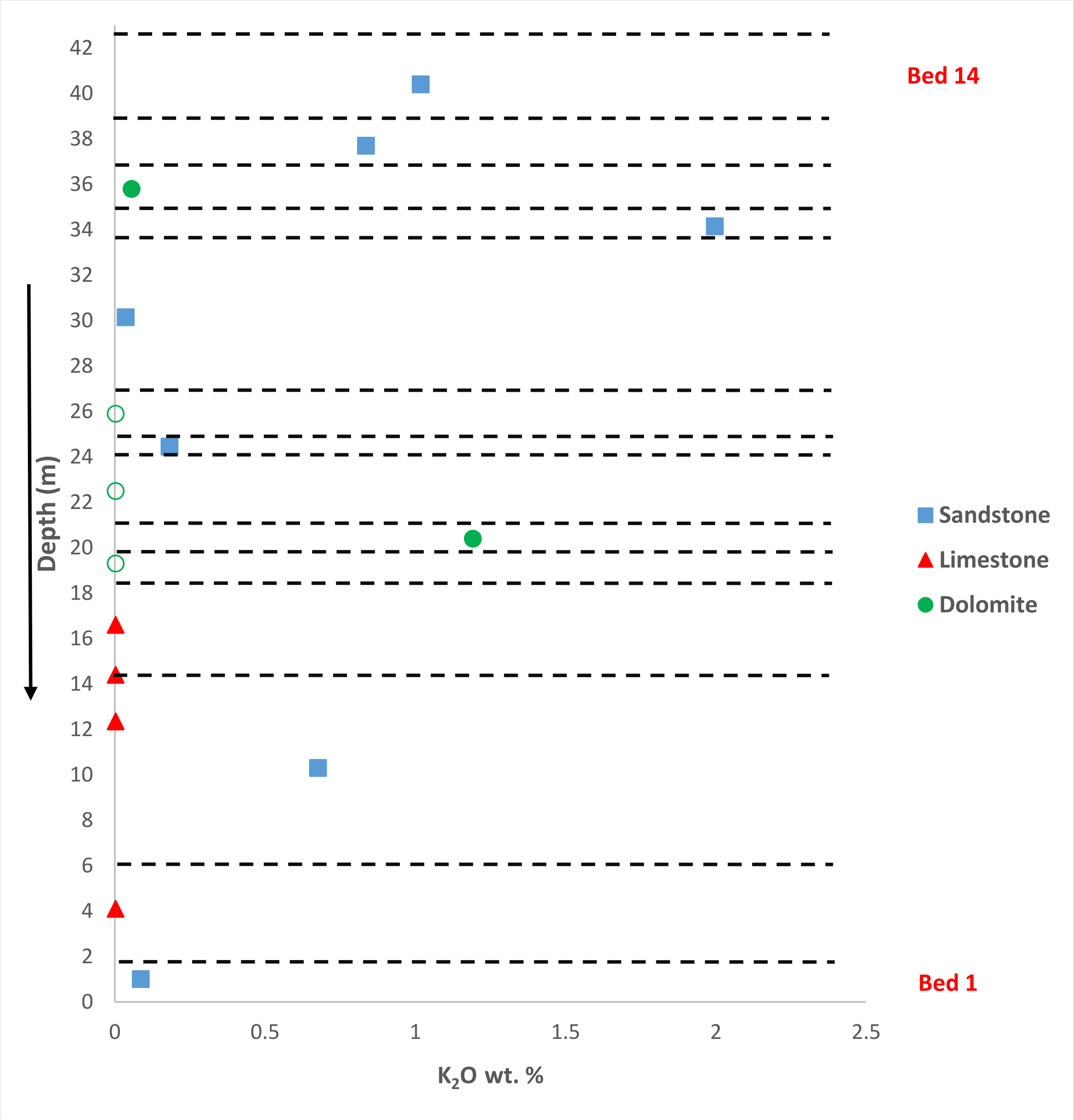

Figure 3-65. K_2O weight % versus depth. All limestone samples are below detection (red data points plotted at half the detection limit). The green with white core circular data points are dolomite samples in which K_2O is below detection; they are plotted at half the detection limit. The black dashed lines represent bed contacts.

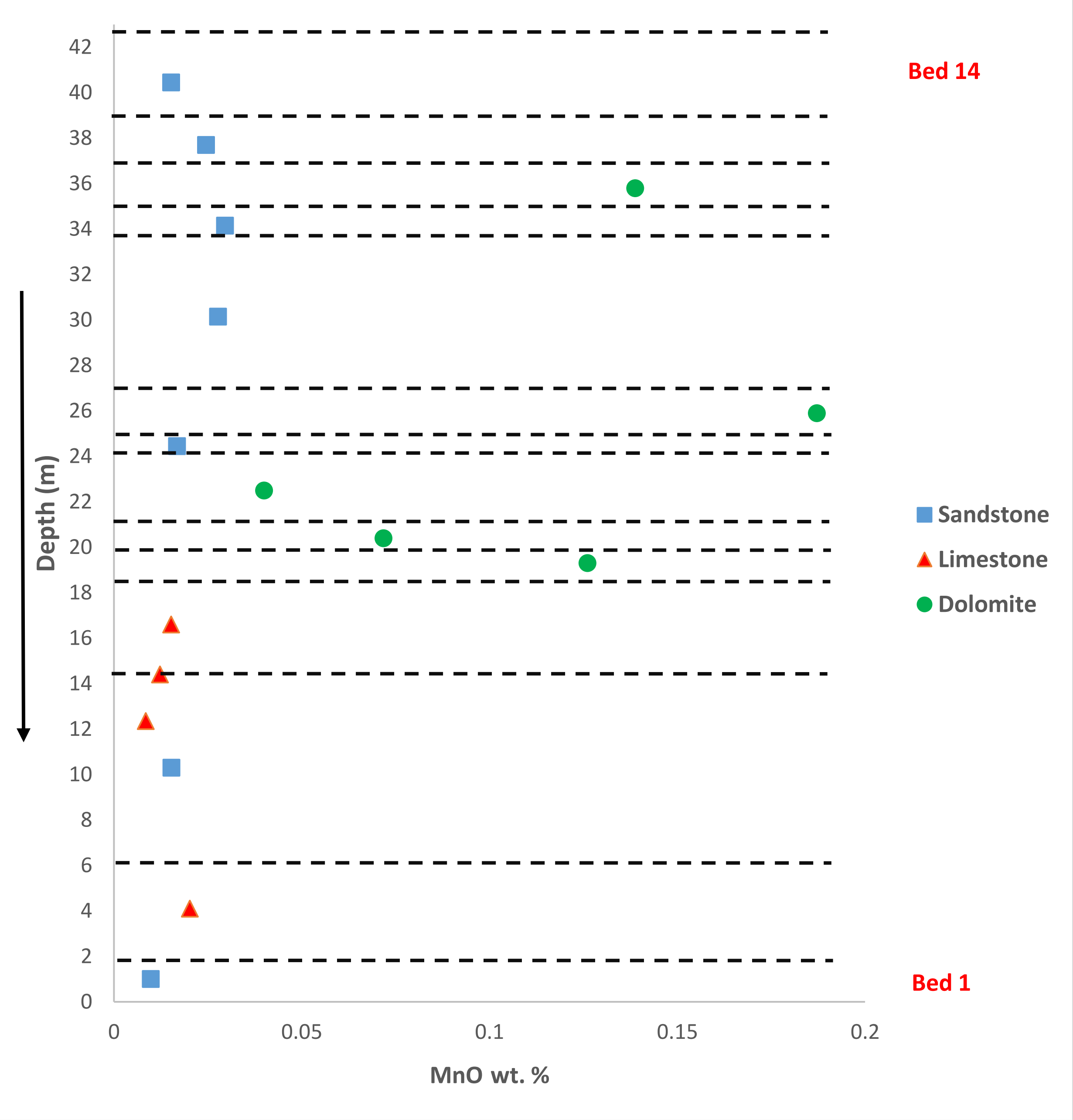

Figure 3-66. MnO weight % versus depth. The black dashed lines represent bed contacts.

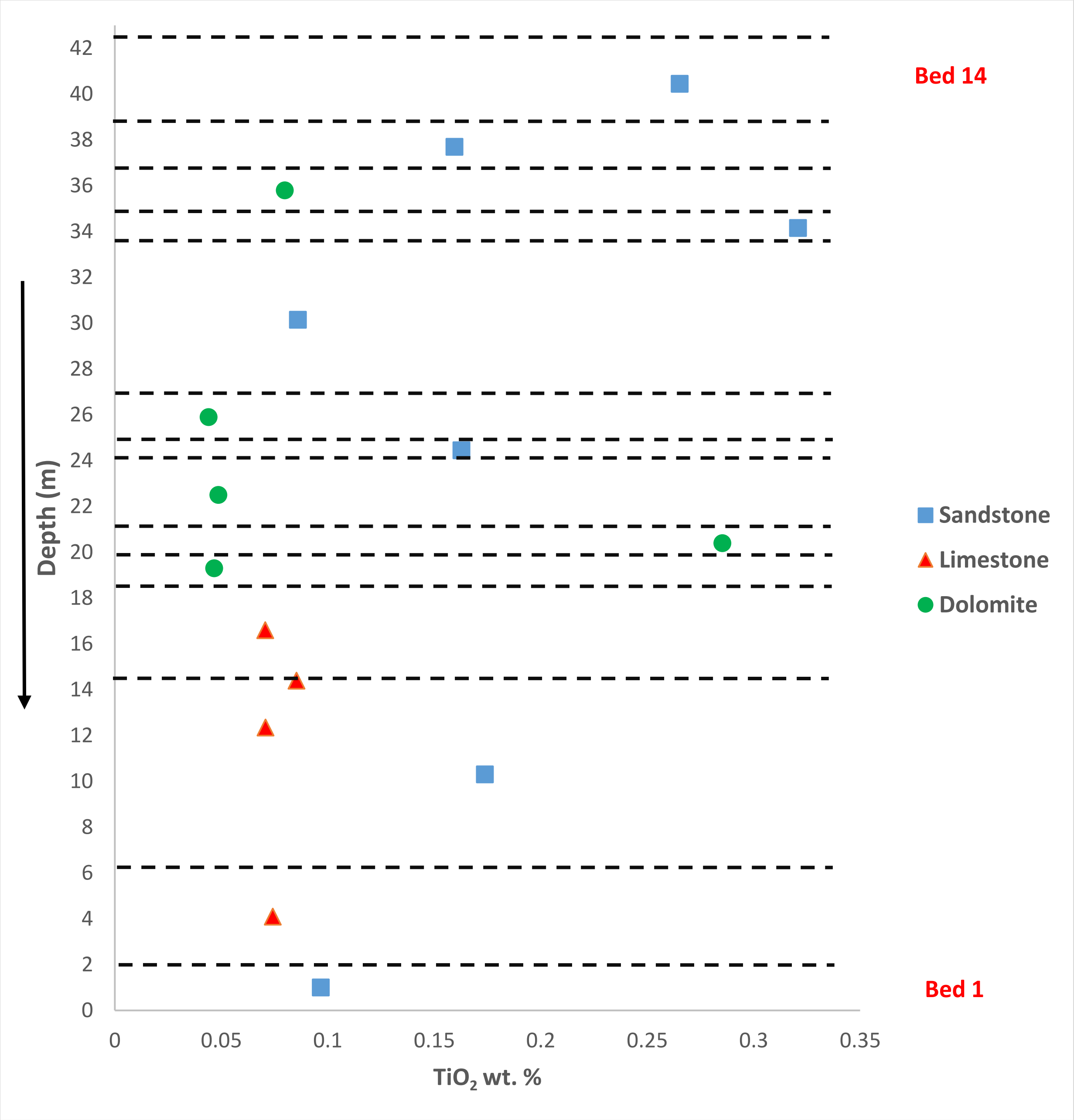

Figure 3-67. TiO_2 weight % versus depth. The black dashed lines represent bed contacts.

The cross-plot of SiO_2 versus Al_2O_3 is used to investigate the importance of clays within the sandstone. In sandstone samples there is not a clear relationship between SiO_2 and Al_2O_3. Most carbonate samples are low in both SiO_2 and Al_2O_3, but samples with higher SiO_2 concentrations tend to also be higher in Al_2O_3. (Fig. 3-68).

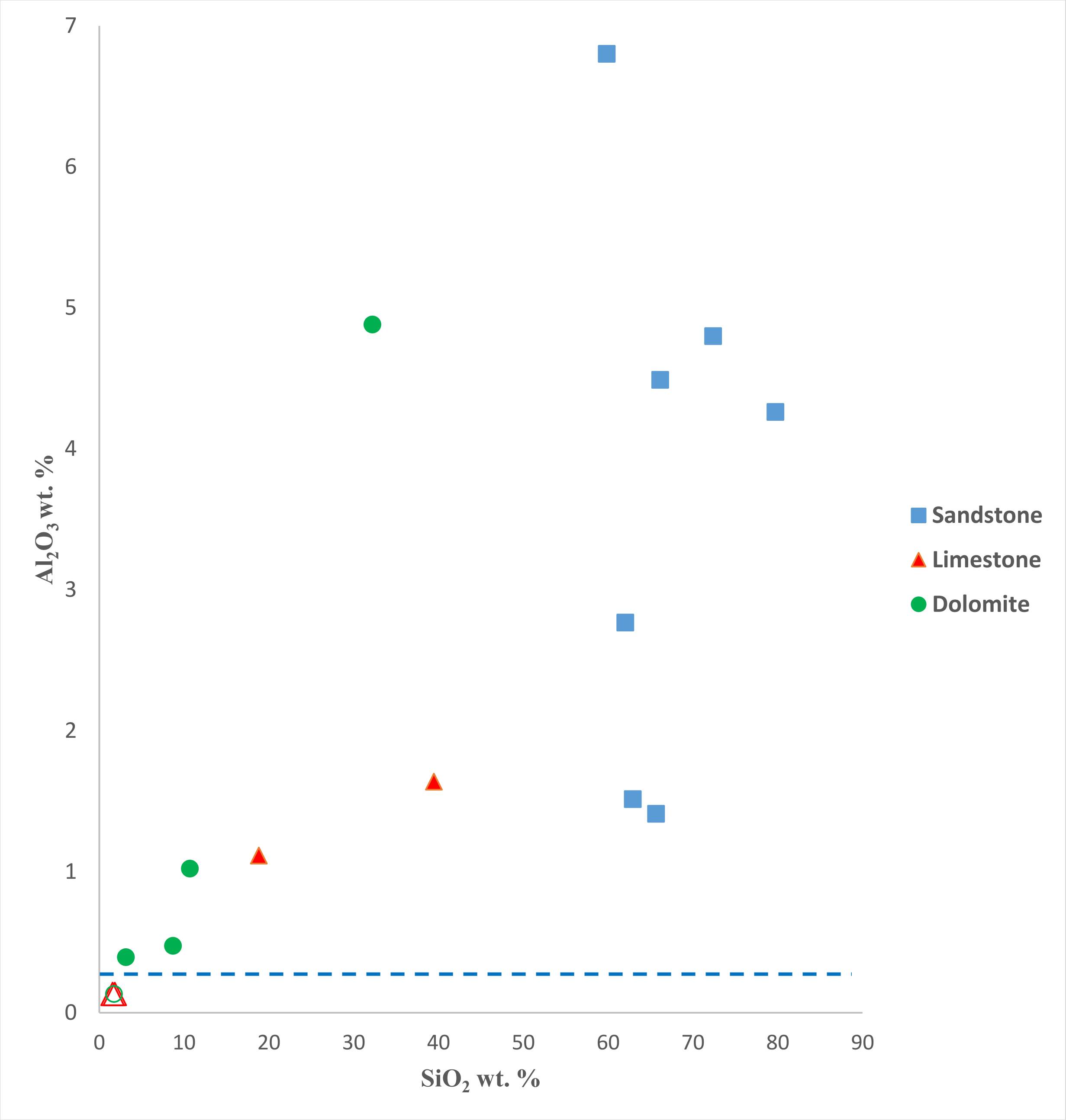

Figure 3-68. Cross-plot of weight % SiO_2 versus weight % Al_2O_3. The red with white core triangular data points are limestone samples that have Al_2O_3 below detection and are plotted at half the detection limit. The green with white core circular data point is a dolomite sample in which Al_2O_3 is below detection; it is plotted at half the detection limit. The blue dashed line on the plot shows the detection limits.

Sr has been plotted against CaO (Fig. 3.69) to see whether there is a relationship between the two elements in any lithology. The concentration of Sr is somewhat higher in limestone samples than in dolomite samples. Neither the individual lithologies, nor the overall data set show any apparent correlation between Sr and Ca.

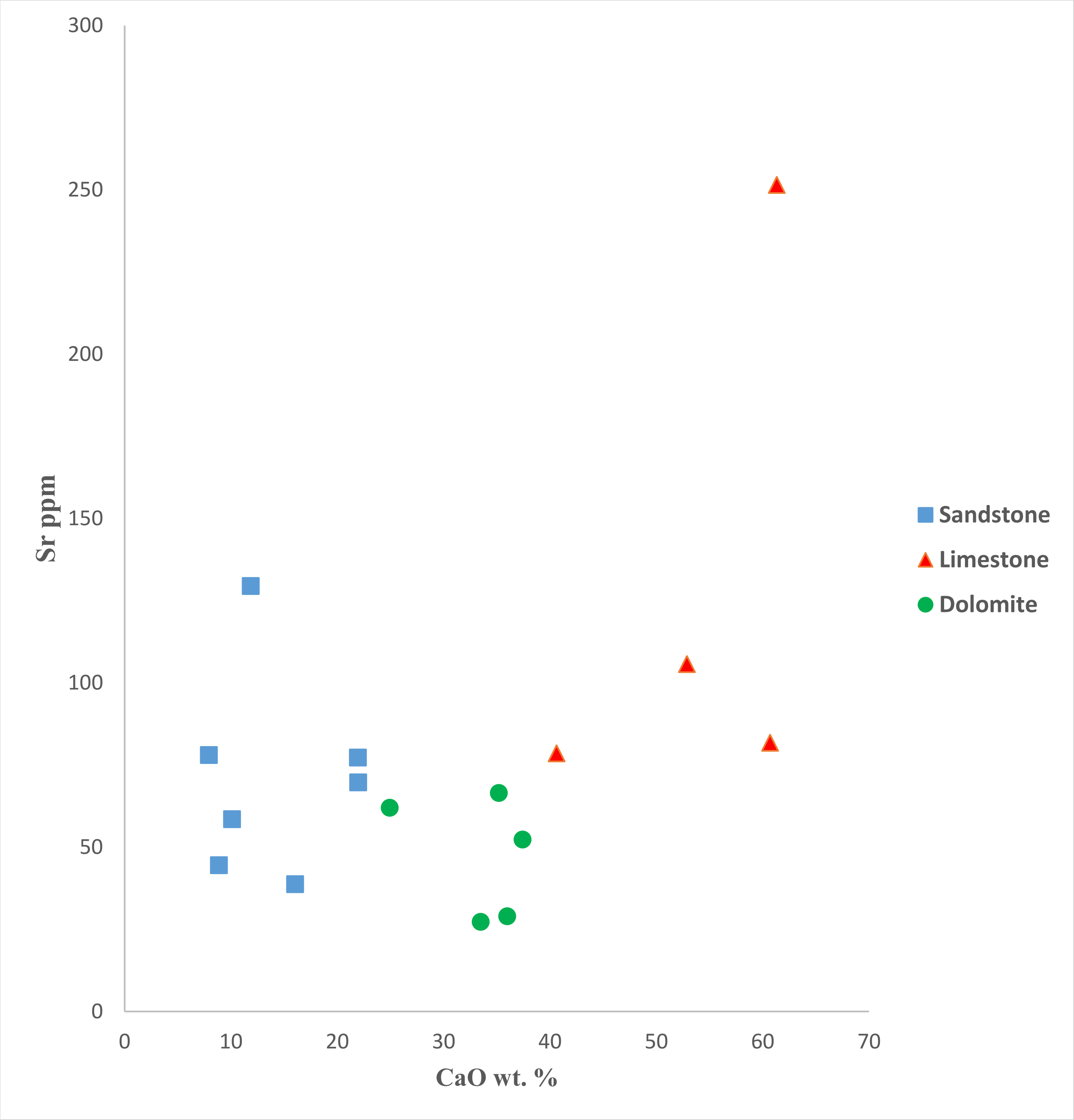

Figure 3-69. Cross-plot of CaO weight % versus Sr.

The concentration of S is below detection in the stratigraphically lower samples, detectable in the middle of the section, and a mix of not detectable and detectable in stratigraphically higher samples (Fig. 3.70). The S values are relatively high in some sandstone and dolomite samples, but below detection in others and below detection in all limestone samples. In sandstone the values range from 176 ppm to 1013 ppm, whereas in dolomite they range from 224 ppm to 802 ppm.

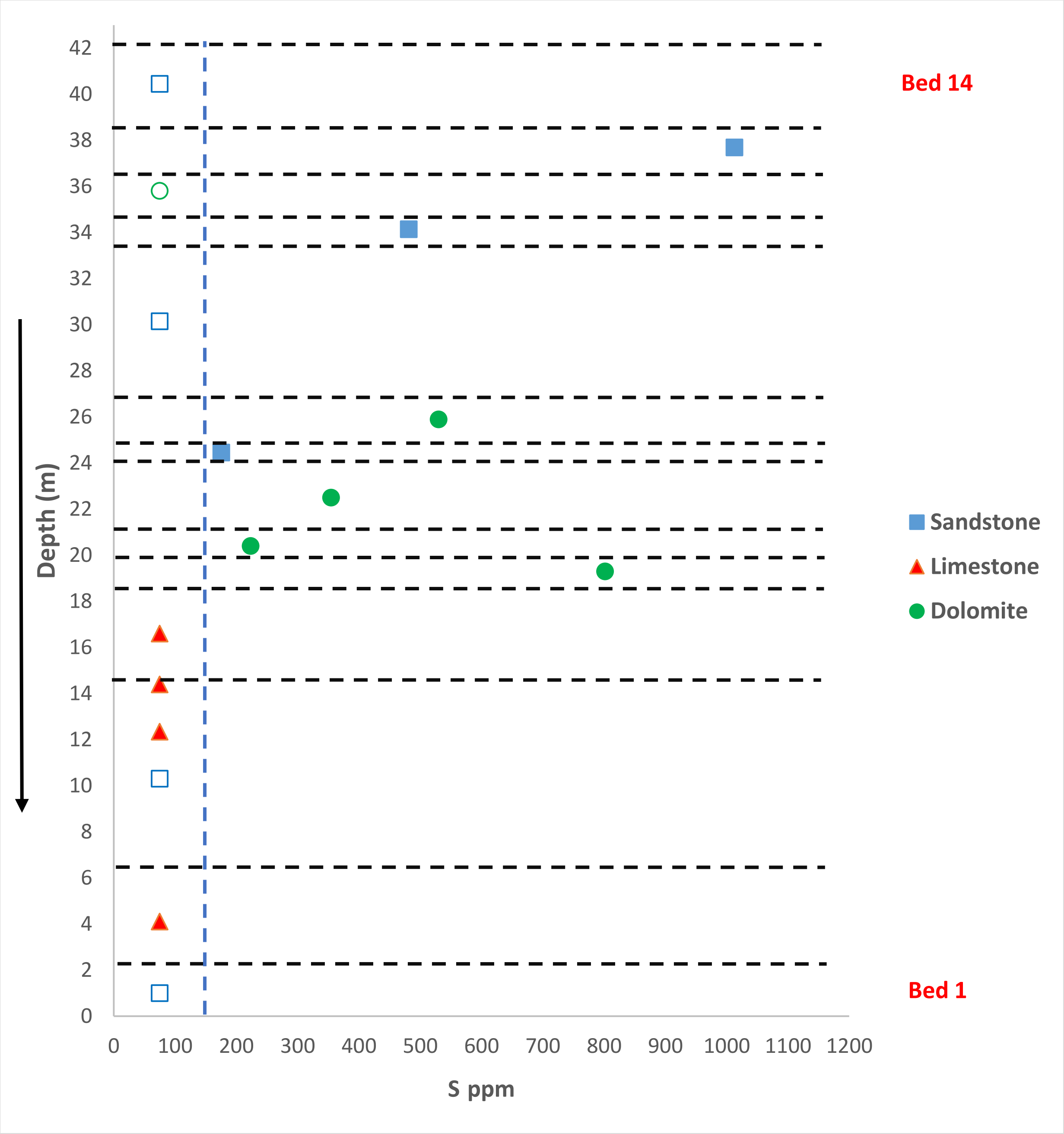

Figure 3-70. Plot of S versus Depth. The blue with white core square data points are sandstone samples that have S content below detection and are plotted at half the detection limit. The green with white core circular data point is a dolomite sample that has S concentration below detection and plotted at half the detection limit. All limestone samples (red data points) are below detection and is plotted at half of the detection limit. The blue dashed line on the plot shows the detection limits. The black dashed lines represent bed contacts.

A cross-plot of MgO versus S (Fig. 3.71) was used to see if there is a relationship between Mg and S. Note that Mg and S are below detection in the lower part of the outcrop and above the detection limits in the middle and upper part of the outcrop. The cross-plot shows that four out of five dolomite samples have detectable S concentration.

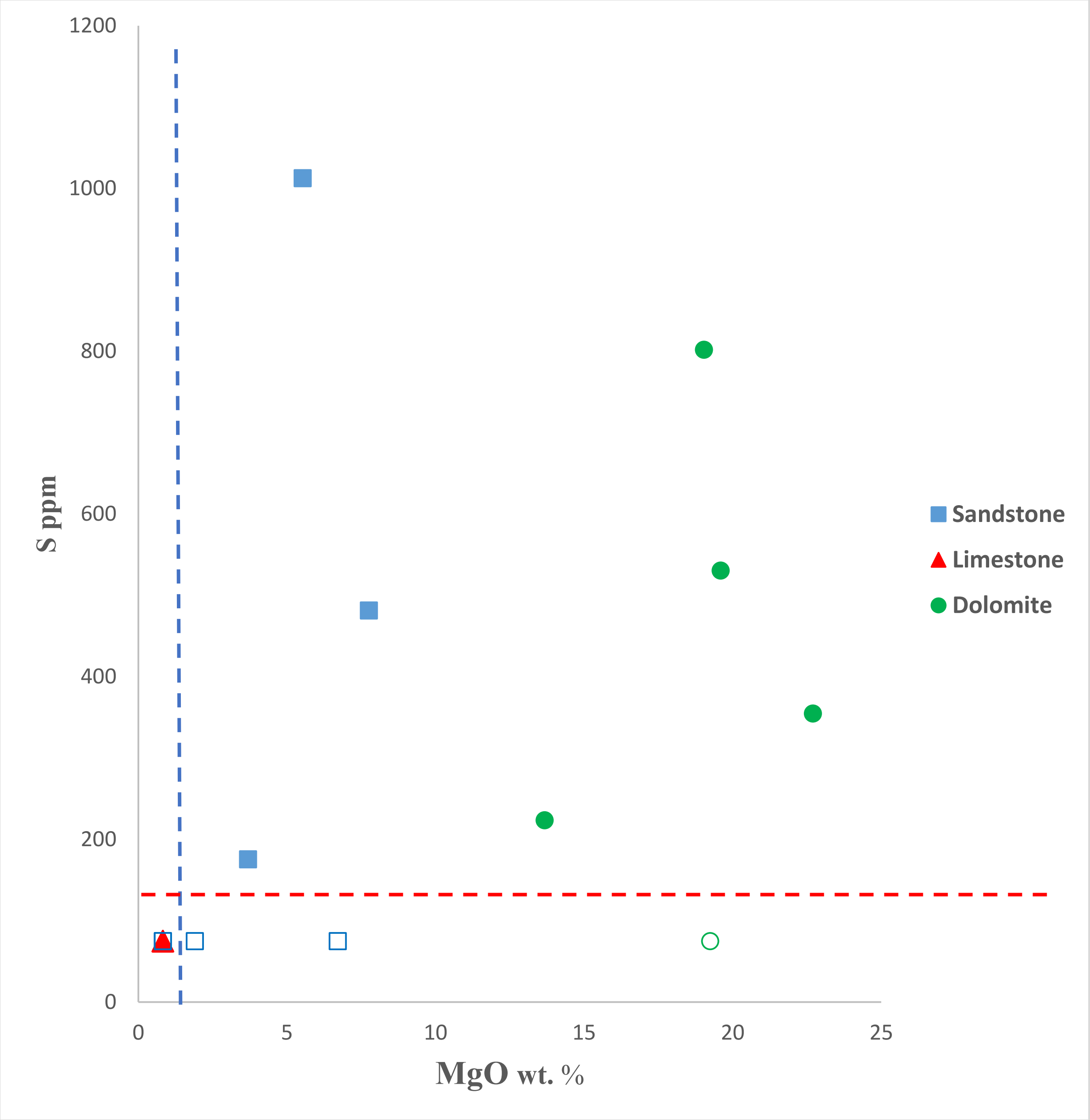

Figure 3-71. Plot of MgO weight % versus S. The blue with white core square data points are sandstone samples that have S content below detection and are plotted at half the detection limit. The green with white core circular data point is a dolomite sample that has S concentration below detection and is plotted at half the detection limit. The limestone samples (red data points) have both S and MgO concentration below detection and are plotted at the half of the detection limit. The dashed lines on the plot show the detection limits.

A cross-plot of K_2O versus Al_2O_3 (Fig. 3.72), in sandstone samples shows a positive relationship between K_2O and Al_2O_3 contents, whereas the carbonate samples are low in both elements. K and Al might be expected to show correlation if the dominant minerals hosting Al are K-spar, micas, and (or) illite, but not if the Al is mainly in plagioclase or clays other than illite. The plot shows a positive correlation between Al and K for sandstone samples exceeding 2% Al_2O_3, but not for sandstones below 2% Al_2O_3 or for carbonates.

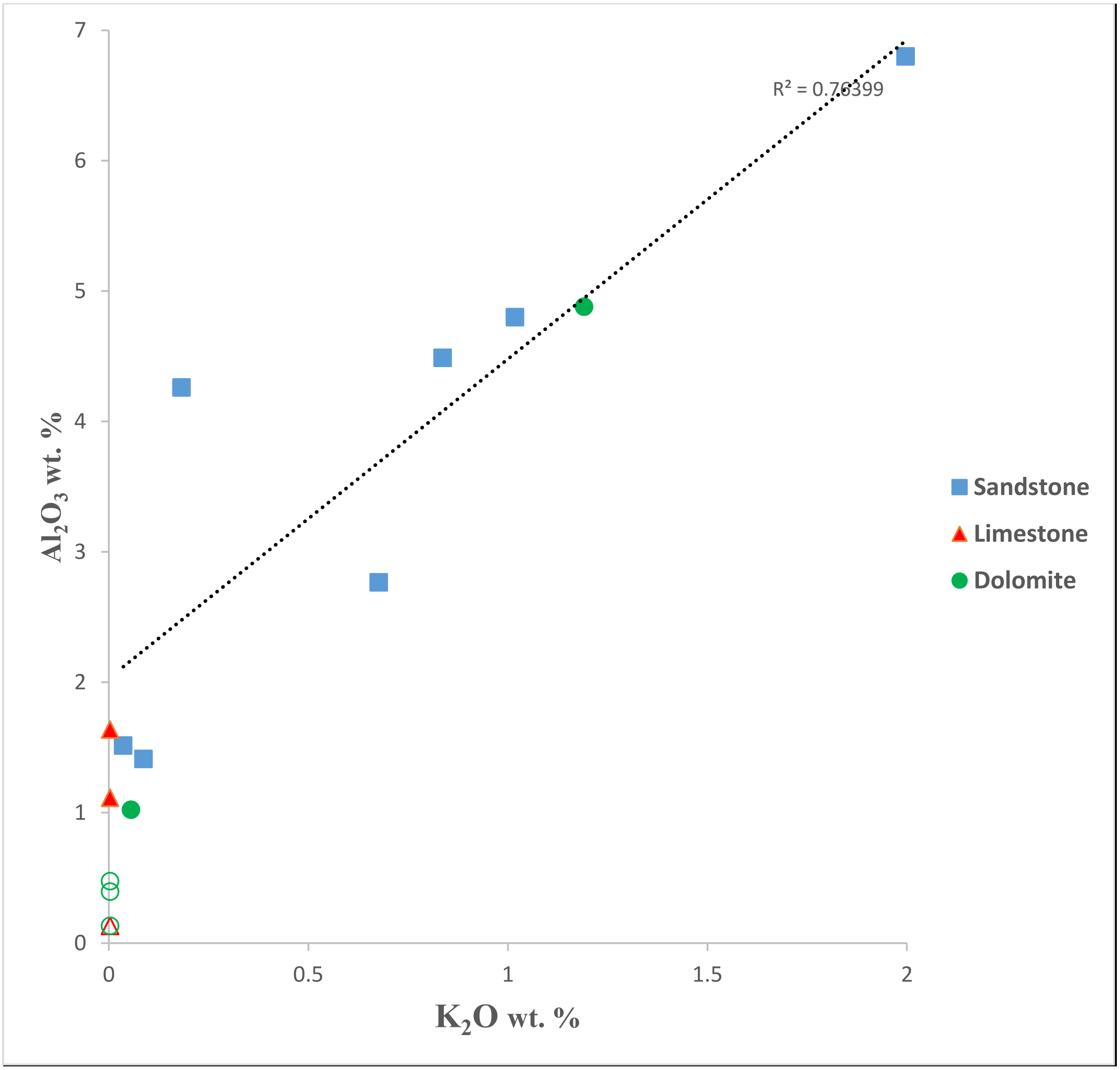

Figure 3-72. K_2O weight % versus Al_2O_3 weight %. The green with white core circular data points are dolomite samples that show K_2O concentration below detection and are plotted at half of the detection limit. One dolomite sample (green circle with white core) shows Al_2O_3 concentration below detection and is plotted at half of the detection limit. All limestone samples (red triangle) show K_2O concentration below detection and two samples show Al_2O_3 below detection and are plotted at the half of the detection limit.

Rb is higher in sandstone samples, varying from 8.5 ppm to 58 ppm, than in carbonate samples, where it varies from below detection to 3.5 ppm. The content of V in sandstones varies from below detection to 166 ppm and from below detection to 114 ppm in the carbonate samples. The concentration of Cr ranges between below detection and 48 ppm in sandstone, and from below detection to 76 ppm in carbonate samples. The Cu values range from 7 ppm to 28 ppm in sandstone, and from below detection to 12 ppm in carbonate. The Zr values are generally higher in the sandstones at 68 ppm to 201 ppm than in carbonates that range from below detection to 77 ppm. The Pb concentration ranges from 5 ppm to 9 ppm in sandstone, and from below detection to 6 ppm in carbonate. The Zn concentration ranges from 7.5 ppm to 19 ppm in sandstone, and from 4.5 ppm to 28 ppm in carbonate. Finally, there are some elements for which most values are below the detection limit, including Ni and Y. One sample each of sandstone, limestone and dolomite contain Ni values above detection. The Y concentration is above detection in three sandstone samples and one dolomite sample (Table 3.4).

CHAPTER 4
DISCUSSION

4.1 Ingleside Outcrop

Several features observed in both outcrop and thin section, including calcite veins, carbonate-hosted vugs, and carbonate cement, suggest carbonate mobility throughout the outcrop during diagenesis. The presence of stylolites suggests that pressure solution of carbonates (limestone and dolomite) is one possible source of carbonate that could have reprecipitated in veins or as cement (Fredrickson, 1978). The fact that the stylolites are approximately parallel to bedding and not perpendicular suggests that they formed during and contributed to compaction and were not formed during later tectonic activity. This likely early timing of stylolite development suggests availability of cement-forming carbonate early in burial diagenesis.

4.2 Petrography

There are some petrographic findings in this thesis that are similar to those of Fredrickson (1978), but with some differences. One difference is that she observed dolomite cement in only one out of 27 samples. Fredrickson (1978) used alizarin red stain to distinguish between calcite and dolomite, so is unlikely to have misidentified dolomite as calcite. In the present study, which also used alizarin red stain, both dolomite and calcite cement were observed in all samples, although dolomite was uncommon in the deepest samples. Another difference is that Fredrickson's sandstone samples were stained to recognize feldspar. This technique may have helped her accurately recognize feldspar, and to classify the sandstones mostly as subarkose. On the other hand, the thin sections in this thesis were not stained for feldspar and some untwinned feldspar may not have been recognized, and most of the sandstones in my thesis are classified as quartz arenite. Further, she observed illite, smectite, and kaolinite in her samples, and only one sample contains a small amount of mixed layer smectite-illite. Fredrickson (1978) used x-ray diffraction to analyze clay minerals. Therefore, she was able to report more types of the clay minerals. However, in my study only kaolinite was recognized in the thin sections, and x-ray diffraction analysis was not used; therefore, some clay minerals possibly were not recognized in the thin sections.

Fredrickson (1978) observed quartz grains content generally increasing up-section, whereas in this study no trend in quartz content was observed. This may be because in the present study some untwinned feldspar was classified as quartz and that concealed the trend. She also reported quartzite, igneous, and carbonate rock fragments in the thin sections. Carbonate grains are composed of skeletal fragments, peloids, and minor oolites. In my study, only carbonate and sandy siltstone rock fragments were observed in thin sections. Fredrickson reports hematite is present in small amounts as detrital grains, an observation not made in my study.

There are some similarities in diagenetic processes and observations between the present study and previous studies on sandstone diagenesis. One of the similarities is that Fredrickson (1978) observed that hematite cement rimmed the grains in the Fountain Formation and Ingleside Formation in the Owl Canyon area, Colorado. Rainoldi et al. (2015) also noted that hematite cement coated framework grains and was precipitated in early diagenesis in a Late Cretaceous sandstone from the Neuquén Basin, Argentina. Rainoldi et al. (2015) also stated that silica overgrowths overlie hematite cement, so formed after the precipitation of hematite cement. In my study the hematite cement coated grains and occurred on interpenetrating boundaries between compacted grains and therefore is interpreted as occurring in early diagenesis prior to compaction. Also, quartz cement overlies the hematite cement and is interpreted to have been precipitated after the hematite cement precipitation.

Another similarity is with the suggestion of Imam and Shaw (1987) that poikilotopic cement formed in early diagenesis, which they observed in sandstone in the Surma Group from the Bengal Basin. They reported that where poikilotopic Fe-calcite cement is present, the grains have limited contacts, and in some samples the grains appear to float in the poikilotopic cement, and consequently conclude that the poikilotopic cement precipitated in very early diagenesis. Rahman et al. (2011) observed that framework grains surrounded by poikilotopic carbonate cement were not affected much by compaction, and that the poikilotopic cement precipitated before quartz cementation. In addition, the poikilotopic cement occurred between loosely packed grains and filled pores, indicating it was precipitated early within the samples. In my study poikilotopic cement precipitated between grains that were not strongly compacted and the grains within the poikilotopic cement are coated with hematite cement. Consequently, the poikilotopic cement is interpreted to be precipitated early in diagenesis, but after the precipitation of the hematite cement.

An additional similarity between my study and others is the abundance of carbonate cement, which Worden and Burley (2003) stated is one of the most abundant cements in sandstone. Dissolution along stylolites in carbonates is another possible source for calcite cement (Land and Dutton, 1978; Bjørlykke, 2010). In my study stylolites were observed in carbonate and were probably one source of carbonate that reprecipitated in veins or as cement. Boggs (2009) suggested that the dissolution of Ca-feldspar is a possible source of calcium to form calcite cement. In my study no Ca-feldspar was recognized and there is no evidence that there was ever much Ca-feldspar present in the section, although its presence, followed by complete destruction, cannot be ruled out.

According to McBride (1989) silica cement is precipitated mainly at burial depths between 1 to 2 km and at temperature range of 40-90°C, and could precipitate at a burial depth of 4 km or even 6 km. Bjorlykke and Egeberg (1993) suggested that quartz cementation is favored by deep burial. In sandstones from the rapidly subsiding North Sea Basin, they found from fluid inclusion analysis that most quartz cement formed at temperatures above 90 -100°C and probably continued precipitating slowly after petroleum emplacement, but they also suggest that quartz cement in other settings can form at 70-80°C. Worden and Burley (2003) stated that commonly quartz cementation in sandstone forms at temperature ranging between 80 –100°C. Rahman et al., (2011) observed that quartz cement in sandstone samples from the Surma Group in the Bengal Basin is more abundant in deeply buried sandstones and is rare in sandstones from shallower depths. They observed quartz cement in sandstone from depths between 2000 and 3400 m. These studies considered together with the fact that the Denver-Julesburg Basin was probably not rapidly subsiding when this Ingleside locality was undergoing burial diagenesis, suggest that quartz cement likely formed at depths well over 1 km and temperatures above 60°C. This suggests that in my study the quartz overgrowths are not only later than the hematite cement, but probably formed after the main stage of compaction, and hence after pokilotopic carbonate cement.

Alteration of feldspar during diagenesis has been reported in numerous studies. Land and Dutton (1978) reported that some feldspar grains were partially or completely replaced by calcite. Some cements precipitated in secondary porosity suggesting that these cements precipitated in late stage after the dissolution of the feldspar. Also, feldspar destruction occurred as temperature increased with burial depth. Land and Milliken (1981) observed that feldspar alteration was an important process and has an impact on the precipitation of silica and carbonate cements, and on the formation of the secondary porosity in the sandstone of the Frio Formation, Texas Gulf Coast. They also observed that K-feldspar decreased with depth and below 4,267 m much K-feldspar was dissolved or albitized. Milliken et al. (1994) described that the dissolution and albitization of K-feldspar in samples from burial depth between 0.9-4.3 km in sandstones of the Frio Formation, South Texas, caused a loss of about 2 wt. % of K_2O in sandstone. Wilkinson et al. (2001) concluded that the amount of K-feldspar decreased with burial depth in two different rift basins in the North Sea and the passive margin basin of the USA Gulf Coast. K-feldspar destruction at a burial depth from about 1.5 to 4.5 km reduced the rock volume by about 15%, and arkosic sandstones turned into quartz arenite sandstones as secondary porosity increased due to the destruction of K-feldspar. In the present study some of the feldspar was partially altered to calcite and dolomite, indicating diagenetic feldspar replacement occurred. Also, some feldspar partly dissolved, creating secondary porosity. Observations in this study do not establish the relationship between feldspar alteration and increasing depth, but based on other these other studies it likely occurred sometime in the middle to later stages of burial diagenesis.

Land and Dutton (1978) stated that kaolinite cementation formed by as a result of H^+ released during replacement of detrital feldspar in the Gray sandstone in the West Tuscola Field, Texas. Imam and Shaw (1987) observed that authigenic kaolinite cement precipitated in pore spaces and formed as a result of feldspar alteration. They also suggested that the formation of kaolinite cement is favored by the presence of acidic pore fluids, with feldspar as the source of Al and Si to form this cement. Worden and Burley (2003) suggested that kaolinite precipitation requires low ionic strength water and low pH, that can be provided by weathering. Also, kaolinite cement fills pore spaces, and is formed by feldspar replacement and alteration. Islam (2009) observed that feldspar alteration was responsible for some kaolinite cement. Taylor et al. (2010) described that kaolinite cement precipitated in pore spaces as authigenic cement caused by feldspar dissolution. In my study kaolinite cement precipitated in pore space, and may be concurrent with feldspar dissolution which might be the source for Al and Si in the kaolinite cement. The fact that low pH favors kaolinite precipitation suggests the possibility that organic acids associated with hydrocarbons may have favored diagenetic precipitation of kaolinite in the Ingleside. However, some of the feldspar replacement by kaolinite may have occurred during modern weathering rather than during diagenesis.

The saddle dolomite which was observed in sample ING-15 in bed 9 (Fig. 3.44), suggests that there was a late stage of dolomitization that affected the outcrop. The trace amount of glauconite observed might be reworked detrital material, rather than an indicator of the depositional environment.

4.3 Geochemistry

Considering the petrographic findings and the geochemical data together, it is possible to relate most of the geochemical findings to the mineralogical observations. The CaO in sandstone samples is related to calcite and dolomite cement, whereas the MgO is related almost entirely to dolomite cement. The Fe_2O_3 in sandstone samples is probably mainly in hematite cement within the sandstone. Furthermore, the low concentration of K_2O in sandstone samples could be attributed to the low proportion of K-feldspar and other K-rich minerals. The original sediment deposited may have been richer in K-feldspar and its partial destruction during diagenesis may have contributed to loss of K (Fig. 3.33).

The cross-plot of weight % SiO_2 versus weight % Al_2O_3 (Fig. 3.68) shows no clear relationship between SiO_2 and Al_2O_3 content in sandstone. Petrographic analysis shows only modest amounts of Al-containing minerals, including feldspar, mica, glauconite and kaolinite. These petrographic findings, along with the abundance of quartz, suggest that no strong relationship should be expected between Al and Si.

S and Mg concentrations may be related to one another. S is below detection in the lower part of the outcrop. S is detectable in the middle and upper part of the outcrop. The concentration of MgO is also below detection in the lower part of the outcrop, and detectable in all samples in the middle and upper part of the outcrop (Fig. 3-64). Four out of five dolomite samples contain detectable S, as do three out of five sandstone samples (Fig. 3.70). This interesting stratigraphic similarity in S and MgO concentrations, may indicate that MgO and S were added by diagenetic fluids that moved through the middle and upper part of the outcrop, but not the lower part. There is, however, no clear correlation between the concentrations of the two elements (Fig. 3.71). The mineral host of the S is uncertain; neither anhydrite nor gypsum were recognized in thin section, but small amounts may have been overlooked. The highest S content is approximately 1000 ppm in GS-13 from bed 13, and if all of the S were in gypsum it would be 0.53% of the sample, and if all of the S were in anhydrite it would be 0.42% of the sample.

K_2O correlates positively (r^2=0.76) to Al_2O_3 in the sandstone samples (Fig. 3.72), probably because the Al_2O_3 is mostly in illite, micas, feldspar, or glauconite that also have K in them. In the sandstone samples below 2% Al_2O_3 there is very little K_2O, indicating that in these samples Al is probably in kaolinite. There is one sample classified as dolomite that plots with the relatively K- and Al-rich sandstones and also has unusually high SiO_2 (32 wt. %) for a carbonate rock. It likely has a substantial sand grain content that includes some feldspar.

4.4 Limitations of the XRF Data

The XRF device could not be used to detect some trace elements, rare earth elements, Na, or elements lighter than Na. Therefore, the elemental concentrations reported (Tables 3.3 and 3.4) are those which the instrument can detect. CO_2 has been calculated by assigning all Ca and Mg to carbonates minerals (Table 4.1). As noted previously, the detection limits used in Tables 3.3 and 3.4 are those reported by the manufacturer for analyses under ideal circumstances and are likely lower than the actual detection limits for the data in the current study. Further, the calibration of the instrument was accepted without use of either primary or secondary standards similar to the rocks analyzed here. In the absence of use of appropriate standards, the data should only be treated as qualitative indicators of rock composition. Assessment of the data obtained (Table 4.1) does indicate that the bulk rock compositional data are not accurate. GS-2 and GS-4, both limestone samples, are shown to exceed 60 wt.% CaO, values that cannot be correct because a rock that is 100% calcite would be only 56 wt.% CaO. Furthermore, the sum of the major elements plus CO_2 calculated by assigning all CaO and MgO to carbonate minerals (Table 4.1) shows high totals for all but two samples without considering the additional weight of H_2O or Na_2O in the samples. So, the data are clearly not accurate. Even so, the data can be used with the thin sections to produce qualitative information to support the petrologic observations and, in the case of S and Mg, to interpret the outcrop diagenesis.

Table 4.1. The sum of the major elements plus CO_2, CO_2 has been calculated by assigning all CaO and MgO to carbonate minerals. SS = sandstone; DO = dolomite; LST = limestone.

Elements	**GS-1**	**GS-2**	**GS-3A**	**GS-3B**	**GS-3C**	**GS-4**	**GS-5**	**GS-6**	**GS-7**	**GS-8**	**GS-9**	**GS-10**	**GS-11**	**GS-12**	**GS-13**	**GS-14**
Rock Type	**SS**	**LST**	**SS**	**LST**	**LST**	**LST**	**DO**	**DO**	**DO**	**SS**	**DO**	**SS**	**SS**	**DO**	**SS**	**SS**
SiO_2 %	66	1.8	62	19	39	1.6	1.7	32	3.1	80.	8.7	63	60.	11	66	72
TiO_2 %	0.10	0.074	0.17	0.085	0.071	0.071	0.047	0.29	0.049	0.16	0.044	0.086	0.32	0.080	0.16	0.27
Al_2O_3 %	1.4	b.d.	2.8	1.1	1.6	b.d.	b.d.	4.9	0.39	4.3	0.48	1.5	6.8	1.0	4.5	4.8
Fe_2O_3 %	0.46	0.11	0.63	0.25	0.17	0.094	0.12	2.3	0.28	0.94	0.32	0.45	2.5	0.25	0.78	0.91
MnO %	0.010	0.020	0.015	0.012	0.0085	0.015	0.13	0.072	0.040	0.017	0.19	0.028	0.030	0.14	0.025	0.015
CaO %	22	61	22	53	41	61	37	25	36	7.9	35	16	12	33	8.9	10.
MgO %	b.d.	b.d.	b.d.	b.d.	b.d.	b.d.	19	14	23	3.7	20.	6.7	7.8	19	5.5	1.9
K_2O %	0.087	b.d.	0.68	b.d.	b.d.	b.d.	b.d.	1.2	b.d.	0.18	b.d.	0.036	2.0	0.055	0.84	1.0
CO_2 %	17	48	17	42	32	48	50	35	53	10	49	20	18	47	13	10
Total %	107	111	106	115	114	110	109	114	116	107	113	108	109	112	100	101

4.5 Diagenesis Within the Ingleside Formation

The diagenetic processes observed in the Ingleside thin sections, including cementation, compaction, and feldspar dissolution and alteration, can to some extent be placed relative to one another in a paragenetic sequence. This relative sequence is based on petrographic observations of spatial relationships among the various primary and diagenetic rock constituents. Hematite cement was likely precipitated during very early diagenesis, prior to compaction, because it coated the grains and is present between grain boundaries that were later affected by compaction (Fig. 3.25, 3.26).

Carbonate cement is observed to occur in three types. Poikilotopic dolomite cement, blocky calcite cement, and blocky dolomite cement. Previous studies of diagenesis have mainly described poikilotopic calcite cement, so it seems likely that the poikilotopic dolomite cement was precipitated as calcite cement and then was replaced by dolomite cement. This cement precipitated between grains that were not affected much by compaction, and probably saved the grains from the effects of compaction (Fig. 3.46). This suggests the poikilotopic cement, likely calcite, was precipitated very early before compaction. The grains that are cemented with the poikilotopic cement are coated with hematite cement (Fig. 3.47). This means that the poikilotopic cement probably precipitated after the hematite cement.

The blocky calcite and dolomite cements are present in pores between grains that are affected by compaction (Fig. 3.24). This may indicate that blocky cement might have been precipitated during or after compaction and was present to protect grains from the effects of compaction. The grains that are cemented with the blocky cement are sometimes rimmed with hematite cement (Fig. 3.25). This suggests that blocky cement was precipitated after the precipitation of hematite cement. However, there is no evidence to present for whether blocky calcite or blocky dolomite cement precipitated first.

Quartz overgrowth cement precipitated after the precipitation of the hematite cement. The grains cemented with quartz overgrowth cement are coated with the hematite cement (Fig. 3.26), which means the quartz overgrowth cement postdated the hematite cement. Based on when quartz overgrowth cement typically forms, it may have formed much later than hematite cement.

Kaolinite cement precipitated in pore space, and may be concurrent with feldspar dissolution which might be the source for Al and Si in the kaolinite cement (Bucke and Mankin, 1971). However, it is possible that kaolinite cement was formed by modern weathering rather than diagenesis. Some of the feldspar is partially altered to calcite, dolomite and kaolinite (Fig. 3.33), and this could be evidence that some of the feldspar replacement occurred during diagenesis. However, some of the feldspar replacement by kaolinite may have occurred during modern weathering.

Hydrocarbon migration is interpreted to have occurred before blocky carbonate cementation. Evidence for this is that some oil filled pore spaces, and then as the oil migrated, some residue of bitumen was left along the edges of pores, and then the blocky carbonate cement precipitated (Fig. 3.38). The oil does not appear to have flowed through or penetrated the blocky carbonate cement, which may indicate the oil moved before the precipitation of the blocky carbonate cement. Additional evidence is that some residue of bitumen is found in the edges of calcite-filled fractures (Fig. 3.48), which may indicate the oil moved along the fractures and then later the calcite precipitated in fractures. However, Figure 3-45 shows a fracture, now calcite-filled, that crosscuts blocky dolomite cement. This suggests that the calcite filling the fracture in sample ING-17 in bed 9 is later than dolomite and that fracturing may have occurred in multiple episodes or over a relatively long-time span.

Bedding-parallel stylolites observed in carbonate samples (Fig. 3.36) were probably formed during compaction, and may have been a source for carbonate that reprecipitated in veins or as a cement. The proposed paragenetic sequence of diagenetic processes affecting the Lower Ingleside Formation is shown in Figure 4.1.

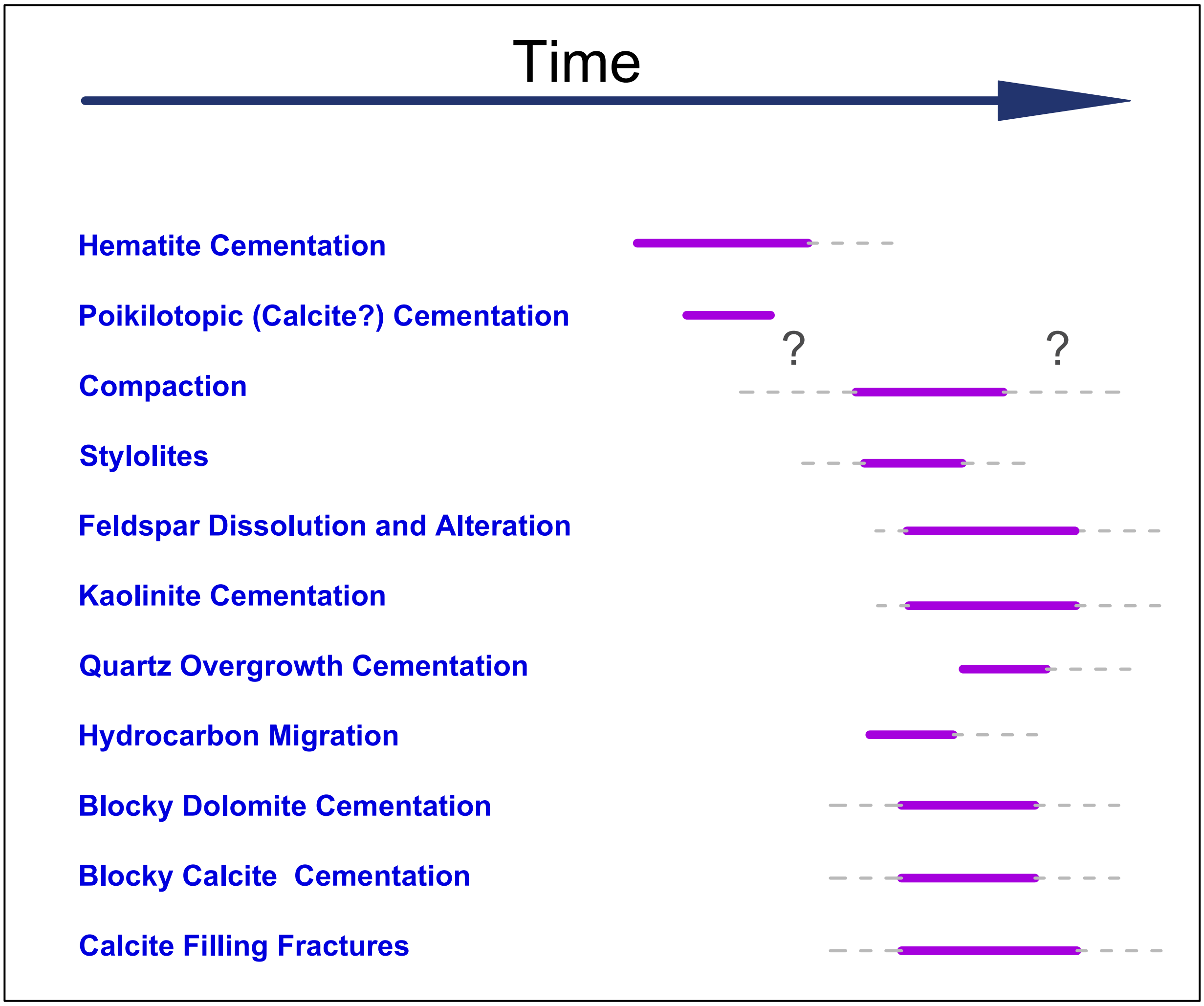

Figure 4-1. Paragenetic sequence of the diagenetic processes affecting the Lower Permian Ingleside Formation, Hwy. 287, Owl Canyon area, Larimer County, Colorado.

This study about the Ingleside outcrop could be useful from the perspective of a petroleum company if the Ingleside were being evaluated as a prospective hydrocarbon reservoir. This study describes the timing of diagenetic events and the timing of hydrocarbon migration in the Ingleside Formation. Understanding the timing of diagenetic events of the Ingleside Formation could help oil companies to evaluate the timing of changes in porosity and permeability, relative to hydrocarbon migration. With more detailed study, for example fluid inclusions, some of the diagenetic features described in this study might be useful for constraining temperature and pressure during burial and therefore in basin modeling. Further, this study describes the timing of hydrocarbon migration relative to other diagenetic events within the Ingleside, so this can help oil companies to investigate when the hydrocarbon moved and to determine its accumulation. Therefore, these techniques could assist oil companies with understanding petroleum exploration, trapping, and basin modeling.

CHAPTER 5
CONCLUSIONS

Petrographic analysis was combined with geochemical analysis in order to interpret the diagenetic history of the lower Permian Ingleside Formation exposed in the roadcut at Owl Canyon. This exposure is divided into fourteen different beds that dip to the east, and are composed mainly of sub-mature to mature quartz arenite sandstone, limestone, dolomite, or siltstone. Cements within the sandstone beds include calcite, dolomite, hematite, quartz, and kaolinite. Dolomite and calcite are the most common cements within the sandstone. Calcite cement is generally more abundant in stratigraphically lower samples, and dolomite cement content is variable, but generally higher in samples from the middle and upper part of the section studied. Carbonate cement occurs in three types, poikilotopic dolomite cement, blocky calcite cement, and blocky dolomite cement. Hematite cement probably precipitated in very early diagenesis before compaction. The poikilotopic cement was also precipitated very early, but after the precipitation of the hematite cement. The blocky calcite cement and the blocky dolomite cement precipitated after the poikilotopic cement. Kaolinite cement was probably precipitated during diagenetic feldspar dissolution, although both could also have occurred during modern weathering. Geochemical data provides some information about the outcrop diagenesis. The CaO in sandstone samples is due to the occurrence of calcite and dolomite cement. The MgO in sandstone samples is related to dolomite content. Furthermore, the low concentration of K_2O in sandstone samples could be attributed to the low proportion of K-feldspar, and other K-rich minerals and possibly reflects loss of K during diagenesis. The relationship fact that S and MgO are both more abundant in samples from the middle and upper parts of the outcrop than in deeper samples suggests that they were added by diagenetic fluids.

REFERENCES

Al-Hajeri, M.M., Al Saeed, M., Derks, J., Fuchs, T., Hantschel, T., Kauerauf, A., Neumaier, M., Schenk, O., Swientek, O., Tessen, N. and Welte, D., 2009. Basin and petroleum system modeling. Oilfield Review, vol. 21, no. 2, pp.14-29.

Berman, A.E., 1978. Permian stratigraphy and paleotectonics, Bellvue-Livermore area, Larimer County, Colorado: relation to petroleum in the Lyons Formation: M.S. Thesis, Colorado School of Mines, 86 p.

Berner, R.A., 1980. Early diagenesis; a theoretical approach Princeton series in geochemistry, Princeton Univ. Press: Princeton, NJ, United States, United States, 239 p.

Bjørlykke, K., 2010. Petroleum Geoscience from Sedimentary Environments to Rock Physics, Springer-Verlag Berlin Heidelberg, 508 p.

Bjorlykke, K. and Egeberg, P.K., 1993. Quartz cementation in sedimentary basins. AAPG Bulletin, vol. 77, no. 9, pp.1538-1548.

Boggs, S., Jr. 2009. Petrology of sedimentary rocks. United States: Cambridge University Press: New York, NY, United States, 599 p.

Bucke, D. and Mankin, C., 1971. Clay-mineral diagenesis within interlaminated shales and sandstones, Journal of Sedimentary Petrology, vol. 41, no. 4, pp. 971-981.

Butters, R.M., 1913. Permian or Permo-Carboniferous of the eastern foothills of the Rocky Mountains in Colorado, Bulletin - Colorado Geological Survey, Department of Natural Resources, vol. 5, Part 2, pp. 58-101.

Clayton, J.L., 1989. Geochemical evidence for Paleozoic oil in Lower Cretaceous Sandstone, northern Denver Basin: American Association of Petroleum Geologists Bulletin, v. 73, no. 8, pp. 977–988.

Clayton, J.L., 1999. Distribution and thermal history of Paleozoic source rocks in the Denver Basin, in Smith-Rouch, L.S., Wheeler, D.M., and Webb, J.C., eds., Pennsylvanian and Permian of the northern Denver Basin Colorado, Nebraska and Wyoming: RMS-SEPM (Rocky Mountain Section of the Society for Sedimentary Geology) Guide- book, p. 1–3.

COGCC, 2018. http://cogcc.state.co.us/data4.html#/production. Accessed March 2, 2018.

Crick, W.B., 1987. Sedimentology of the Ingleside Formation Horsetooth Reservoir, Larimer County, Colorado: M.S. Thesis, Colorado State University, 342 p.

Davis, R.A., 1947. The Origin, Age, and Correlation of the Ingleside Formation of North Central Colorado: M.S. Thesis, University of Colorado, Boulder, Colorado, 40 p.

Folk, R.L., 1974. Petrology of Sedimentary Rocks: Austin, TX, Hemphill Press, second edition, 182 p.

Fredrickson, J.A., 1978. Petrology and depositional environments of the Fountain and Ingleside formations, Owl Canyon, Colorado: M.S. Thesis, University of Wyoming, 100 p.

Higley, D.K. and Cox, D.O., 2007. Oil and gas exploration and development along the front range in the Denver Basin of Colorado, Nebraska, and Wyoming, in Higley, D.K., compiler, Petroleum systems and assessment of undiscovered oil and gas in the Denver Basin Province, Colorado, Kansas, Nebraska, South Dakota, and Wyoming—USGS Province 39: U.S. Geological Survey Digital Data Series DDS–69–P, ch. 2, 41 p.

Hoyt, J.H. and Chronic, B.J., 1961. Wolfcampian fusulinid from Ingleside Formation, Owl Canyon, Colorado. Journal of Paleontology, vol. 35, no.5, pp.1089.

Hoyt, J.H., 1962. Pennsylvanian and Lower Permian of northern Denver Basin, Colorado, Wyoming, and Nebraska, Bulletin of the American Association of Petroleum Geologists, vol. 46, no. 1, pp. 46-59.

Imam, M.B. and Shaw, H.F., 1987. Diagenetic controls on the reservoir properties of gas bearing Neogene Surma Group sandstones in the Bengal Basin, Bangladesh, Marine and Petroleum Geology, vol. 4, no. 2, pp. 103-111.

Islam, M.A., 2009. Diagenesis and reservoir quality of Bhuban sandstones (Neogene), Titas gas field, Bengal Basin, Bangladesh, Journal of Asian Earth Sciences, vol. 35, no. 1, pp. 89-100.

Kelly, A., 1984. Petroleum geology of the upper Casper Formation in the northern Laramie Basin, Earth Science Bulletin, vol. 17, pp. 104.

Land, L.S. and Dutton, S.P., 1978. Cementation of a Pennsylvanian deltaic sandstone: isotopic data, Journal of Sedimentary Petrology, vol. 48, pp. 1167-1176.

Land, L.S. and Milliken, K.L., 1981. Feldspar diagenesis in the Frio Formation, Brazoria County, Texas Gulf Coast, Geology, vol. 9, pp. 314-318.

Lee, M.K. and Bethke, C.M., 1994. Groundwater flow, late cementation, and petroleum accumulation in the Permian Lyons Sandstone, Denver Basin. AAPG bulletin, vol. 78, no. 2, pp.217-237.

Maughan, E.K. and Ahlbrandt, T.S., 1978. Field trip to Pennsylvanian and Permian rocks near Lyons, Colorado. School Notes," Clastic diagenesis--its role in reservoir quality and hydrocarbon entrapment: Amer. Assoc. Petr. School Course Note, Tulsa, 18 p.

Maughan, E.K. and Wilson, R.F., 1963. Permian and Pennsylvanian strata in southern Wyoming and northern Colorado. Guidebook to the geology of the northern Denver basin and adjacent uplifts: Rocky Mountain Association of Geologists, pp. 95-104.

McBride, E.F., 1989. Quartz cement in sandstones: a review, Earth-Science Reviews, vol. 26, pp. 69-112.

Milliken, K.L., 1994. Elemental mobility in sandstones during burial: whole-rock chemical and isotopic data, Frio Formation, South Texas, Journal of Sedimentary Research, Section A: Sedimentary Petrology and Processes, vol. 64, pp. 788-796.

Napp, K., 1985. Late Paleozoic stratigraphy and sedimentation, northwest Denver Basin, Colorado: Colorado State University: M.S. Thesis, 314 p.

Olympus, 2014. http://www.olympus-ims.com.

Pittman, E.D. and King, G.E., 1986. Petrology and formation damage control, Upper Cretaceous sandstone, offshore Gabon, Clay Minerals, vol. 21, no. 4, pp. 781-790.

Prucha, J.J., Graham, J.A. and Nickelsen, R.P., 1965. Basement-controlled deformation in Wyoming province of Rocky Mountains foreland. AAPG Bulletin, vol. 49, no.7, pp. 966-992.

Rahman, M.J, McCann, T, Abdullah, R, and Yeasmin, R., 2011. Sandstone diagenesis of the Neogene Surma Group from the Shahbazpur gas field, southern Bengal Basin, Bangladesh, Austrian Journal of Earth Sciences = Mitteilungen der Oesterreichischen Geologischen Gesellscaft, vol. 104, no. 1, pp. 114-126.

Rainoldi, A, Franchini, M, Beaufort, D, Mozley, P, Giusiano, A, Nora, C, Patrier, P, Impiccini, A, and Pons, J., 2015. Mineral reactions associated with hydrocarbon paleomigration in the Huincul High, Neuquen Basin, Argentina, Geological Society of America Bulletin, vol. 127, no. 11-12, pp. 1711-1729.

Schatz, B.A., 1986. Depositional environments of the Upper Fountain and Ingleside Formations between Lyons and Loveland. Colorado: MS Thesis, Boulder, University of Colorado, 118 p.

Schmidt, V. and McDonald, D.A., 1979. The role of secondary porosity in the course of sandstone diagenesis, Special Publication - Society of Economic Paleontologists and Mineralogists, no. 26, pp. 175-207.

Shi, C., Cao, J., Tan, X., Luo, B., Zeng, W. and Hu, W., 2017. Discovery of oil bitumen co-existing with solid bitumen in the Lower Cambrian Longwangmiao giant gas reservoir, Sichuan Basin, southwestern China: Implications for hydrocarbon accumulation process. Organic Geochemistry, vol. 108, pp.61-81.

Sipe, D.R., 1984. Depositional environments and origin of bounding surfaces in the Ingleside Formation, Livermore area, Colorado: M.S. Thesis, University of Wyoming, 99 p.

Sonnenberg, S., 2015. New reserves in an old field, the Niobrara/Codell resource plays in the Wattenberg Field, Denver Basin, Colorado. First Break, vol.33, no. 12, pp.55-62.

Steidtmann, J.R., 1974. Evidence for eolian origin of cross-stratification in sandstone of the Casper Formation, southernmost Laramie Basin, Wyoming. Geological Society of America Bulletin, vol. 85, no. 12, pp.1835-1842.

Taylor, T.R., Giles, M.R., Hathon, L.A., Diggs, T. N., Braunsdorf, N.R., Birbliblia, G.V., Kittridge, M.G., Macaulay, C.I., and Espejo, I.S., 2010. Sandstone diagenesis and reservoir quality prediction: Models, Myths, and reality, AAPG Bulletin, vol. 94, pp. 1093-1132.

Walderhaug, O., 1990. A fluid inclusion study of quartz-cemented sandstones from offshore mid-Norway; possible evidence for continued quartz cementation during oil emplacement, Journal of Sedimentary Petrology, vol. 60, no. 2, pp. 203-210.

Wilkinson, M, Milliken, K.L., and Haszeldine, R.S., 2001. Systematic destruction of K-feldspar in deeply buried rift and passive margin sandstones, Journal of the Geological Society of London, vol.158, pp. 675-683.

Worden, R.H. and Burley, S.D., 2003. Sandstone diagenesis; the evolution of sand to stone, Blackwell Publishing: Oxford, United Kingdom, pp. 1-44.